

INVESTIGATION OF 2D METAL CHALCOGENIDE NANOSTRUCTURES FOR SOLAR CELL APPLICATIONS

Thesis

Submitted in partial fulfillment of the requirements for the degree of

DOCTOR OF PHILOSOPHY

By

SUBHASHMITA RAY



DEPARTMENT OF PHYSICS

NATIONAL INSTITUTE OF TECHNOLOGY KARNATAKA,

SURATHKAL, MANGALORE-575025

SEPTEMBER, 2023

INVESTIGATION OF 2D METAL CHALCOGENIDE NANOSTRUCTURES FOR SOLAR CELL APPLICATIONS

Thesis

Submitted in partial fulfillment of the requirements for the degree of

DOCTOR OF PHILOSOPHY IN PHYSICS

By

SUBHASHMITA RAY



DEPARTMENT OF PHYSICS

NATIONAL INSTITUTE OF TECHNOLOGY KARNATAKA,

SURATHKAL, MANGALORE-575025

SEPTEMBER, 2023

DECLARATION

By the Ph.D. Research Scholar

I hereby *declare* that the Research thesis entitled “**Investigation of 2D metal chalcogenide nanostructures for solar cell applications**”, which is being submitted to the National Institute of Technology Karnataka, Surathkal in partial fulfillment of the requirements for the award of the Degree of Doctor of Philosophy in Physics is a *bonafide report of the research work carried out by me*. The material contained in this Research Thesis has not been submitted to any University or Institution for the award of any degree.

Subhasmita Ray
Name: Subhasmita Ray
Registration Number: 187077PH003
Department of Physics

Place: NITK-Surathkal
Date: *12.09.2023*

C E R T I F I C A T E

This is to *certify* that the Research Thesis entitled “**Investigation of 2D metal chalcogenide nanostructures for solar cell applications,**” submitted by Subhasmita Ray (Register Number: **187077PH003**) as the record of the research work carried out by her, is *accepted as the Research Thesis submission* in partial fulfillment of the requirements for the award of the degree of Doctor of Philosophy.


Research Guide(s)


12/9/2023
Dr. Kartick Tarafder


(Supervisor)

(Signature with Date & Seal)

भौतिकी विभाग / **Physics Dept.**
राष्ट्रीय प्रौद्योगिकी संस्थान कर्नाटक सुन्तकल
NITK SURATHKAL
मंगलूर 575 025 - कर्नाटक
MANGALORE-575 025, KARNATAKA


12/09/2023
Dr. Kasturi V. Bangera

(Co - supervisor)


12-9-2023
Chairman - DRPC
(Signature with Date and Seal)
Dr. N.K. UDAYASHANKAR
PROFESSOR & HEAD
DEPARTMENT OF PHYSICS
NITK SURATHKAL, SRINIVASNAGAR
MANGALORE - 575 025, INDIA

ACKNOWLEDGEMENT

“When the going gets tough, the tough get going” is one of the proverbs I have always believed in. Although a Ph.D. is intended to signify an individual's distinctive contribution to science, it would be insincere to imply that it can be achieved solely by one person. Throughout the past four and a half years, I have encountered numerous challenges, ranging from obtaining results to getting my manuscript accepted. Fortunately, some individuals have made this journey a bit smoother for me.

I would like to start by expressing my sincere gratitude to my supervisor, **Dr. Kartick Tarafder**, and co-supervisor, **Dr. Kasturi V. Bangera**, for accepting me as their student. I am grateful for their guidance, cooperation, and moral support that have kept me motivated.

I express my deepest gratitude to **Dr. Kartick Tarafder** for introducing me to density functional theory and supporting me throughout my studies with immense passion and trust in my abilities. His patience, support, and guidance allowed me to progress successfully in my work and develop as an independent researcher. I am indebted to him for his invaluable suggestions and encouragement throughout the research period. Without his constant motivation and persistent help, this thesis would not have been completed. I would also like to thank **Prof. Kasturi V. Bangera** for her advice and suggestions regarding my research work. Apart from this, I would like to thank my RPAC members, **Dr. Saikat Dutta** and **Dr. Ajith K M**, for their insightful comments during the progress presentation.

I have been extremely fortunate to work with some exceptionally talented people during my time as a doctoral student; without them, this thesis would not be possible. First, Thank you, **Dr. Sowjanya**, for sharing your knowledge of PVD systems. Working with **Dr. Bharath S. P.** and **Dr. Biswajit Barman** has been a privilege. Thank you so much for helping me to characterize the samples.

A special thanks to **Dr. Sulakshana Shenoy**, who helped me a lot when I changed my field of interest from experimental to theoretical condensed matter physics. I would also like to thank all my CMS colleagues, **Dr. Nayana**, **Dr. Shruti**, **Dr. Ramesh**, **Miss Suneetha**, **Mr. Anantharam**, **Mrs. Kalyani**, and **Mr. Ashwath**, for all the valuable

suggestions and discussions. I want to extend my sincere thanks to **Er. Basavaraj, Dr. Sahaj, Ramya, Vikash, and Kishore** for their support.

Finally, a big and special thanks to **Dr. Sunil Ray, Dr. Lekha Das, Er. Saibalini Ray and Dr. Saswat Ray**, for their unconditional love, support, and encouragement throughout this Ph.D. tenure, are beyond description.

There are numerous people with whom I would like to express my sincere gratitude. Even though I may have overlooked mentioning their names, their assistance will forever be etched in my memory.

I want to extend a heartfelt thank you to everyone who aided and stood by me during my Ph.D. research endeavor. Your generous support and guidance in every stage of my study enabled me to finish the program successfully. I am grateful for your contribution to my achievement.

This research work was funded by MHRD, India. I am grateful to NITK for providing the Institute fellowship, and I also appreciate Cense, IISC, for providing the SEM facility.

Subhasmita Ray

ABSTRACT

The use of two-dimensional metal chalcogenides in solar cells has become a popular research topic in the quest to meet global energy needs. This study concentrates on the preparation and performs a detailed investigation of the properties of various binary chalcogenide substances (II-VI and V-VI semiconductors) intended for solar cell usage. The properties of different heterostructures made from pristine semiconductors are also examined. The junction between two semiconductors is vital in separating and transferring the charge carriers. To gain insight into this phenomenon, a few heterostructures are suggested to advance the development of solar cells. The physical vapor deposition method is employed to deposit the samples (thin films), and several characterization tools are used to study the materials' structural, morphological, optical, and electrical properties.

Furthermore, the optimized geometry, electronic structure, and the optical properties of the binary semiconductors and their heterostructure are explored using the first-principles Density Functional Theory calculations. The proper band edge position (CB and VB) of the pristine semiconductors, band alignment in the heterojunctions and the separation of the charge carriers at the interface are studied theoretically. This thesis aims to not only describe the properties of the junction but also provide a diverse range of materials that can be used in the next generation of solar cells.

Keywords: Thin films, PVD, DFT, compound semiconductor thin film solar cells.

TABLE OF CONTENTS

Chapter 1	Introduction to Photovoltaics	Page No.
1.1	A general introduction	2
1.2	The semiconductor thin-film technology	3
1.3	Solar cells employing thin film technology	3
1.4	Mechanism of thin-film solar cell	5
1.5	Photovoltaic materials	6
1.5.1	Cadmium telluride (CdTe)	6
1.5.2	Zinc telluride (ZnTe)	6
1.5.3	Zinc selenide (ZnSe)	7
1.5.4	Cadmium selenide (CdSe)	7
1.5.5	Antimony selenide (Sb ₂ Se ₃)	7
1.5.6	Antimony sulphide (Sb ₂ S ₃)	8
1.6	Semiconductor heterojunctions in solar cell applications	8
1.7	Literature Survey	9
1.8	Scope of the work	15
1.9	Objectives	15
Chapter 2	Experimental, theoretical methodology and characterization techniques	
2.1	Experimental methodology	18
2.2	Characterization Techniques	19
2.2.1	X-Ray diffraction	19
2.2.2	Scanning electron microscope	21
2.2.3	Energy dispersive analysis by X-rays	22
2.2.4	UV-Vis spectroscopy	22
2.2.5	Electrical characterization	23

	2.2.6	Capacitance Vs. Voltage characterization	24
2.3		Theoretical approach	25
	2.3.1	Born-oppenheimer approximation	26
	2.3.2	Hartree-Fock approximation	27
	2.3.3	Density Functional Theory	28
	2.3.4	Thomas-Fermi-Dirac approximations	28
		2.3.4.1 H-K theorem 1	29
		2.3.4.2 H-K theorem 2	30
	2.3.5	The Kohn-Sham DFT	30
	2.3.6	Exchange-correlation energy functional	34
	2.3.7	Improvement in the conventional DFT method	35
		2.3.7.1 Self-interaction error	35
		2.3.7.2 Hybrid functional	35
		2.3.7.3 DFT + U functional	37
	2.3.8	Charge density calculation	37
	2.3.9	Bader charge analysis	39
	2.3.10	Band alignment of the heterostructure	40
2.4		Summary	42
Chapter 3		Preparation and properties of CdTe thin films at different substrate temperatures	
	3.1	Introduction	44
	3.2	Methodology	45
		3.2.1 Experimental methodology	45
		3.2.2 Theoretical methodology	46
	3.3	Results and discussion	46
		3.3.1 Experimental outcomes	46

	3.3.1.1	Structural analysis	46
	3.3.1.2	Morphological properties	48
	3.3.1.3	Optical properties	51
	3.3.1.4	Electrical properties	51
	3.3.2	Theoretical results	53
	3.3.2.1	Structural properties	53
	3.3.2.2	Electronic properties	53
	3.3.2.3	Work function and band edge position	54
3.4		Summary	55
Chapter 4		Preparation and properties of ZnTe thin films deposited at different substrate temperatures	
4.1		Introduction	58
4.2		Methodology	59
	4.2.1	Experimental methodology	59
	4.2.2	Theoretical methodology	59
4.3		Results and Discussions	60
	4.3.1	Experimental results	60
	4.3.1.1	Structural properties	60
	4.3.1.2	Morphological and elemental studies	61
	4.3.1.3	Optical properties	64
	4.3.1.4	Electrical properties	65
	4.3.2	Theoretical results	66
	4.3.2.1	Structural properties	66
	4.3.2.2	Electronic properties	67
	4.3.2.3	Work function and band-edge position	68
4.4		Summary	69

Chapter 5	<i>P-ZnTe/n-CdTe heterostructure preparation and properties. (ZnTe as a BSF layer in CdTe solar cells)</i>	
5.1	Introduction	72
5.2	Methodology	73
5.2.1	Experimental methodology	73
5.2.2	Theoretical methodology	73
5.3	Results and discussion	74
5.3.1	Experimental results	74
5.3.1.1	Structural properties	74
5.3.1.2	Optical properties	74
5.3.1.3	Electrical properties	76
5.3.2	Theoretical results	77
5.3.2.1	Optimized structure parameters, Electronic structure	77
5.3.2.2	Work function, band alignment, and the charge carrier dynamics	79
5.4	Summary	80
Chapter 6	<i>Investigation of CdSe and ZnSe as potential back surface field layer for CdTe based solar cells: A study from first principles calculations</i>	
6.1	Introduction	84
6.2	Computational methodology	85
6.3	Results and discussion	86
6.3.1	Geometric structures	86
6.3.2	Electronic structure	87
6.3.3	Optical properties	88
6.3.4	Band alignment and charge carrier dynamics	90
6.4	Summary	94

Chapter 7	Synthesis and characterization of Cu doped CdTe thin films for solar cell applications	
7.1	Introduction	98
7.2	Experimental details	99
7.3	Results and discussion	100
	7.3.1 X-ray diffraction analyses	100
	7.3.2 Morphological studies	102
	7.3.3 Optical properties	103
	7.3.3.1 Transmittance	103
	7.3.3.2 Optical band gap calculation	104
7.4	Summary	105
Chapter 8	Sulfur alloyed Sb₂Se₃ and a new 2D material for solar cell applications	
8.1	Introduction	108
8.2	Theoretical methodology	109
8.3	Results and discussion	110
	8.3.1 Crystal structure of S alloyed Sb ₂ Se ₃	110
	8.3.2 Electronic properties of S alloyed Sb ₂ Se ₃	112
	8.3.2.1 Band structure	112
	8.3.2.2 Density of states	113
	8.3.3 Introduction to mxenes and S4(130)/ mxenes interface	117
8.4	Summary	120

Chapter 9	ZnS_xSe_{1-x} thin films: A study into its tunable energy band gap property using an experimental and theoretical approach	
9.1	Introduction	124
9.2	Methodology	125
9.2.1	Experimental details	125
9.2.2	Computational technique	126
9.3	Results and discussion	126
9.4	Summary	137
Chapter 10	Summary, conclusion, and future scope of the work	
10.1	Summary of the work	140
10.2	Conclusion	140
10.3	Future scope of the work	141
References		143
Publications		
Curriculum vitae		

LIST OF FIGURES

Figure No.	Details	Page No
1.1	Schematic representation of solar cell	4
1.2	Schematic representation of different types of heterostructures a. Type-I b. Type-II c. Type-III	9
2.1	Experimental set up for thermal evaporation	18
2.2	A typical sketch of a Scanning Electron Microscope	21
2.3	Flow chart of Kohn-Sham iterative method	33
2.4	$x > 0$ is the electron reach layer, whereas the $x < 0$ is the hole reach layer, development of charge density due to the diffusion at the interface.	38
2.5	Two atoms (cyan solid circles) are used to show the Bader charge analysis in one dimension. The variation in electron density in one dimension is shown by the black solid line. A black dashed line designates the location of the zero-flux surface between the two atoms, while a blue dashed circle designates the Bader volume of each atom.	40
3.1	XRD pattern of CdTe thin films deposited at different substrate temperatures	47
3.2	SEM micrograph of CdTe thin films deposited at a substrate temperature of a. 300 K b. 373 K c. 423 K d. 473 K e. 523 K	49
3.3	Elemental mapping of a. Cd b. Te for the sample deposited at room temperature.	49
3.4	EDAX spectra of CdTe thin films deposited at substrate temperature of a. 300 K b. 373 K c. 423 K d. 473 K e. 523 K	50
3.5	Absorbance spectra of CdTe thin films at different substrate temperature	51

3.6	Band gap of CdTe thin films at different substrate temperature.	51
3.7	The variation of current with respect to the applied voltage for the CdTe thin films deposited at different substrate temperature.	52
3.8	Optimized geometry of the CdTe (110), right side image shows the unit cell.	53
3.9	Electronic band structure of CdTe (110)	54
3.10	DOS of CdTe (110)	54
3.11	Average electrostatic potential of CdTe(110)	55
4.1	XRD pattern of ZnTe thin films deposited at different substrate temperatures.	61
4.2	SEM micrograph of ZnTe thin films deposited at the substrate temperature of a. 300 K b. 373 K c. 423 K d. 473 K e. 523 K	62
4.3	Elemental mapping of a. Zn b. Te for the sample deposited at 300 K	63
4.4	EDAX spectra of ZnTe thin films deposited at a substrate temperature of a. 300 K b. 373 K c. 423 K d. 473 K e. 523 K	64
4.5	Absorbance spectra of ZnTe thin films deposited at different substrate temperatures.	65
4.6	The band gap of ZnTe thin films deposited at different substrate temperatures.	65
4.7	I Vs V characteristics of the ZnTe thin films deposited at different substrate temperatures.	66
4.8	Optimized geometry of ZnTe (110)	67
4.9	Band structure of ZnTe (110)	68
4.10	DOS of ZnTe (110)	68
4.11	Average electrostatic potential of ZnTe (110)	68

5.1	Diagrammatic representation of deposited layers for the heterojunction	74
5.2	The XRD pattern of ZnTe/CdTe deposited at the optimum condition within the 2Θ ranging from a. 20° - 65° b. 22° - 27°	75
5.3	Absorption spectra of ZnTe (black) and CdTe(orange) thin films deposited in the optimized condition and ZnTe/CdTe hetero junction (brown)	75
5.4	The band gap of ZnTe (black), CdTe(orange) thin films deposited in the optimized condition and ZnTe/CdTe hetero junction (brown)	75
5.5	I-V characteristics of p-ZnTe/n-CdTe heterojunction diode at room temperature.	76
5.6	The capacitance-voltage characteristic for p-ZnTe/n-CdTe heterojunction	76
5.7	Optimized geometry of ZnTe/CdTe interface	78
5.8	Electronic band structure of the heterostructure	78
5.9	DOS of the heterostructure	78
5.10	Average electrostatic potential of ZnTe/CdTe	79
5.11	Band edge position and their alignment for ZnTe, CdTe and ZnTe/CdTe heterojunction	81
6.1	Optimized geometry structures of a) ZnSe, b) CdTe, c) CdSe, d) ZnSe/CdTe, and e) CdSe/CdTe heterostructures.	87
6.2	Electronic band structure of a) ZnSe, b) CdTe, c) CdSe, d) ZnSe/CdTe, and e) CdSe/CdTe heterostructures. Fermi energy is set at $E = 0$ in each graph. Red and blue color bands represent valence and conduction bands, respectively.	88
6.3	The absorption spectrum of a) ZnSe (brown), CdTe (red), and ZnSe/CdTe heterostructure (black), b) CdSe	89

	(cyan), CdTe (red) and CdSe/CdTe heterostructure (pink).	
6.4	Partial density of states of a) ZnSe, b) CdTe, c) CdSe, d) ZnSe/CdTe, and e) CdSe/CdTe heterostructures. The Fermi energy is set at $E = 0$ in each graph.	90
6.5	The estimated work function of a) ZnSe (110), b) CdTe (110), c) CdSe (110), d) ZnSe/CdTe, and e) CdSe/CdTe	91
6.6	Charge density difference plots for a) ZnSe/CdTe and b) CdSe/CdTe heterostructures. The yellow and cyan color indicates the charge accumulation and charge depletion regions, respectively.	92
6.7	Relative band edge position and alignment in ZnSe, CdTe, CdSe, a) ZnSe/CdTe heterostructure, and b) CdSe/CdTe heterostructure with respect to the vacuum level.	93
6.8	A schematic diagram for the photo-generated charge carrier separation process in BSF-layer/CdTe heterostructure.	94
7.1	XRD images of the deposited films show the shifting of the 2θ value towards a higher angle.	100
7.2	Change in crystallite size (black) and strain (blue) due to a change in doping concentration.	102
7.3	SEM images of undoped CdTe thin film (A), 1% Cu doped CdTe thin Film (B), 2% Cu doped CdTe thin film(C), 3% Cu doped CdTe thin film (D), and 5% Cu doped CdTe thin film. (E).	103
7.4	Transmittance plot of undoped and Cu-doped CdTe thin films	104
7.5	Tauc's plot for undoped and Cu-doped CdTe thin films shows that the band gap decreases with increased doping percentage. This is maybe due to defect states.	105

8.1	Optimized bulk geometry of $\text{Sb}_2(\text{S}_x\text{Se}_{1-x})_3$ for $x =$ (S1) 0, (S2) 0.5, (S3) 0.6, (S4) 0.7, (S5) 0.8, (S6) 0.9, (S7) 1.0.	112
8.2	Band structure of $\text{Sb}_2(\text{S}_x\text{Se}_{1-x})_3$ for $x =$ (S1) 0, (S2) 0.5, (S3) 0.6, (S4) 0.7, (S5) 0.8, (S6) 0.9, (S7) 1.0 using HSE06 functional.	114
8.3	DOS of $\text{Sb}_2(\text{S}_x\text{Se}_{1-x})_3$ for $x =$ (S1) 0, (S2) 0.5, (S3) 0.6, (S4) 0.7, (S5) 0.8, (S6) 0.9, (S7) 1.0 using HSE06 functional	115
8.4	a. Optimized geometry, b. Band structure, and c. DOS of S4 using HSE06 functional.	117
8.5	a. Optimized geometry, b, and c: Electronic properties of ScHfNNoH	118
8.6	a. Optimized geometry of the heterostructure b, c. Electronic properties of the heterostructure.	119
8.7	The optical absorbance spectra of S4 (130), mxenes, and their heterostructure were estimated using the DFT.	120
9.1	XRD diffractograms of $\text{ZnS}_x\text{Se}_{1-x}$ films for $x =$ (a) 0, (b) 0.10, (c) 0.25, (d) 0.50, (e) 0.75, (f) 0.90, and (g) 1.	127
9.2	Variation of the (1 1 1) peak position of the $\text{ZnS}_x\text{Se}_{1-x}$ thin films for $x =$ (a) 0, (b) 0.10, (c) 0.25, (d) 0.50, (e) 0.75, (f) 0.90, and (g) 1.	128
9.3	Optimized geometry of $\text{ZnS}_x\text{Se}_{1-x}$ films for $x =$ (a) 0, (b) 0.10, (c) 0.25, (d) 0.50, (e) 0.75, (f) 0.90, and (g) 1.	129
9.4	FESEM images of $\text{ZnS}_x\text{Se}_{1-x}$ films for $x =$ (a) 0, (b) 0.10, (c) 0.25, (d) 0.50, (e) 0.75, (f) 0.90, and (g) 1.	130
9.5	Elemental mapping images of $\text{ZnS}_{0.50}\text{Se}_{0.50}$ thin films (a) Zn, (b) S, and (c) Se.	131
9.6	Transmittance plot of $\text{ZnS}_x\text{Se}_{1-x}$ films for $x =$ (a) 0, (b) 0.10, (c) 0.25, (d) 0.50, (e) 0.75, (f) 0.90, and (g) 1.	132

9.7	Tauc's plot of $\text{ZnS}_x\text{S}_{1-x}$ films for $x =$ (a) 0, (b) 0.10, (c) 0.25, (d) 0.50, (e) 0.75, (f) 0.90, and (g) 1.	133
9.8	Calculated band structure of $\text{ZnS}_x\text{Se}_{1-x}$ thin films for $x =$ (a) 0, (b) 0.10, (c) 0.25, (d) 0.50, (e) 0.75, (f) 0.90, and (g) 1 using HSE06 functional	134
9.9	PDOS of $\text{ZnS}_x\text{Se}_{1-x}$ thin films for $x =$ (a) 0, (b) 0.10, (c) 0.25, (d) 0.50, (e) 0.75, (f) 0.90, and (g) 1	135
9.10	Theoretical absorption co-efficient of $\text{ZnS}_x\text{Se}_{1-x}$ films for $x =$ (a) 0, (b) 0.10, (c) 0.25, (d) 0.50, (e) 0.75, (f) 0.90, and (g) 1.	136
9.11	Variation of the energy band gap of $\text{ZnS}_x\text{Se}_{1-x}$ thin films with composition 'x.'	137

LIST OF TABLES

Table No.	Details	Page No.
3.1	Structural parameters of CdTe thin films at the different substrate temperatures	48
3.2	Composition of CdTe samples at elevated substrate temperature	50
3.3	Change in the energy band gap of the deposited CdTe thin films	52
4.1	Structural parameters of ZnTe thin films at the different substrate temperatures	61
4.2	Elemental composition of ZnTe thin films at different substrate temperatures	63
4.3	Change in the energy band gap of the deposited ZnTe thin films	65
6.1	Band gap energy, work function, and the band edge positions for pristine CdTe, ZnSe, and CdSe layers	86
7.1	XRD data of Cu-doped CdTe thin films with different doping concentrations	101
7.2	Average grain size and elemental analysis of deposited films	103
7.3	Band gap and average transparency of the deposited films	105
8.1	Band gap and the position of VBM and CBM for S alloyed Sb_2Se_3	113
9.1	Structural parameters of ZnS_xSe_{1-x} films.	128
9.2	Composition and energy band gap of ZnS_xSe_{1-x} thin films.	131

NOMENCLATURE

Abbreviations:

Si	Silicon
PCE	Power conversion efficiency
CdTe	Cadmium Telluride
CIGS	Copper Indium Gallium Selenide
CZTS	Copper Zinc Tin sulfide
SQ	Shockley Queisser
IR	Infrared
TCO	Transparent conducting oxide
BSF	Back surface field
E_g	Bandgap
ZnTe	Zinc telluride
CdSe	Cadmium selenide
ZnSe	Zinc selenide
Sb_2Se_3	Antimony selenide
Sb_2S_3	Antimony sulfide
n-	N type semiconductors
p	p- type semiconductors
SnO_2	Strontium oxide
FF	Fill factor
J_{sc}	Short circuit current
V_{oc}	Open circuit voltage
CdS	Cadmium sulfide
T_s	Substrate temperature
η	Efficiency
$CdCl_2$	Cadmium chloride
AMPS	Analysis of Microelectronic and Photonic Structure) simulation program

SCAPS	Solar cell capacitance simulator
PVD	Physical vapor deposition
CVD	Chemical vapor deposition
MBE	Molecular beam epitaxy
DFT	Density Functional Theory
HF	Hartree Fock
DOS	Density of states
CB	Conduction band
VB	Valence band
CBO	Conduction band offset
VBO	Valence band offset
PBE	Perdew-Burke-Ernzerhof
GGA	Generalized gradient approximation
HSE	Heyd-Scuseria-Ernzerhof
HK	Hohenberg-Kohn
PAW	Projector Augmented Wave
XRD	X-Ray diffraction
SEM	Scanning electron microscope
EDAX	Energy –dispersive X-ray analysis
I-V	Current Versus Voltage

Symbols and units:

Mm	Micrometer
eV	Electron volt
Mv	Millivolt
Ma	Mili-ampere
A	Absorption coefficient (cm^{-1})
K	Temperature in Kelvin
h	Planck's constant
$h\nu$	Photon energy
Nm	Nanometer

λ	Wavelength
$^{\circ}\text{C}$	Celsius
D	Crystallite size
D	Interplanar spacing
2θ	Bragg angle
at %	Atomic percentage

CHAPTER 1

INTRODUCTION TO PHOTOVOLTAICS

Overview:

This chapter describes a brief introduction to photovoltaic cells. The unique properties of thin films are explained, followed by a discussion on different materials for their applications in photovoltaic cells. The literature survey emphasizes the materials and their heterostructure from theoretical and experimental perspectives. Furthermore, the scope and objectives of the present work are mentioned in the following sections.

1.1 A general introduction:

The demand for per capita energy is increasing day by day. The major challenge in the 21st century is to satisfy the energy requirements of human beings. Until now, the primary source of energy to meet daily needs has been fossil fuels. However, we are aware that this limited resource will become scarce in the coming years, and the use of fossil fuels significantly impacts the environment through air pollution (Perera 2017). Consequently, there has been a push to harness power from renewable resources like the sun and the wind. Solar energy is a promising eco-friendly fuel source. Efforts have been made to utilize solar energy by using solar cells. The Si solar cell, a first-generation photovoltaic cell, has been the traditional option. Recently, a Si-solar cell with a back contact structure and a module size of 180 cm² reported a high Power Conversion Efficiency (PCE) of 26.33% (Yoshikawa et al. 2017). Although silicon-based cells are currently the most viable option, they have some limitations. The production cost for pure silicon used in solar cells is very high. Additionally, the material has an indirect bandgap, and a relatively low absorption coefficient. To overcome these drawbacks, second-generation CdTe and CIGS-based solar cells are proposed, which exhibit moderate power conversion efficiency (Birkmire and McCandless 2010). The parent compounds in these cells are cost effective to produce, possess direct bandgap, and have a large absorption coefficient in the visible light range. As a result, the cells' efficiency is anticipated to increase with less production cost (Dharmadasa et al. 2014). Recently, compound semiconductor thin films such as Cadmium Telluride (CdTe), Copper Zinc Tin Sulfide (CZTS), and Copper Indium Gallium Selenide (CIGS) have received more attention for their application in the field of thin film solar cells. However, these compound semiconductor thin films can achieve a PCE of up to 17%, it I, and it comparable to silicon wafer-based solar cells. De Vos et al. predicted a 42% PCE for the dual hetero-junction solar cell (also known as the tandem solar cell) in 1980 (De Vos 1980). For almost all the single junction thin film solar cells, the achieved PCE is less than the Shockley-Queisser (SQ) limit. For CdTe solar cells, the SQ limit suggests a maximum theoretical efficiency of approximately 30% (Shockley and Queisser 1961). However, the highest reported experimental efficiency thus far is 22.1%, as noted by Green et al. in 2020 (Green et al. 2021a).

This implies that careful studies of band edge positions, interface properties, band alignment, and the suitable doping concentration in the elemental layers can significantly increase the power conversion efficiency.

1.2 The semiconductor thin-film technology:

The accumulation of scientific knowledge and technological advancements have significantly impacted human life. Through fundamental insights in material science, we have been able to fabricate solar cells that are not only lighter but also more robust and durable. The usefulness of scientific and technological products ultimately depends on the societal needs they serve. Following the invention of the transistor, semiconductor thin films emerged as a critical development. Compound semiconductor thin films play a vital role in modern society. These films, whose thickness can vary from the nanometer to the micrometer range, show different material's characteristics compared to its bulk form. Thin films boast a high surface-to-volume ratio and can exhibit unique electrical, magnetic, and optical traits. Both crystalline and amorphous thin films are incredibly significant in the realm of advanced technological applications. Thin films of various compounds have many applications, including microelectronic devices such as magnetic recording devices, sensors, Infrared (IR) detectors, interference filters, solar cells, satellite temperature regulator, and superconductors. The epitaxial growth of thin films allows precise control over the electron and phonon transport processes in metals, insulators, and semiconductors. Additionally, thin films have made significant contributions to solid-state physics, such as enabling quantum mechanical tunneling through metal-insulator junctions, micromagnetics, and plasma resonance absorption. Thin films exhibit excellent thermal stability and superior mechanical properties, including higher yield strength, elastic modulus, and interfacial adhesion. This makes them an ideal choice for ensuring device stability. Furthermore, thin films demonstrate distinct electronic, optical, and mechanical behavior compared to their bulk counterparts. The high yield strength of thin films allows them to withstand significant residual stresses, which are relieved through plastic deformation.

1.3 Solar cells employing thin film technology:

Figure 1.1 illustrates the various thin-film layers that constitute the thin-film solar

cell, including the transparent conducting oxide (TCO), window layer, absorber layer (either n or p-type), and the metal contact layer. The overall performance of the cell depends on each of these layers as it has different physical and chemical properties. The substrate is used to deposit the thin film layers. A TCO layer collects current from the external circuit at the top of the multilayer junction. The TCO is then positioned to form a junction with the absorber layer, and a window layer is then positioned directly below the TCO. The absorber layer produces a photo-generated charge carrier by absorbing photons from the light source. Charge carriers are further transported to the electrode with the help of the window layer. The lowermost layer in the cell is the bottom electrode consisting of a metal thin-film. Another back surface field (BSF) layer can be used between the absorber and the bottom electrode to limit charge recombination on the back side of the material. Higher doping on the solar cell's backside creates a "back surface field" (BSF). The transition zone between the highly and weakly doped regions exhibits p-n junction behavior. Due to an electric field at the interface, minority carrier transport to the back surface is impeded. As a result of the BSF's passive shielding effect on the rear surface, a high concentration of minority carriers is preserved throughout the device.

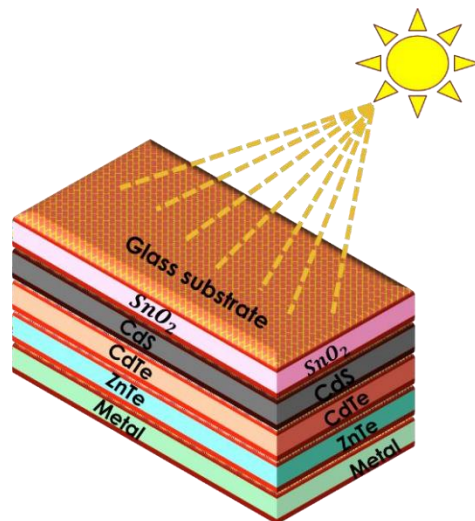


Figure 1.1: Schematic representation of solar cell

Intriguingly, the crystal structure, electron affinity, work function, thermal expansion coefficient, diffusion coefficient, chemical affinity, mobility, mechanical adhesion, etc., of each layer used in a thin-film solar cell are all

unique. The interface can cause a change in the electrical and optical characteristics of heterostructures due to stress, surface recombination centers, photon reflection/transmission/scattering, inter-diffusion, and chemical changes. Therefore, a detailed understanding of the individual layer and their interfaces is very important to design an efficient solar cell.

1.4 Mechanism of thin-film solar cell:

A solar cell typically uses a photovoltaic effect to convert sunlight into electricity. Semiconducting material is used in the active layer of the cell, which is responsible for light absorption. In case of semiconductors, there exists a gap between the valence band (consists of localized electrons) energy spectrum and conduction band (contains the free electrons) energy spectrum. The semiconducting materials have most electrons in the valence band at room temperature. These electrons absorb the energy of a solar photon and move into the conduction band, leaving holes in the valence band. An electron-hole pair is formed when a conduction band electron and a valence band hole come nearer. Because both the electron and the hole are free to move around, this pair can transmit electricity through the material. The photon with the same energy is released when the electron and hole are allowed to recombine and return to their original state (which is a lower energy state). According to the principle of detailed balance, in a state of thermodynamic equilibrium, the rate at which a photon is absorbed to excite an electron-hole pair and the rate at which a photon is emitted to destroy the same pair must be equal. For the optimal performance of the solar cell, the electron and hole of the electron-hole pair must be separated during the excitation process of the semiconducting material. There are a few ways to accomplish this, but a p-n junction is the most common. Here, a p-type and n-type semiconducting layer converge, creating a chemical potential difference that pulls electrons in one direction and holes in the other, effectively splitting the electron-hole pair. Using metal contacts with different work functions is another option, analogous to a Schottky-junction cell.

When light incidents on the surface of a solar cell, only the photons with sufficient

energy than the bandgap of the semiconductor are absorbed. To create electron-hole pairs, this absorption kicks off the process of valence-to-conduction-band electron transitions. It is straightforward to separate and store these carriers for the further reaction if they diffuse into the depletion region before recombination.

1.5 Photovoltaic materials:

As mentioned in the previous section, solar cell efficiency can be significantly improved by using a class of semiconducting thin films in the cell. There exist various 2D metal chalcogenide materials, among them Cadmium telluride (CdTe), Zinc-telluride (ZnTe), Cadmium selenide (CdSe), Zinc selenide (ZnSe), Antimony selenide (Sb₂Se₃), and Antimony sulfide (Sb₂S₃) are the most promising candidates, which can be effectively used as different layers in the solar cell.

1.5.1 Cadmium telluride (CdTe):

Cadmium Telluride (CdTe) is an II-VI semiconductor with a direct bandgap of 1.5 eV at room temperature and a high absorption coefficient. CdTe thin film with a layer thickness of only 2 μm can absorb up to 90% of the incident light (compared with around 10 μm for Si). CdTe is viewed as a potential photovoltaic material because of its low cost and excellent performance in solar cells. Unlike other II-VI compound semiconductors, doping acceptor or donor impurities in this one makes it easy to switch between n-type and p-type conductivity.

1.5.2 Zinc telluride (ZnTe):

Crystals of zinc telluride (ZnTe) are II-VI semiconductors, have a zinc-blende cubic structure and a high band gap of 2.25 eV at 300 K. Green light-emitting diodes made from this material has great potential. Most II-VI wide-bandgap semiconductors can be doped to the n-type but not the p-type. ZnTe, however, stands out because it can be readily doped p-type but just not n-type. Consequently, n-type doping in ZnTe is difficult to achieve.

1.5.3 Zinc selenide (ZnSe):

Zinc selenide (ZnSe) is a significant compound semiconductor in the II-VI group chalcogenides. Typically, semiconductors in this group have a wide band gap, with ZnSe having a value of approximately 2.7 eV at room temperature. Additionally, ZnSe possesses other beneficial properties such as a low exciton binding energy (~21 meV), excellent electronic transport abilities, high refractive indices (both linear and nonlinear), and a wide range of optical transparency in the visible spectrum. These properties make chalcogenide semiconductors highly versatile in chemical analysis, treatment of biological entities and diseases, and the development of physical, electrical, and mechanical devices, notably solar cells.

1.5.4 Cadmium selenide (CdSe):

This is an inorganic compound that belongs to the II-VI semiconductor group and appears as a black-to-red-black solid. Its bulk direct bandgap at room temperature is 1.74 eV, which falls within the visible spectrum. CdSe its natural crystalline forms are either hexagonal (wurtzite) or cubic (sphalerite, rock salt). CdSe is useful in solar cells, bio-imaging, fluorescent tagging, and electroluminescent devices like LEDs because its optical and electrical properties can be precisely adjusted at the nanoscale level through quantum confinement. CdSe quantum dots, a zero-dimensional material with promising applications in nano-engineering, are the subject of extensive research.

1.5.5 Antimony selenide (Sb₂Se₃):

Sb₂Se₃ belongs to the V-VI binary semiconductor group and is a viable material for photoconductive detectors. The sulfosalt mineral antimonselite crystals form in the orthorhombic space group and are denoted by the IMA symbol Atm. Antimony is in the +3-oxidation state in this mineral, and selenium is in the -2 oxidation state. The bonding in this mineral is covalent in nature, which is evident from its black color and semiconducting properties. The c-axis of the crystal has an unusually high low-frequency dielectric constant of 133 at room temperature. At ambient conditions, its band gap is 1.18 eV.

Sb_2Se_3 solar cells have several advantages over popular options like cadmium telluride and copper indium gallium selenide. It remains stable at low temperatures with a single phase and is abundant in the earth while also low-toxic and easy to prepare. These features make Sb_2Se_3 a viable alternative to traditional solar cell options that are limited by toxicity or scarcity.

1.5.6 Antimony sulfide (Sb_2S_3):

Stibnite, also known as antimony sulfide (Sb_2S_3), is a nanomaterial with an orthorhombic crystal structure and semiconductor properties. It displays exceptional characteristics and can be utilized in electronic and optoelectronic devices. The direct band gap of this semiconductor is between 1.8 and 2.5 eV. Doping techniques allow the fabrication of both p-type and n-type materials.

1.6 Semiconductor heterojunctions in solar cell applications:

From the binary semiconductors, several heterostructures were constructed, and their properties were studied. To understand the charge transfer mechanism, it is essential to know the different types of semiconductor heterojunctions that may form in solar cells.

1. Type –I, also called a straddling heterojunction, in which E_{c2} is greater than E_{c1} , whereas, E_{v2} is lesser than E_{v1} . In this scenario, the two charge carriers require energy to transition from the semiconductor with a lower band gap to the one with a wider band gap. As they cross the junction, the carrier from the opposite side releases this energy.
2. Another type of heterostructure is the Type-II, also known as a staggered junction. In this configuration, the band gaps of the two semiconductors overlap, resulting in one carrier losing energy while the other gains the same amount of energy. Additionally, the movement of the charge carrier is unsymmetrical.

3. In the Type-III or broken gap configuration, the bandgap of two semiconductors does not overlap. The carrier transfer situation is similar to Type-II, but more noticeable.

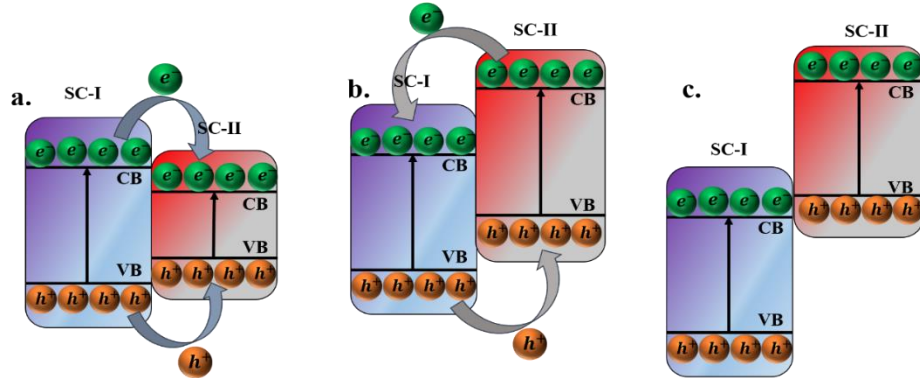


Figure 1.2: Schematic representation of different types of heterostructures

a. Type-I b. Type-II c. Type-III

1.7 Literature survey:

CdTe has a remarkable feature allows for creating a full photovoltaic device through thin film technology. For the first time, Bonnet and Rabenhorst made this discovery as far back as 1972, when they published a paper on CdTe/CdS thin film solar cells that showed an efficiency of 6 percent. Since then, many groups have tried to improve the efficiency of CdTe/CdS solar cell by adopting different deposition technique. However, it was not until the 1980s that Tyan and Albuerne (Tyan and Perez-Albuerne 1982) exceeded the 10% efficiency value. Ferekides et al. studied the efficiency of CdTe/CdS deposited on glass substrates. The CdS window and CdTe absorber layers were deposited using a chemical bath deposition technique. The process involved depositing a 500-1200 Å CdS layer on a SnO₂-coated glass substrate, then depositing a 4-8 μm CdTe thin film at varying substrate temperatures to achieve optimal junction properties. At the National Renewable Energy Laboratory, the most effective device achieved (AM 1.5G) conversion efficiency of 15.8% with a fill factor of 74.5%, an open-circuit voltage of 843 mV, and a short-circuit current of 15.1 mA/cm² (Ferekides et al. 1993). CdTe thin films were deposited by H.R Moutinho et al. in 1995 using physical vapor deposition, sputtering, and closed space sublimation. The films were subsequently treated with CdCl₂ at varying temperatures. Regardless of the deposition technique or substrate structure, the sample showed the highest device quality after being treated at

400°C. Additionally, a nano-grain structure was discovered in CdTe sputtered samples for the first time (Moutinho et al. 1995). In 2004, Xuanzhi Wu developed three new materials, including cadmium tin oxide (CSO) as a transparent conducting oxide layer, Zinc tin oxide (ZSO) as a buffer layer, and a window layer CdS: O. A modified CTO/ZTO/CdS/CdTe device structure was introduced. These innovations were aimed at addressing issues associated with standard SnO₂/CdS/CdTe cells and improving the performance and reproducibility of CdTe cells. The result was a CTO/ZTO/CdS/CdTe polycrystalline thin-film solar cell with an NREL-confirmed total-area efficiency of 16.5%, which was the highest efficiency ever reported for CdS/CdTe solar cells. This was achieved with a Voc of 845.0 mV, Jsc of 25.88 mA/cm², FF of 75.51%, and an area of 1.032 cm² (Wu 2004).

Even though CdTe/CdS solar cells exhibit high performance and efficiency, several unsolved challenges in their production prevent the efficiency improvement. The back contact issue is one of the most important because it affects the solar cell's durability over time. Several metals, including copper (Cu), lead (Pb), silver (Ag), and gold, were used to create a low resistance or ohmic contact with a p-type CdTe film (Au) (Bätzner et al. 2000; Corwine et al. 2004; Ernst et al. 2001; Kanevce and Gessert 2011; Visoly-Fisher et al. 2003). As a result, these materials tend to diffuse into different layers and deteriorate the stability of the cell. In 2010, Matin et al. used the SCAPS 1D to simulate solar cells. The back surface field layer (BSF), Sb₂Te₃ or ZnTe, and buffer layer, ZnO or Zn₂SnO₄, were introduced in the conventional CdTe solar cell, and the PCE was calculated. The problem of back surface recombination loss and the inefficiency of cells were thought to be amenable to solutions involving the introduction of materials with different bandgap properties, such as ZnTe (with a higher bandgap of 2.25 eV), Sb₂Te₃ (with a lower bandgap of 0.3 eV), and most importantly, the Back surface Reflector (BSR) materials of high dielectric coefficient (Matin et al. 2010). An efficiency of 16.9% was achieved. An 18.7% efficient solar cell was developed in 2012 at NREL. The following year, they produced a solar cell made of CdTe with an efficiency of 19%. The highest V_{OC} of 900 mV was reported by M. Gloeckler (Gloeckler et al. 2013).

A new composite absorbing layer was developed in 2013 using cycle growth and a single offset superlattice made from CdTe/ZnTe. The study involved subjecting the solar cells to multiple cycles to determine their properties in relation to the superlattice.

In addition, the crystallinity, transmission spectrum, and cross-sectional morphology of the ZnTe/CdTe composite layers were investigated using a variety of experimental cycles. The solar cells with an FTO/CdS/CdTe/ZnTe: Cu/(ZnTe|CdTe)_n/ZnTe: Cu/Au structure exhibited an impressive spectral response from 550-800 nm, with some response from 850-900 nm. Incorporating the composite layer led to a 12.8% improvement in photoelectric conversion efficiency, a short-circuit current density of 25.59 mA/cm, and a fill factor of 66.8%. The spectral response can be further enhanced by integrating with other technologies (He et al. 2017). Later, Deepak Sutar et al. investigated the change in ZnTe film thickness during annealing. The goal was to determine if these films could work as a suitable rear contact material. They developed 200 nm and 300 nm thin ZnTe films through e-beam evaporation, which were subsequently annealed at 100⁰C, 200⁰C, and 300⁰C in air ambient. The films were then characterized using appropriate tools to explore their physical properties. The results demonstrated a robust relationship between film thickness, annealing temperature, and the resulting films' physical properties. In CdTe solar cell devices, the 200 nm ZnTe thin films annealed at 100⁰C worked well as the rear contact material (Suthar et al. 2021a).

The study revealed that thin film solar cells comprised layers including FTO, TiO₂, n-ZnSe, p-CdTe, Ag: ZnSe, and Ni. The Ag: ZnSe layer was important for reducing barrier height and improving the performance of the solar cell. They examined the effect of buffer layers, bandgap energy, and temperature on the efficiency of solar cells. Incorporating the Ag: ZnSe layer improved efficiency from 17.01 to 22.31% (Souri and Marandi 2023). By exchanging the metal contact for a highly reflective one-dimensional distributed Bragg reflector, the research team of Kazmi et al. achieved a substantial improvement. This improved cell performance was achieved by increasing the optical path length at a wide range of angles and frequencies. The proposed cell demonstrated impressive electrical parameters under global AM 1.5G conditions, with J_{SC} of 25.036 mA/cm², V_{oc} of 1.065 V, FF of 87.56%, and η of 23.94% (Kazmi et al. 2020). Matin et al. introduced the Cu₂Te BSF layer in 2013 to improve the conversion efficiency. An established simulator called the 'Analysis of Micro-electronics and Photonic Structures' (AMPS-1D) was used to investigate the performance of cells, including V_{oc}, J_{sc}, FF, efficiency, and temperature stability. A modified structure of

CdTe-based PV cell, $\text{SnO}_2/\text{Zn}_2\text{SnO}_4/\text{CdS}/\text{CdTe}/\text{Cu}_2\text{Te}/\text{Ni}$, was proposed as an improvement over the reference structure of $\text{SnO}_2/\text{Zn}_2\text{SnO}_4/\text{CdS}/\text{CdTe}/\text{Cu}$. The simulation findings demonstrated that the cell's performance was improved without compromising the cell's stability after adding Cu_2Te as a BSF layer. New doors have been opened for ultra-thin CdTe PV cells as the analysis showed high conversion performance of 19.5% can be reached using a 0.6 μm thick CdTe absorber with BSF. The cell was stable at higher temperatures (Matin et al. 2013). Back surface field (BSF) SnS layers were first introduced by Sabrina et al. in the field of CdTe solar cells. Part of a series of thin layers, including a buffer layer (CdS) between the absorber layer (CdTe) and the windows layer (ZnO-Al), was added after the back contact (Ni). The latest findings revealed that the structure featuring the BSF layer ($\text{ZnO}/\text{CdS}/\text{CdTe}/\text{SnS}/\text{Ni}$), with dimensions of 0.6 μm of CdTe, 0.02 μm of CdS, 0.2 μm of ZnO, and 0.4 μm of SnS, offers an impressive efficiency of 21.83%. This enhancement in electrical efficiency surpasses prior reported results while reducing costs through a thinner absorber layer (Benabbas et al. 2016).

Different methods of treating CdTe thin films were suggested as alternatives to the traditional post-deposition treatment. These methods involved treating the films with CdCl_2 , MgCl_2 , CuCl_2 , and AgNO_3 . The effect of these treatments on the films' microstructural, morphological, and optoelectrical properties was studied. When compared to other treatments, it was seen that the CuCl_2 treatment led to a higher carrier concentration of 10^{15} cm^{-3} . The diffusion of Cu in the CdS/CdTe layer may have acted as a co-doping mechanism. Thus, it is crucial to carefully select the post-deposition treatment and conduct thorough investigations to enhance the performance of CdTe thin film solar cell devices (Harif et al. 2020). T.D. Dzhafarov conducted research on the impact of Cu on the properties of CdTe thin films through diffusion. At 400 degrees Celsius, adding Cu to CdTe thin films reduces the resistivity of p-type materials by up to seven times higher. A study compared CdTe(Cu)/CdS and CdTe/CdS cells found that CdTe(Cu)/CdS cells had increased efficiency but degraded faster due to electrodiffusion of Cu in the CdTe film (Dzhafarov et al. 2005). Polycrystalline CdTe thin films had their hole density increased by group V substitution on Te, a method developed by Brian McCandless et al. Vapor transport deposition was used to deposit

P, As, and Sb-doped CdTe films onto the superstrate solar cell structure at 550⁰C. They used capacitance-voltage analysis to calculate the doping level. The dopant incorporation levels were confirmed to be 10¹⁷-10¹⁸ atoms/cm³, and acceptor concentrations increased to >10¹⁵ cm⁻³ for P and >10¹⁶ cm⁻³ for As and Sb (McCandless et al. 2019). N.B. Chaure et al. demonstrated the positive impact of Iodine doping on CdTe thin films. By adding iodine to the CdTe layers, the electrical conductivity was significantly improved, as expected. Additionally, optimal concentrations of 0.05M CdI₂ in the bath resulted in enhanced optical absorption. The study also noted an impressive short-circuit current density of nearly 60 mA cm⁻², with satisfactory V_{oc} values of 700 mV. While the fill factors were negatively affected by the structure's low conductivity, this work effectively demonstrated the benefits of iodine doping (Chaure et al. 2003). H. Zhao studied the effects of O and Sb doping on CdTe solar cells deposited using the closed-space sublimation technique. The study found that the effect on V_{OC} was not solely dependent on the doping concentration but also influenced by factors like a reduction in reverse saturation current. This was observed in CdTe cells that the introduction of O₂ during the CSS process, affects both the doping concentration and CdS/CdTe junction properties. The highest concentration achieved with antimony was around 10¹⁶ cm⁻³; further increases did not lead to higher V_{OC}, the maximum V_{OC} attained at about 830 mV. SCAPS simulations suggested that a back contact barrier and/or relatively high defect concentrations were responsible for the further increase in V_{OC} (Zhao et al. 2009).

Currently, the inorganic compound semiconductors with a binary structure and chemical composition of V₂-VI₃, such as Sb₂Se₃, have been gaining increasing attention. This is due to their exceptional optical and electrical characteristics, which make them highly suitable for utilization in thin-film solar cells (Chen et al. 2015). In 2011, Patrick and Giustino conducted research on Sb₂Se₃, examining its potential as a charge transfer medium in dye-sensitized solar cells (Patrick and Giustino 2011a). Additionally, it has been studied as a possible anode material for sodium-ion batteries, as well as in the thermoelectric and photodetector industries, and as a topological insulator. Sb₂Se₃ is a possible option for the p-type absorber layer in thin film solar cells because of its high optical absorption efficiency in the visible region and availability of

earth elements, Sb and Se, in contrast to CdTe and CIGS solar cell materials. Antimony selenide has a simpler composition with binary constituents, reducing the likelihood of secondary phase formation in contrast to other inorganic absorber layers in CIGS and CZTSSe solar cells (Zeng et al. 2016).

Recent research on Sb_2Se_3 has revealed unexpected complexity in its intrinsic defect chemistry, challenging the conventional understanding of binary properties. Liu and colleagues (Liu et al. 2017) identified five inherent point defects in Sb_2Se_3 , including substitutions, vacancies, and one interstitial defect. They discovered that in Se-poor conditions, deep donor defects like defect at Sb present at Se site (Sb_{Se}) and V_{Se} predominated, while in Se-rich conditions, shallow acceptor defects like Se_{Sb} and inert defects like Se_i were more common. However, Huang et al. (Huang et al. 2019) classified all point defects into three types: five antisites, five vacancies, and non-equivalent interstitials (Sb_i , Se_i). They identified $\text{Sb}_{\text{Se}1}$, $\text{Sb}_{\text{Se}2}$, and $\text{Sb}_{\text{Se}3}$ defects as donor defects and $\text{Se}_{\text{Sb}1}$ and $\text{Se}_{\text{Sb}2}$ as acceptor defects. At the same time, Savory and Scanlon (Savory and Scanlon 2019) proposed that these defects are amphoteric, acting as both electron and hole traps, respectively. Overall, Sb_2Se_3 exhibits unexpected complexity in its intrinsic defect chemistry, challenging conventional semiconductor understanding.

Furthermore, Virt et al. investigated the properties of Sb_2S_3 and Sb_2Se_3 thin films deposited by the pulsed laser deposition method. It was found that the deposited films had a polycrystalline structure. The band gap width for the Sb_2Se_3 and Sb_2S_3 films was determined by analyzing their absorption spectra, resulting in widths of 1.66 and 2.12 eV, respectively (Virt et al. 2013). Several studies have been conducted on the impact of Mg and Fe dopants in Sb_2Se_3 thin films (Li et al. 2016b). Lai et al. studied the optical properties of electrochemically deposited Sb_2Se_3 thin films for use in solar cells (Lai et al. 2012; Shi et al. 2012). PVD methods in superstrate configuration have achieved a device efficiency record of approximately 6% (Wang et al. 2017). Using commercially available Sb_2Se_3 powders as source material, Zhou et al. achieved a superstrate Sb_2Se_3 solar cell with an efficiency of approximately 5.6% (Zhou et al. 2015). Thin films of Sb_2Se_3 have been grown through the process of thermal evaporation and selenization of the metal stack by DC sputtering (Kaito et al. 1998; Li et al. 2017; Liu et al. 2014;

Maghraoui-Meherzi et al. 2013; Yuan et al. 2016). A study conducted by Li et al. aimed to examine how sodium doping affects the properties of Sb_2Se_3 thin films created through rapid thermal evaporation (Li et al. 2016a). Due to its Q1D ribbon-like structure, Sb_2Se_3 displays anisotropy in charge-transport property, resulting in varied electrical conductivity. Sb_2Se_3 typically exhibits weak p-type conductivity due to its low intrinsic charge carrier concentration of around 10^{13} cm^{-3} . However, certain studies suggested that extrinsic doping can lead to n-type conductivity (Chen et al. 2017a).

1.8 Scopes of the work:

From a materials-science perspective, the difficulties and necessary research for interface engineering of thin-film solar cells using inorganic-compound semiconductors are not thoroughly studied up to this day. In theory, defining optimal device structures from physical considerations is straightforward. However, to bring these structures in real, sophisticated processing strategies are required to overcome the limitations of many materials. Thin-film solar cells could benefit from a deeper investigation into their causes and consequences.

Comprehensive literature review revealed that CdTe, ZnTe, CdSe, ZnSe, Sb_2Se_3 , and Sb_2S_3 are the important photovoltaic materials. CdTe, for instance, is utilized as the absorber layer in thin film solar cells. It has been discovered that the PCE of the solar cell may be improved by employing different materials for the various layers of the cell. However, there have been limited attempts to synthesize and investigate these materials from this perspective. Additionally, there is a lack of theoretical knowledge about these systems, which is necessary for their effective utilization in the device. Therefore, this work focuses on modeling and investigation of various semiconductor thin films and their hetero-structures using Density Functional Theory (DFT). Through first-principles calculation, various properties of the semiconductor thin films and their heterostructure can be examined. The primary objectives of the thesis content are outlined below.

1.9 Objectives:

1. Optimize the growth condition of different telluride-based semiconductor thin films and their heterostructure by using the thermal evaporation technique.

2. To study the structural, morphological, compositional, optical, and electrical properties of the grown thin films and their hetero-structures.
3. To perform a detailed theoretical investigation of the synthesized films using ab-initio density functional theory.
4. To study the suitability of these materials in photovoltaics and other device applications.

CHAPTER 2

EXPERIMENTAL, THEORETICAL METHODOLOGY, AND CHARACTERIZATION TECHNIQUES

Overview:

This chapter outlines the experimental procedure for depositing thin films and numerous characterization approaches for examining the properties of the deposited samples. It also provides a detail description of the first principles theory and the computational methods that are used to performed theoretical studies.

2.1 Experimental Methodology:

The preparation of good-quality thin films is one of the critical requirements of the study. There are various methods for preparing thin films, which can be divided into four groups: physical vapor deposition (PVD), sputtering, chemical vapor deposition (CVD), and chemical deposition. Physical vapor deposition methods include resistive heating, electron beam evaporation, RF heating, Laser evaporation, flash evaporation, and more. The sputtering method includes glow discharge sputtering, triode sputtering, ion plating, magnetron (direct and reactive) sputtering, ion beam sputtering, and RF sputtering. The CVD process involves chemical reactions, such as chemical transfer, thermal decomposition (pyrolysis), reduction, oxidation, nitride, and carbide formation. The thermal evaporation method is the most suitable PVD technique for growing thin films. It has advantages such as a very high deposition rate, low material consumption, low cost of operation, and minimal impurities associated with the growing layer. The tendency to form oxides is also considerably low and has high reproducibility. (Bacewicz 1997)



Fig 2.1 : Experimental setup for thermal evaporation

The thermal evaporation method involves placing a source in a filament, boat, or crucible and positioning a substrate at a distance opposite the evaporation source. Molybdenum, Tungsten, or Tantalum boats with higher melting points than the evaporator material are typically used for depositing samples. Both the substrate and

source are located within the vacuum chamber; it is crucial to maintain a pressure range of 10^{-5} Torr throughout the deposition process. A pumping system consisting of a diffusion and rotary pump is used to achieve this. Pressure is measured using the Pirani and penning gauge at different deposition stages. The desired vapor pressure of the source material is achieved by heating the boat to a higher temperature. The concentration of the growth species in the gas phase is controlled by adjusting the source temperature and carrier gas flux.

In the present work, the tantalum boat was used to deposit the thin films at the optimum residual pressure of 10^{-5} Torr. The conventional gravimetric method was used to determine the thickness of the deposited samples.

$$t = \frac{m_2 - m_1}{\rho A} \quad (2.1)$$

(Here, ' m_1 ' and ' m_2 ' denotes the mass of the glass substrate and film-coated glass substrate, respectively. ' ρ ' is the density of the bulk material, and ' A ' is the area of the deposited sample.

2.2 Characterization Techniques:

After the successful deposition of our thin film, we proceeded to characterize them using different characterization techniques such as X-ray diffraction, Scanning electron microscopy, Energy dispersive analysis by X-rays, Scanning electron microscope, UV-Vis spectroscopy, etc. the detailed working principles of these techniques are described in the following.

2.2.1 X-ray diffraction (XRD):

X-ray powder diffraction (XRD) is a rapid analytical technique primarily used for phase identification of a crystalline material and can provide information on unit cell dimensions. The analyzed material is finely ground, homogenized, and the average bulk composition is determined. X-ray diffractometer consists of three basic elements: an X-ray tube, a sample holder, and an X-ray detector. X-rays are generated in a cathode ray tube by heating a filament to produce electrons, accelerating the electrons toward a target by applying a voltage, and bombarding the target material with electrons. When electrons have sufficient energy to dislodge the inner shell electrons of the target

material, characteristic X-ray spectra are produced. These spectra consist of several components, the most common being K_{α} and K_{β} . The most commonly used diffractometer is known as the Debye-Scherrer diffractometer. X-ray diffraction is based on constructive interference of monochromatic rays and a crystalline sample. These X-rays are generated by a cathode ray tube, then filtered to produce monochromatic radiation and collimated to concentrate and directed towards the sample. The interaction of the incident rays with the sample produces constructive interference and a diffracted beam when Bragg's condition is satisfied. These diffracted beams are detected, processed, and counted. By scanning the sample through a range of 2θ angles, all the possible diffraction directions of the lattice should be attained due to the random orientation of the powdered material. (Zachariasen 1967) Conversion of the diffraction peaks to d- spacings allows the identification of the material because each material has a set of unique d-spacings. Typically, this is achieved by comparison of d-spacings with standard reference patterns. The interplanar spacing (d) of all the deposited samples is calculated by using Bragg's law,

$$n\lambda = 2d\sin\theta \quad (2.2)$$

'n' is the order of diffraction, ' λ ' is the wavelength of the X-rays, and ' θ ' is the glancing angle.

The diffraction data obtained for the deposited samples are compared with the powder diffraction files, which are produced by the Joint Council on Powder Diffraction Standards (JCPDS).

The average grain size (D) of the samples is calculated by using Debye Scherrer's formula,

$$D = \frac{0.94\lambda}{\beta\cos\theta} \quad (2.3)$$

Furthermore, the lattice constant of the deposited samples is obtained by using the interplanar spacing and the Miller indices (h k l). For the cubic system,

$$a = \frac{d}{\sqrt{h^2+k^2+l^2}} \quad (2.4)$$

2.2.2 Scanning electron microscope (SEM):

To create an image, SEM moves a focused electron beam across a surface. The electrons in the beam interact with the sample, and the resulting signals can reveal the surface's topography and composition. Secondary electrons (which create SEM images), backscattered electrons (which determine crystal structures and orientations of minerals), photons (which produce characteristic X-rays used in elemental analysis), visible light, and heat are all examples of such signals. In an electron microscope, the electron beam can be focused to a tiny spot size using electrostatic lenses. The fine beam is scanned on the sample surface using a scan generator, and the detector collects backscattered electrons. The electron collector amplifies the signal from the scan generator, creating an image of the sample surface. To minimize filament and sample damage from air molecules and electron collisions, a vacuum chamber is used. One major drawback of the SEM is that it cannot be used for direct analysis of highly resistive samples because they become charged from incident electrons, rendering the images unreliable. Thus, insulating solids are made conductive by coating them with a very thin metal film, such as gold or platinum (< 10 nm), without compromising any crucial aspects of the sample.

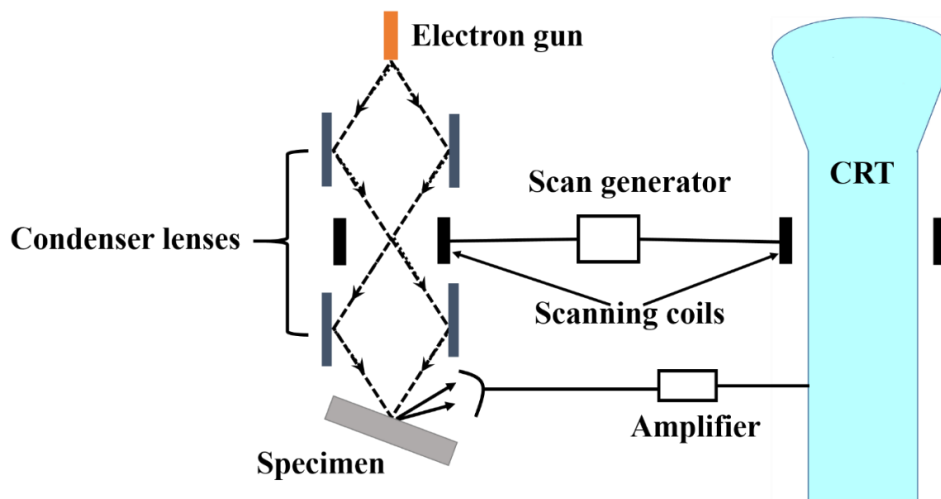


Figure 2.2 A typical sketch of a Scanning Electron Microscope

The electron microscope is also used to know the composition of the sample by Energy Dispersive Analysis of X-rays (EDAX). (Gordillo et al. 1995a)

2.2.3 Energy dispersive analysis by X-rays (EDAX):

When the primary beam interacts with atoms in a sample, it triggers shell transitions that emit X-rays. These X-rays have an energy that is specific to the parent element. By detecting and measuring these X-rays, we can analyze the elemental composition of the sample. EDS is a quick way to obtain qualitative analysis and, with proper standards, quantitative analysis of the sample's elemental composition. It has a sampling depth of 1-2 microns and can also be used to create maps and line profiles that show the distribution of elements on the sample surface.

In this present work, the morphological and compositional studies are carried out by using the Carl Zeiss electron microscope.

2.2.4 UV –Vis spectroscopy:

The electronic structure and band gap transitions between valence and conduction bands are determined by using this characterization technique. This method investigates bulk, colloidal, thin-film, and nanostructured metals, semiconductors, and insulators. There is an optical band gap in semiconductors and some insulators. Absence of absorption occurs when the energy of the incident photon is insufficient to excite the electrons from the valence band to the conduction band. An abrupt increase in absorption occurs when the energy of the incident photon is high enough to excite the electrons to the conduction band minimum; the photon with energy above that is also absorbed by the material (Chander and Dhaka 2016).

In this study, the deposited samples' absorbance spectra were obtained using the UV-Vis NIR spectrometer 3600. There are three detectors in this tool. InGaAs and cooled PbS detectors are available for the near-infrared area, while photomultiplier tubes (PMT) are given for the UV and visible wavelengths. The UV-3600 Plus, in contrast to conventional spectrophotometers, uses an InGaAs detector to cover the crossover region and guarantees great sensitivity throughout the whole measured wavelength range.

The coefficient of absorption (α) can be calculated from the transmission spectra by the following relation,

$$T = \frac{I}{I_0} = \exp(-\alpha t) \quad (2.5)$$

Where 'I' is the intensity of transmitted rays, 'I₀' is the intensity of incident rays, and 't' is the thickness of the sample.

For direct band gap semiconductors, the band gap can be calculated by using Tauc's relation (Tauc and Menth 1972)

$$\alpha h\nu = B(h\nu - E_g)^{\frac{1}{2}} \quad (2.6)$$

Where 'B' is the band tailing parameter. Tauc's plot ($(\alpha h\nu)^2$ versus $h\nu$ (in semiconductors)) is used to determine the band gap of the material. The variation of the $(\alpha h\nu)^2$ with the $h\nu$ is linear in certain regions. The intercept of this line on the $h\nu$ axis at the $(\alpha h\nu)^2 = 0$ gives the band gap of the material.

2.2.5 Electrical characterization:

To fabricate any electronic devices, the electrical properties of the material should be known. The electrical properties like carrier type and resistivity of the material play a key role in designing the devices. The current-voltage characteristics curves are generally used to calculate all the electrical parameters. (Rosa 1984)

The resistivity of the samples can be calculated by using Ohm's law,

$$\rho = \frac{RA}{L} \quad (2.7)$$

Where 'R' represents the resistance of the samples, 'A' is the active area on which film is deposited, and L is the distance between the electrodes. Here 'R' is calculated from the slope of current versus voltage characteristics. In this thesis, current-voltage (I Vs. V) characteristics are studied by using a Keithley-source meter- 2400.

The hot probe method is used to determine the conductivity of the samples. The sample is probed with a voltmeter or an ammeter while a heat source, like a soldering iron, is

placed on one of the leads. Because of the heat, the majority charge carriers (holes in p-type and electrons in n-type) will travel away from the lead, and more carriers can be produced. As a result, there will be a difference in current/voltage. For instance, if a heat source is put on the positive lead of a voltmeter connected to an n-type semiconductor, the area around the heat source/positive lead will become positively charged, giving rise to a positive voltage measurement. Similarly, for p-type material, the negative voltage will be obtained. The majority free carriers that are thermally excited can be explained as the translation from the hot probe to the cold probe. This type of translation is named the diffusion of charge carriers. The translation of the majority of carriers determines the direction of the multimeter's current reading. Because of this, the cold probe continues to be agnostic. In contrast, the area around a hot probe becomes charged with minority carriers; thus, the open circuit voltage or short circuit current can be used to identify the material.

2.2.6 Capacitance Vs. Voltage characterization:

The technique of capacitance-voltage profiling is used to describe the electrical properties of semiconductor materials and devices. The applied voltage is changed while measuring and plotting the capacitance as a function of voltage. In this method, a depletion area is made using a metal-semiconductor junction (Schottky barrier), a p-n junction, or a MOSFET. This region may contain ionized donors and electrically active defects but not the conducting electrons or holes. Therefore, the depletion region behaves as a capacitor. By adjusting the voltage across the junction, the depletion width can be altered. The doping profile and electrically active defect densities of the semiconductor are revealed by the correlation between the depletion width and the applied voltage. In semiconductor physics, this method is widely used to characterize the bipolar junction transistor, organic thin film transistor, photovoltaic cells, and photodiodes. The junction capacitance and the biasing voltage are related by the following expression:

$$\frac{1}{C^2} = 2 \left[\frac{(V - V_b + \frac{kT}{q})}{q \epsilon_0 \epsilon_r N A^2} \right] \quad (2.8)$$

‘V’ and ‘V_b’ correspond to an applied voltage and built-in potential, respectively. ‘A’ is the active area of the device, and ‘N’ is the doping concentration.

2.3 Theoretical approach:

Having a comprehensive understanding of a material's properties at the atomic level is crucial for its application in devices. Results obtained from electronic structure calculations serve as the foundation for determining a material's fundamental characteristics. This section will cover the basics of electronic structure theory and the first-principles methods used to calculate electronic structures. Additionally, we will discuss the theoretical background of the charge transfer mechanism and the appropriate alignment of the band edge positions, necessary for solar cell applications.

The study of classical mechanics is helpful in examining the characteristics of large-scale materials. However, when dealing with materials at the nano-scale range, classical mechanics is not sufficient in calculating microscopic properties. In this case, quantum mechanics is necessary to analyze the properties of low-dimensional materials like quantum dots, nanorods, thin films, and other nanomaterials. The well-known *Schrödinger's* equation (SE) for a stationary system is governed by $\hat{H}\psi = E\psi$ determines the dynamics of the quantum mechanical systems. Where ‘ \hat{H} ’ represents the Hamiltonian operator of the system represented by the total energy of the system, ‘ ψ ’ stands for the state vector of the system, and ‘E’ is the energy of the system.

Hamiltonian operator for the system with ‘M’ numbers of nuclei and ‘N’ numbers of electrons is defined as,

$$\hat{H} = \frac{-\hbar^2}{2} \sum_{I=1}^M \frac{1}{M_I} \nabla_I^2 - \frac{\hbar^2}{2m_e} \sum_{i=1}^N \nabla_i^2 + \frac{e^2}{4\pi\epsilon_0} \sum_{I=1}^M \sum_{J>I}^M \frac{Z_I Z_J}{|R_I - R_J|} - \frac{e^2}{4\pi\epsilon_0} \sum_{i=1}^N \sum_{I=1}^M \frac{Z_I}{|R_I - r_i|} + \frac{e^2}{4\pi\epsilon_0} \sum_{i=1}^N \sum_{j>i}^N \frac{1}{|r_i - r_j|} \quad (2.9)$$

The first two terms are the kinetic energy operator of the nuclei and electrons, respectively. The third, fourth, and fifth terms are related to the potential energy operators of nucleus-nucleus interaction, nucleus-electrons interaction, and electrons-electrons interaction, respectively. Here I and J run over the M Nuclei. On the other hand, i and j represent the N nos. of electrons in the system. For simplification, the

atomic constants (e , m_e , \hbar , and $4\pi\epsilon_0$) are set to 1, and then the above Hamiltonian can be written as,

$$\hat{H} = \frac{-1}{2} \sum_{I=1}^M \frac{1}{M_I} \nabla_I^2 - \frac{1}{2} \sum_{i=1}^N \nabla_i^2 + \sum_{I=1}^M \sum_{J>I}^M \frac{Z_I Z_J}{|R_I - R_J|} - \sum_{i=1}^N \sum_{I=1}^M \frac{Z_I}{|R_I - r_i|} + \sum_{i=1}^N \sum_{j>i}^N \frac{1}{|r_i - r_j|} \quad (2.10)$$

We can construct the SE corresponding to this Hamiltonian, and the solution will give the energy levels of a molecule. Note that the Hamiltonian depends on the nos. of electrons and nuclei in the system. It is difficult to solve the equation for the system with more nos. of electrons and nuclei. For example, the wave function must be solved using $3M$ (nuclear) + $3N$ (electronic) variables in a system with M nuclei and N electrons. This suggests that solving the SE is essentially impossible. The need for approximations is amply highlighted by such a case.

2.3.1 Born-Oppenheimer Approximation:

The approximation is based on the fact that nuclei have a greater mass than electrons, making them almost stationary compared to electronic mobility. Since the kinetic energy of the nucleus is much lower than that of the electrons, it is not considered in the calculation. In addition, the potential energy operators of nucleus-nucleus interaction are constant and can be ignored due to the fixed position of the nuclei. By making these approximations, the Hamiltonian is simplified only to include the electron's variables, known as the electronic Hamiltonian.

$$\hat{H}_e = \frac{-1}{2} \sum_{i=1}^N \nabla_i^2 - \sum_{i=1}^N \sum_{I=1}^M \frac{Z_I}{|R_I - r_i|} + \sum_{i=1}^N \sum_{j>i}^N \frac{1}{|r_i - r_j|} \quad (2.11)$$

Corresponding SE can be constructed as $\hat{H}_e \psi_e = E_e \psi_e$, 'e' denotes the terms associated with the electrons. The solution to this SE will be obtained by varying the position of the nucleus 'R'. Which in turn gives the energy Eigen value as a function of nucleus

position 'R.' If the system consists of an 'M' number of nuclei and an 'N' number of electrons, then the BO approximation reduces the number of variables for the wave function from $3M+3N$ to only $3N$. This approximation calculates the electronic structure of a system by considering only the electronic part.

Even using the BO approximation, computing the SE for an atom with N electrons is a computationally intensive process because of the multiple electron-electron repulsion factors. An analytic solution of interacting electronic Hamiltonian is not possible to obtain. Therefore, one can use a numerical technique based on variational principles to obtain the solution of the electronic Hamiltonian equation.

2.3.2 Hartree-Fock Approximation:

In 1948, Douglas Hartree proposed a method to calculate the best possible one-electron wave function, which was further developed by V. Fock and J.C. Slater and classified as the Hartree-Fock self-consistent field approach. (HF-SCF). According to this approximation, the many-body problem is treated as a collection of N-independent particle problems. The N-electron wave functions are approximated by an antisymmetrized product of the N one-electron wave function, which is referred to as the Slater determinant. Using the variational method, one can obtain a set of N -coupled equations for the N spin orbitals. The Hartree wave function and energy of the system are obtained by solving these equations.

As previously stated, no analytical method exists for solving many-electron systems, so a numerical method called the self-consistent field method is used. This non-linear method solves the Schrödinger equation for each electron, and the process is repeated for the others. The wave functions obtained from the first computation are used as the basis set for the electrons, and the computation is repeated for each electron with a new set of wave functions. This results in improved wave functions for each electron. The total energy and charge density are then calculated from the new wave function and compared to the output of the previous computational cycle (Energy and charge density) the same method will be repeated until the desired accuracy is reached. In this approximation, the electronic correlation is not fully taken into account, which shows an incorrect energy value. However, the computational cost is pretty high, making the

calculation of a large system untenable. From the above discussion, it is clear that the wave function approach governed by SE would not be straightforward for a system with a large number of atoms/electrons. The density functional theory (DFT) is an alternate technique for converting wave function-based many-electron problems of $3N$ variables to 3 variables density-based problems

2.3.3 Density functional theory:

DFT is based on the theorem that all characteristics of molecular systems may be derived by their electron density $\rho(r)$, where r is the spatial coordinates. (W. KOHN AND L. J. SHAM 1965) DFT is particularly useful because it uses particle density to reduce the N -body system's $3N$ degrees of freedom to just three spatial coordinates. This theory is one of the most extensively utilized first-principles models in the field of condensed matter physics to describe the different properties of the system, which includes not only the bulk materials but also the complex structures, e.g., molecules, nanoparticles, etc.

Improved exchange energy function approximations from the 1990s have led to a generally satisfactory agreement between DFT calculations and experimental data for condensed-matter systems. Additionally, compared to earlier approaches that relied on the complex many-electron wavefunction, like Hartree-Fock theory (Hartree 1928), (Fock 1930) and its successors, the computational costs were relatively low. There are still challenges in using DFT to precisely define intermolecular interactions, other strongly correlated systems, transition states, charge transfer excitations, and the band gap of some semiconductors, despite the advances that have been made.

2.3.4 Thomas-Fermi –Dirac approximation:

The Thomas-Fermi (TF) model was introduced by Thomas (L. H. Thomas n.d.) And Fermi (Fermi 1927) 1927, was the origin of DFT. In this approach, they adopted the electron density $\rho(r)$ rather than the wave function as the fundamental variable. The exchange and correlation of electrons were ignored in the original TF approach; later,

it was modified by the Dirac. The total energy of the system is expressed by the following equation and which is a functional of electron density.

$$E_{TFD}[\rho(r)] = A_1 \int \rho(r)^{\frac{5}{3}} dr + \int \rho(r)V_{ext}(r)dr + \frac{1}{2} \iint \frac{\rho(r)\rho(r')}{|r-r'|} dr dr' + \quad (2.12)$$

$$A_2 \int \rho(r)^{\frac{4}{3}} dr$$

The first term stands for the kinetic energy of the electrons if they were not interacting with one another; the second term represents the Columb interaction energy; the third term is associated with the classical Columb repulsion between electrons; and the fourth term is the local exchange term, which was introduced by Dirac in 1930.

The Thomas-Fermi theory gives an idea for handling the many-body system computationally. On the other hand, the theory has a lot of issues. The most significant one is that solids and molecules cannot form in this theory since it fails to explain atomic bonding. (Teller 1962) Using electron density as the fundamental variable is a good way to show how DFT works, even though it does not do a good job of describing electrons in matter.

Furthermore, in 1964, Hohenberg and Kohn (P. HOHENBERG 1964) demonstrated the accuracy of DFT as a theory of many-body systems. It is known as the Hohenberg-Kohn theorem (H-K theorem). Generally, it applies to any system of interacting particles with an external potential $V_{ext}(r)$. The two theorems on electron density, which are regarded as the basis of DFT are as follows.

2.3.4.1 H-K theorem 1:

This theorem states that the external potential $V_{ext}(r)$ is solely determined by the ground state particle density $\rho(r)$ of a system of interacting particles, except for a constant. The Hamiltonian is thus determined by the ground state particle density, except for a constant energy shift. Theoretically, the ground, as well as the excited states of many-body wave functions, can be calculated. This indicates that the ground state energy is a unique functional of electron density $\rho(r)$, which depends on three spatial coordinates. That means the $3N$ coordinates of the N -electron system are reduced to 3 spatial coordinates by considering the electron density.

2.3.4.2 H-K theorem 2:

It follows from the first theorem that the electron density in the ground state is sufficient to determine the many-body system's desired properties. But how do we verify that a particular density is the ground state density we are in search of? The second theorem proved by Hohenberg and Kohn in their 1964 contribution provides a formal prescription for how this issue should be approached. The second theorem states that there exists a universal functional $E(\rho)$, which delivers the lowest energy E_0 if and only if the input density is the true ground state density which is $\rho_0(r)$. Furthermore, by applying the variational principle, the ground state charge density can be calculated.

2.3.5 The Kohn-Sham DFT:

It should be noted that the functional form of $E(\rho)$ is unknown and remains a concern. The interaction energy with the external field has a simple, functional form and can be expressed as $\int v(r)\rho(r)dr$. However, due to electron-electron interaction, it is challenging to express electron kinetic energy and electron-electron interaction energy in terms of electron density. Kohn and Sham's solution to this problem, Kohn-Sham (KS) DFT, was published in 1965.

The KS approximation assumes that the two systems have the same ground state density while replacing the many-body system with a fictitious non-interacting system. KS DFT finds a hypothetical non-interacting system and incrementally improves it by using the variational principle instead of establishing the universal HK functional.

The electronic Hamiltonian is,

$$\hat{H}_e = \sum_{i=1}^N \frac{-1}{2} \nabla_i^2 + \sum_{i=1}^N V_{ext}(r_{ij}) + \sum_{i=1}^N \sum_{j>1}^N \frac{1}{|r_i - r_j|} \quad (2.13)$$

In equation 2.5, it is clear that the last term can be expressed as the one electron operator (V_{av} in the non-interacting system, whereas it is impossible to decouple it into the sum of terms containing only r_i and r_j . V_{av} represents the average effect of interaction. Additionally, the Hamiltonian operator in the case of a non-interacting electron system is just the sum of one electron operator.

So equation 2.13 can be rewritten as,

$$\hat{H}_e = \sum_{i=1}^N \frac{-1}{2} \nabla_i^2 + \sum_{i=1}^N V_{ext}(r_i) + \sum_{i=1}^N V_{av}(r_i) \quad (2.14)$$

Kohn and Sham created a second non-interacting system with an effective potential V_{eff} (r) to aid in calculating the ground state density and energy of the interacting system.

We can write the $V_{eff}(r_i)$ from equation 2.14,

$$V_{eff}(r_i) = \sum_{i=1}^N V_{ext}(r_i) + \sum_{i=1}^N V_{av}(r_i) \quad (2.15)$$

Then the electronic Hamiltonian will be,

$$\hat{H}_e = \sum_{i=1}^N \left(\frac{-1}{2} \nabla_i^2 + V_{eff}(r_i) \right) \quad (2.16)$$

Let's apply the variational principle to find the functional form of $V_{eff}(r_i)$

$$V_{eff}(r) = V_{ext}(r) + e^2 \int \frac{\rho(r')}{|r - r'|} dr' + \frac{\delta E_{xc}(\rho)}{\delta \rho(r)}$$

$$V_{ext}(r) + e^2 \int \frac{\rho(r')}{|r - r'|} dr' + v_{xc}[\rho(r)] \quad (2.17)$$

From 2.8 and 2.9, we can write the one-particle Kohn-Sham equation for a fictitious non-interacting system as follows:

$$\left(\frac{p^2}{2m} + V_{eff}(r) \right) \psi_i(r) = \epsilon_i \psi_i(r) \quad (2.18)$$

The wave function of a single electron is denoted by the molecular orbital, also known as the Kohn-Sham orbital, and its associated energy can be determined with the help of

the Kohn-Sham equation. From the Kohn-Sham orbital, the electron density matrix $\rho(r)$ can be written as,

$$\rho(r) = \sum_{i=1}^N |\psi_i|^2 \quad (2.19)$$

By solving the Kohn-Sham equations in a self-consistent fashion, we may be able to calculate the density of the non-interacting system in its ground state. Fig. 2.3 depicts the iterative process flow. The effective potential V_{eff} must be evaluated. Therefore, an initial assumption is made for the electron density. The Kohn-Sham equations are then solved using this in relation to the single-particle wave functions ψ_i . Following calculations, the electron density and total energy associated with these wave functions are compared to the initial guess values. This process is repeated until the data converge within a predetermined accuracy standard. When this loop reaches self-consistency, the electronic portion of the system is solved, and various physical quantities, such as eigenvalues or forces on the system's ions, can be estimated.

Later, a large number of free or paid software packages such as Vienna ab-initio simulation package (VASP), (Kresse and Furthmüller 1996a) Quantum ESPRESSO, (Giannozzi et al. 2017) Quantum ATK,(Smidstrup et al. 2020), WIEN2K,(Blaha et al. 2020) SIESTA, (Soler et al. 2002) ABINIT,(Gonze et al. 2020) CASTEP, (Segall et al. 2002) that used DFT to determine the electronic structural attributes of many-body systems. The widespread use of DFT is also significantly influenced by the accessibility of these reliable and developed software packages.

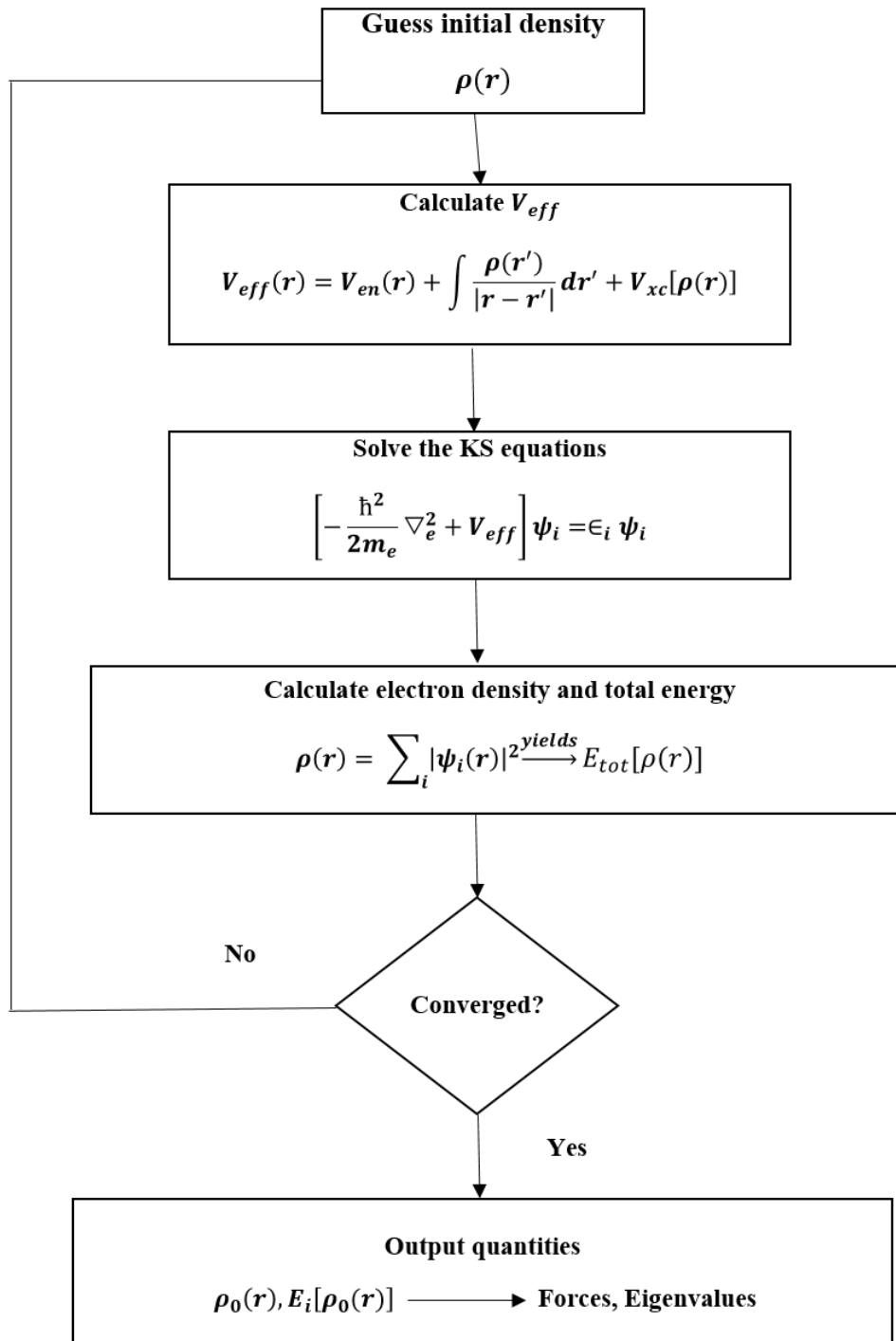


Fig 2.3: Flow chart of Kohn Sham iterative method

It should be noted that the excited states cannot be provided by DFT; only the density and energy of the ground state may be provided. In particular, the Kohn-Sham eigenvalues and eigenfunctions do not agree with the excitation energy and electron

wave functions in the real system. This is a mathematical trick used to obtain the real system's ground state density and energy via the variational principle, and it applies only to the auxiliary non-interacting system. In the DFT formalism, only the energy and density of the ground state are precise. When calculating the band gap of semiconductors and insulators, DFT is frequently incorrect. The band gap problem in DFT calculations stems from an incorrect application of the Kohn-Sham eigenvalues.

2.3.6 Exchange – correlation energy functional (E_{xc}):

It is assumed in the above-mentioned explanations that we are familiar with the functional form of exchange energy. Even if we don't know the precise form of E_{xc} , there are a few approximations that serve effectively in practical scenarios. The easiest approximation is the local density approximation;

$$E_{xc} = \int \rho(r)\epsilon_{xc}(\rho(r))dr \quad (2.20)$$

Here, the ϵ_{xc} is a function of $\rho(r)$, which is the local density. The dependency of exchange-correlation energy functional on $\rho(r)$ is identical to that in a homogeneous electron gas with the same ρ . E_{xc} can also be expressed as an extensively local functional of density because the Kohn-Sham formulation separates the long-range Hartree terms and independent-particle kinetic energy. LDA generally works well for solids because the range of the effects of exchange and correlation is quite small in most materials with average densities.

Furthermore, the generalized gradient approximation was developed, and the exchange energy functional can be expressed as,

$$E_{xc} = \int \rho(r)\epsilon_{xc}(\rho(r))F_{xc}(\rho(r),\nabla\rho(r))dr \quad (2.21)$$

ϵ_{xc} is the exchange energy functional, and F_{xc} represents the dimensionless enhancement factor. Note that the exchange-correlation density can be expressed in terms of $\rho(r)$ and $\nabla\rho(r)$.

GGA results in an exchange energy that is lower than the LDA because the exchange enhancement factor $F_x \geq 1$. GGA lowers binding energy and improves agreement with

the experiment, whereas LDA overbinds. (Martin 2004) The most extensively used versions of F_x are developed by Perdew and Wang (PW91) (Ziesche et al. 1991) and Perdew, Burke, and Enzerhof (PBE). (Perdew et al. 1996)

2.3.7 Improvement in the conventional DFT method:

2.3.7.1 Self-interaction error:

Let's realize the self-interaction error term from the above discussion. The effective potential form is shown in Eq. 2.9, where the second term is the Hartree term. What exactly does this term mean in terms of physics? This term represents the unphysical electron-electron interaction and represents the Columbic interaction between a single electron and the system's total electron density, in which the initial electron is also included. This creates the self-interaction error term. To eliminate the error term, it is essential to know the exact form of the exchange-correlation functional, and both terms can be canceled out with each other. However, it is difficult to cancel this term in any of the approximate forms of exchange-correlation functional such as LDA, GGA, etc. Due to the large Coulomb interactions involved in these terms, it may be substantial. On the other hand, it should be noted that the self-interaction energy in the Hartree-Fock approach is precisely negated by the exact exchange energy. When electrons are highly localized in strongly correlated systems, self-interaction inaccuracy worsens the situation. Semi-local density functional theory predicts that the localized electrons will become unphysically delocalized. By taking electron delocalization into account, the self-interaction error term can be minimized or eliminated altogether. Several approaches have been made to correct the self-interaction error. The most widely used approaches are DFT+U functionals and hybrid functionals. In our thesis, we have used hybrid functional to calculate the exact electronic properties of the materials.

2.3.7.2 Hybrid functional:

The self-interaction of an electron with itself is eliminated in the Hartree-Fock approach, which includes an accurate description of exchange interaction. On the other hand, The Hartree-Fock approximation excludes electron correlation resulting in a significant deviation from the experimental outcomes. Exchange and correlation are both included in DFT within a local or semi-local (as characterized by the reliance on density gradient) approximation. In this situation, the self-interaction error might be

sizable. It has been demonstrated that hybrid functionals, which include a component of precise exchange with a semi-local density functional, significantly improve the structural, thermodynamic, and electrical properties calculation for the periodic systems as well as the molecules.

The combination of exact exchange from Hartree-Fock theory with the remaining exchange-correlation energy from ab-initio is known as hybrid functionals in density functional theory (DFT). PBE0, B3LYP, and HSE are some of the hybrid functional types available. In Chapters 3 to 6, the electronic properties of the material are analyzed using the HSE functional.

HSE functional:

Splitting the Coulomb operator into short-range and long-range components and including only a small amount of short-range exchange into semi-local density functional was proposed by the HSE (Heyd-Scuseria-Ernzerhof) (Heyd et al. 2003) to significantly improve computing efficiency.

The hybrid functional form can be written as;

$$E_{xc}^{\omega} = aE_x^{HF,SR}(\omega) + (1 - a)E_x^{PBE,SR}(\omega) + E_x^{PBE,LR}(\omega) + E_c^{PBE} \quad (2.22)$$

The first term corresponds to the short-range Hartree-Fock exact exchange functional, the second and third terms correspond to the short-range and long-range elements of PBE functional, and the last term represents the PBE correlation functional. ‘a’ is the mixing parameter and the standard value of a is 1/4. ‘ ω ’ is the parameter that regulates how close the interaction is to being short-ranged and the standard value of ω is 0.2 which is referred to HSE 06 functional. At $\omega = 0$, the hybrid functional reduces to PBE0 functional.

Furthermore, in Chapter 7, another approximation, DFT+U, is used to study the electronic properties of the material.

2.3.7.3 DFT + U Functional:

The DFT+U approach is used to describe the ground state of strongly correlated systems. One of the major advantages of this method is that it uses the same DFT formalism with little modification. This is slightly more expensive to compute than the standard DFT calculation. It is observed that the computational operation for the local and semi-local DFT (LDA+U, GGA+U) can be enhanced significantly with the adjustment of Hubbard potential (U). The U correction adds a Hubbard-like term to the strong on-site Coulomb interaction of localized electrons. Valence electrons are treated with the standard DFT assumptions, while the strongly correlated electronic states (d and f orbitals) are defined by the Hubbard Hamiltonian. Two parameters used in materials science to characterize the intensity of on-site interaction are the on-site Coulomb term U and the site exchange term J. The values of U and J can be determined either through ab-initio calculation or semi-empirical methods.

The total energy for DFT+U can be expressed as (Dudarev and Botton 1998)

$$E_{DFT+U} = E_{DFT} + \frac{U - J}{2} \sum_{m,\sigma} (n_{m\sigma} - n_{m\sigma}^2) \quad (2.23)$$

Here, U and J are combined to form a single effective Hubbard-U $U_{eff} = U - J$ rather than being introduced separately into the expression. The J parameter is essential for describing the electronic structure of some types of materials, especially those subject to significant spin-orbit coupling. Hence the U_{eff} is commonly used. m and σ are magnetic and spin quantum numbers, respectively. ' $n_{m\sigma}$ ' is the orbital occupancies.

After a thorough study of the electrical properties of the materials, we proceeded further to study some important properties of the heterostructure, which are discussed as follows:

2.3.8 Charge density calculation:

When a p-type material and n-type material comes together, it is expected that the Fermi level will not be flat and continuous throughout the whole structure. Let us realize how the equilibrium will be established with respect to the junction formation. The region x

> 0 has more electrons than the region $x < 0$, i.e., the hole reach layer. As a result, the electrons and holes will start diffusing from the n-side to the p-side and p-side to the n-side, respectively. The ionized donor atoms generate the electrons on the n-side. Negatively transformed acceptor atoms are left behind when the holes close to the hetero-interface diffuse into the n-side. Similar to this, when electrons that are close to the interface region diffuse to the p-side, leaving behind the positively transformed donor atoms. Therefore, a net positive and negative charge density develops on the right and left sides of the interface, respectively, as shown in Fig 2.4.

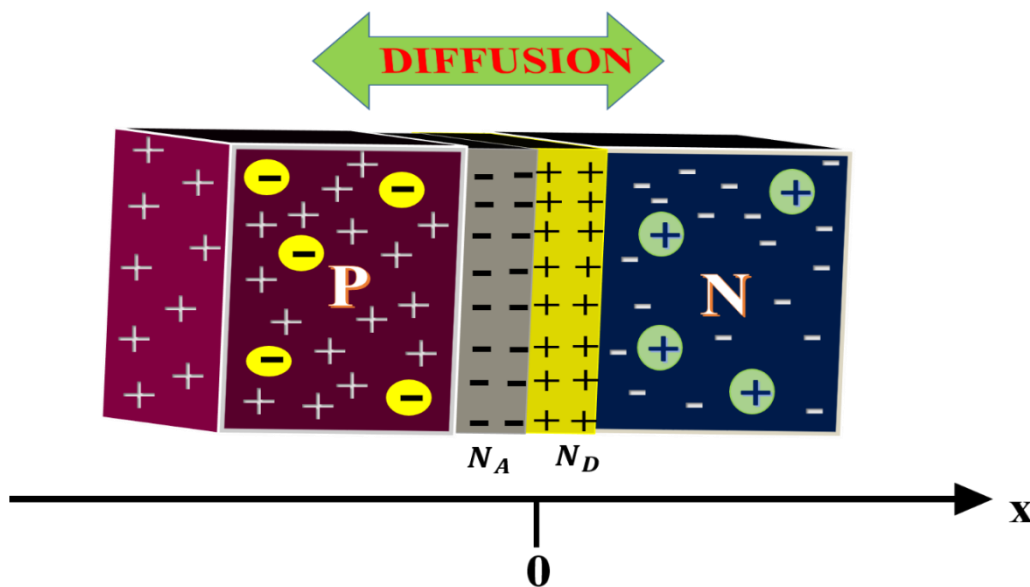


Fig 2.4: $x > 0$ is the electron reach layer, whereas the $x < 0$ is the hole reach layer, development of charge density due to the diffusion at the interface.

The shaded region is called a depletion region, where the majority charge carriers are depleted. Due to the charge densities on either side of the interface, an electric field is created that points away from the acceptor atoms or in the negative x-direction. Drift components of electron and hole currents produced by the induced electric field are in the opposite direction of the diffusive currents. The strength of the electric field grows as more electrons and holes diffuse. The process of diffusion occurs in both electron and hole currents until their respective drift components become equal and opposite to their diffusive components. At this point, the junction reaches an equilibrium state.

In the case of solar cells, the charge density plays an important role as it is a minority charge carrier device. Therefore, we studied the charge distribution in the different layers. Charge density can be calculated by,

$$\Delta\rho = \rho_{interface} - \rho_{SC1} - \rho_{SC2} \quad (2.24)$$

Note that, in the case of ρ_{SC1} and ρ_{SC2} calculation, the atomic positions kept fixed as that of $\rho_{interface}$ calculation.

2.3.9 Bader charge analysis:

An innovative way was developed by Bader to divide molecules into atoms, which is known as the Quantum Theory of Atoms in Molecules. He defined an atom solely in terms of its electrical charge density. The zero flux surfaces are used to divide the atoms.

A zero-flux surface is any two-dimensional surface where the density of charges in the perpendicular direction to the surface is minimal. In most cases, keeping the atoms at a safe distance apart is preferable when the charge density is at its lowest. We have used Bader's theory to understand the charge transfer process. For instance, the total electronic charge of an atom can be roughly approximated by the charge contained within the Bader volume. The charge distribution is used to measure the multiple moments of the interacting atoms (or molecules). The theory also offers a concept of chemical bonding that includes bond strength measurements in numerical form. Additionally, this theory quantifies the charge transfer. Bader charge analysis is used to determine the charge of each atom by comparing it to the valence electrons of a neutral atom in the least energy state. A positive charge in this notation denotes the electrons.

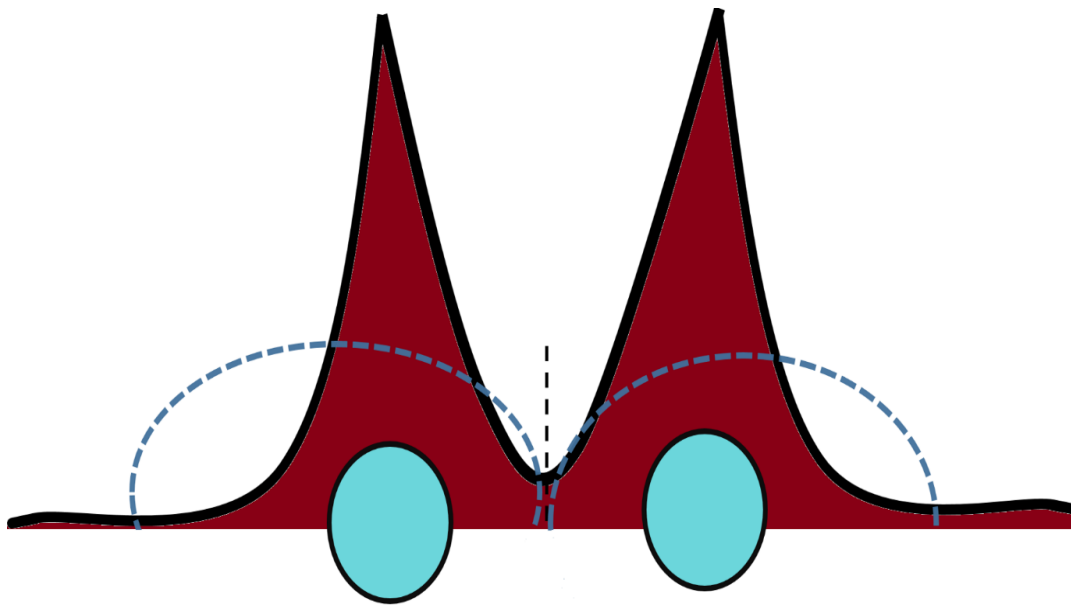


Fig 2.5: Two atoms (cyan solid circles) are used to show the Bader charge analysis in one dimension. The variation in electron density in one dimension is shown by the black solid line. A black dashed line designates the location of the zero-flux surface between the two atoms, while a blue dashed circle designates the Bader volume of each atom.

2.3.10 Band alignment of the heterostructure:

When 'N' atoms are brought together to form a solid, their electrons interact to produce 'N' closely spaced energy levels rather than discrete energy levels, leading to the formation of bands of permissible energies. From the bottom up, the electrons occupy the available bands. The highest occupied molecular orbital (HOMO) may correspond to the energy value inside a band. Then there are many more possible states with slightly higher energies. For instance, applying an electric field causes the electrons to accelerate, gain a small amount of energy, and shift their energy levels upward. This class of materials is called metals. On the other hand, the HOMO of the specific material may be separated from the lowest unoccupied molecular orbital (LUMO) by a certain energy spectrum gap which is known as the band gap of the material. In this scenario, the extra energy in the form of electric fields cannot be readily accepted by the electrons. The closest energy state will be on the other side of the energy band gap. They would get more energy if they accelerated, but there isn't a condition that has just a little bit more energy. Consequently, these materials will react to electric fields or electromagnetic radiation differently than metals. The term "insulator" refers to a class

of materials where the gap is exceptionally high ($E_g > 4\text{eV}$), and When the gap is small, it is categorized as a semiconductor.

We can study the electronic properties of the material by using the DFT. Further, we can get the energy spectrum of the material along with the HOMO and LUMO positions. The band gap is physically significant, yet their absolute positions are insignificant. As a result, we require a framework that enables us to align the HOMO and LUMO positions, respectively, i.e., the valence and conduction band edges concerning some kind of unchanging, physical reference. Here, we have considered the vacuum level as the reference.

Calculation of work function:

The bulk material is not at all necessary for a vacuum calculation. This is straightforward to explain because the definition of the work function is described as removing one electron from the surface. The work function can be estimated using the density-functional theory (DFT) technique, which is based on the electrostatic potential across the material-vacuum interface. The next task is to calculate the average electrostatic potential for a variety of out-of-plane distances and verify that it saturates (if the vacuum is sufficiently thick, this shouldn't be a problem). This saturated energy level is known as the vacuum level. At absolute zero, the work function can be defined by the following equation:

$$\varphi = E_{vac} - E_f \quad (2.25)$$

Determination of band edge position:

The slab structure properties show the near-surface environment, and this is an important parameter to control the work function of the system. Therefore, in this thesis, the surface band gap of the semiconductors is taken into consideration rather than their bulk counterparts. Band offsets can be traced back to two primary factors: band discontinuities and the intrinsic potential at the interface. First, band discontinuities arise because semiconductors have varying band gaps. All these breaks can be broken down into the valence band and conduction band. On the other hand, the built-in

potential is generated due to the charge imbalance at the interface. This can be explained by Poisson's equation. The band bending may be observed close to the interface.

Linear response theory has been proven to be the best theory to predict the band offset. This theory proposes that interface dipoles play a crucial role in band alignment. Interface dipoles, which look like ions but are mathematical constructions based on differences in bulk and interface charge densities, are not real. First principle calculations provide the basis of the linear response theory. The objective of this calculation is to solve the quantum mechanical equations without using any experimental data. According to this theory, the band offset is the sum of two terms, the first of which is intrinsic and is determined by the bulk properties. The second term, which depends on the interface geometry, vanishes for isovalent and abrupt non-polar heterojunctions.

This led to the next step, which involved estimating the band edge positions of the CdTe using the Mulliken electronegativity rules. (Liu 2015) The position of the CBM and VBM concerning the vacuum level has been calculated by using the following equations,

$$E_{VB} = \chi - E_e + \frac{1}{2}E_g \quad (2.26)$$

$$E_{CB} = E_{VB} - E_g \quad (2.27)$$

Here E_{VB} and E_{CB} are the edge potential of the valence band and conduction band, respectively. ' χ ' is the Mulliken electronegativity(Guo et al. 2017), and E_g is the band gap of the material.

2.4 Summary:

This chapter describes the several synthesis procedures, characterization techniques, and computational methodologies followed in the thesis from chapter 3 to chapter

CHAPTER 3

PREPARATION AND PROPERTIES OF CdTe THIN FILMS DEPOSITED AT DIFFERENT SUBSTRATE TEMPERATURES

Overview:

This chapter describes the optimized condition for the deposition of n-CdTe thin films. The optimization process reveals that the substrate temperature plays a crucial role in achieving the stoichiometry condition. Therefore, the structural, morphological, elemental, optical, and electrical properties of the CdTe thin films were studied by changing the substrate temperature.

3.1 Introduction:

For the past two decades, a class of II-VI compound semiconductors has become dominant in device fabrication, such as photovoltaic cells and light-emitting diodes (Yuan et al. 2021)(Kagan et al. 2016). Among them, CdTe is the most promising material owing to its high absorption coefficient (Shaaban et al. 2009), direct band gap (Ismail and Gould 1989)(Chopra and Das 1983), low production cost (Wu 2004), and more stable in the thin film form. (Dobson et al. 2000) A few micrometer thicknesses of CdTe thin films can absorb more than 90% of the incident photon. According to the theoretical calculations, the semiconductor's band gap energies ranging from 1.00 to 2.00 eV are suitable candidates for solar energy conversion. Its direct band gap (1.5 eV), close to the ideal value for the maximum solar energy conversion, supports its applicability for solar cell fabrication. The significant advantage of this material is that it exhibits both p-type and n-type conductivity. Recently, the CdTe solar cell with a CdS window layer has attained an efficiency of 16 %, which is cheaper than the conventional Si solar cell (Çetinkaya et al. 2022). Several deposition techniques have been adopted to deposit the CdTe thin films, such as molecular beam epitaxy (Ringel et al. 1991a), electron beam evaporation (Mathuri et al. 2016) (Abd El-Raheem et al. 2009), chemical vapor deposition (CVD) (Hartley et al. 2001)(Feng et al. n.d.), Sputtering (Compaan et al. 2004), pulsed laser deposition (González-Alcudia et al. 2008), closed space sublimation (Kim et al. 2014), thermal evaporation (Shreekanthan et al. 2006b), and screen printing (Nakano et al. 1986). Among all these, physical vapor deposition has several advantages that restrict impurities' growth and significantly reduce oxide formation. Furthermore, the slow deposition rate makes forming polycrystalline thin films possible. The thin films' structural, morphological, electrical, and optical properties explicitly depend on deposition parameters such as deposition duration, source-to-substrate distance, and substrate temperature (T_s), substrate material, and annealing temperature. All the deposition parameters must be optimized to get the desired properties of the CdTe thin films. The substrate temperature is pivotal in obtaining stoichiometric, crystalline, good-quality thin films.

A thorough experimental analysis of the CdTe thin films has been conducted. However, to comprehend the electrical structure of CdTe thin films and their suitability for PV

cells, one must thoroughly understand their electronic properties and band edge positions. When an electromagnetic wave interacts with a crystal, it is anticipated that the electronic structure of the crystal will be altered. The optical properties had been studied to understand the semiconducting thin films' band structure. Furthermore, optical studies have given rise to exciting optical phenomena that have significantly illuminated thin films' electronic structure. The optical band gap and the type of optical transition can be concluded from the optical absorption studies.

In this chapter, the properties of the CdTe thin films were studied by varying the substrate temperatures. The electronic properties of thin films were comprehensively explored through density functional theory.

3.2 Methods:

3.2.1 Experimental methodology:

The thermal evaporation technique was used to deposit the CdTe thin films on a glass substrate at different substrate temperatures. The pressure was maintained at less than 5×10^{-6} Torr during the synthesis process using a diffusion pump backed by a rotary pump. CdTe powder (Alfa Aesar), purity of 99.9999%, was used to deposit the thin films. Firstly, the glass substrate was dipped in the chromic acid for 48 hours to eliminate the dirt or stain on the surface. Further, it was cleaned with detergent, distilled water, and acetone, followed by ultrasonic cleaning. Then it was kept in the air annealing chamber at a constant temperature of 200°C for 5 hours before deposition. A tantalum boat was used as a source. The films were prepared at different T_s to get the stoichiometry films. The deposition rate was maintained at nearly 46 nm/min. CdTe powder was evaporated from a boat by applying a constant current. The thickness of the film was measured by the gravimetric method, and it was maintained at nearly 420nm. The structural properties of the films were demonstrated by the Rigaku Miniflex600 X-Ray diffractometer ($\lambda_{CuK\alpha} = 1.5402 \text{ \AA}$). The deposited films' surface morphology and elemental composition were studied using the Ultra 55 scanning electron microscopes. The Shimadzu MPC3600 UV–VIS–NIR spectrometer was used to study the absorption spectra of deposited samples in the 300nm–2000 nm wavelength range. The samples' electrical properties were analyzed using the Keithley 2400 source meter. The conductivity of the sample was measured by using the hot probe method.

3.2.2 Theoretical methodology:

To gain a better understanding, The Density Functional Theory (DFT) calculations were used to investigate the electronic structure of CdTe. The projected augmented wave (PAW) method, as implemented in the Vienna ab initio simulation package (VASP) (Kresse and Furthmüller 1996b), was used. Generalized gradient approximation (GGA) has been used, considering Perdew- Burke- Ernzerh (PBE) parameterization scheme to estimate the exchange and correlation potential. The Van Der Waal's (vdW) interaction was introduced in the system employing dispersion correction for the density functional DFT-D3 method (Grimme et al. 2010a). A high wave function cut-off of 500 eV and force convergence criteria 0.01 eV/Å was used to obtain accurate results. Begin with the optimum bulk geometry of the CdTe system obtained. Then the (110) surface slabs were constructed from the optimized bulk geometry and stacked along the normal direction. A sufficient vacuum of 10Å thickness along the normal direction inside the unit cell has been considered during the slab and surface calculations to avoid the interaction between periodic images. Finally, the hybrid-DFT calculation using Heyd-Scuseria-Ernzerhof (HSE06) hybrid functional with 25% Hartree-Fock exchange energy contribution was used to estimate the proper bandgap and the band edge position (Heyd et al. 2003).

3.3 Results and discussions:

3.3.1 Experimental outcomes:

3.3.1.1 Structural analysis:

The XRD pattern of CdTe thin films at the elevated substrate temperatures is depicted in Fig.3.1. The predominant peak at a 2θ value of 23.74° for CdTe thin films was observed. The reflection from the (111) planes of the CdTe corresponds to the value of 2θ , consistent with the reported literature (Rogach 2000) JCPDS (15-0770) CdTe. At higher substrate temperatures, two extra peaks and the predominant peak appear for the films at the angular positions of $2\theta = 39.22^\circ$, 46.29° , as depicted in Fig 3.1. These additional peaks mainly correspond to the reflection from (220) and (311) planes. It was confirmed that all the deposited thin films possessed cubic structures and were poly-crystalline in nature.

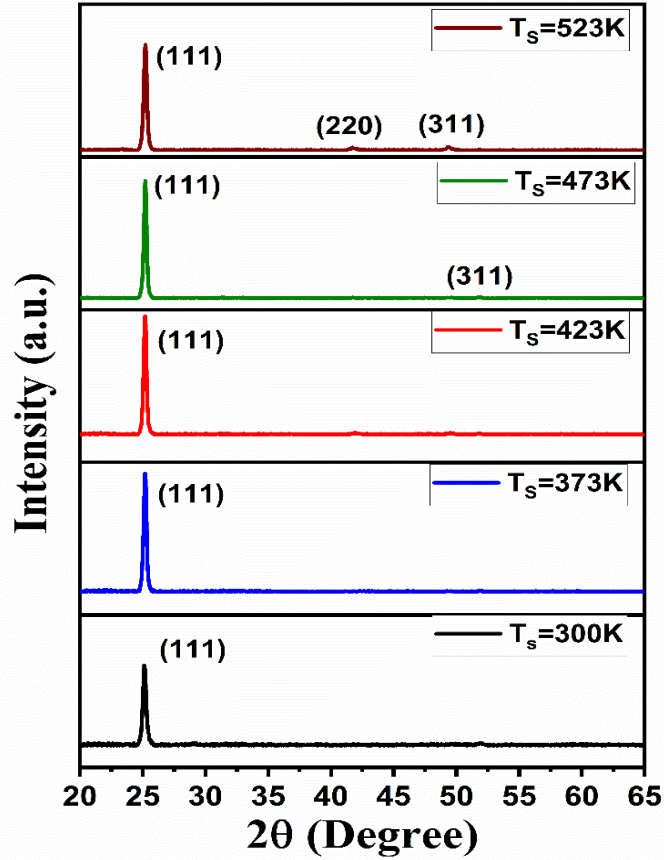


Figure 3.1: XRD pattern of CdTe thin films deposited at different substrate temperatures

The details of the obtained XRD parameters for the deposited samples are mentioned in Table-1. It is observed from Table-1 that the lattice parameters of the CdTe thin films deposited at different T_s are increased with an increase in substrate temperature. It is due to the rise of internal stress in film grains that set off the expansion of the lattice. The average grain size in the pristine CdTe thin films deposited at different substrate temperatures has been measured and reported in Table-1. Note that crystallite size increases with the substrate temperature in the samples due to the more extensive mobility of the atoms at a high temperature which reduces the density of the nucleation centers; under these circumstances, a smaller number of centers start to grow. The texture coefficient (TC) was estimated from the significant peak related to the (111)

plane for the deposited thin films. The estimated value is more than one for all the films, indicating the grain's abundance in that direction.

Table 3.1: Structural parameters of CdTe thin films at the different substrate temperatures

Substrate temperature (in K)					
	300	373	423	473	523
2θ (in degree)	23.74	23.73	23.72	23.67	23.62
d (in Å)	3.74	3.74	3.74	3.75	3.77
a (in Å)	6.48	6.48	6.49	6.50	6.54
D (in nm)	21.69	28.55	29.76	30.61	39.25
TC	1.45	1.52	1.69	1.72	1.85
Average grain size (in Å)	221	245	292	327	352

3.3.1.2 Morphological properties:

The surface morphology of all the deposited thin films was studied through FE-SEM. All the deposited samples are crack and pin-hole free, as depicted in Figure 3.2 (a) - (e). The average grain size of the samples increases with an increase in substrate temperature, as mentioned in Table 3.1. All the deposited samples show granular morphology. The substrate temperature promotes grain growth so that the tiny grains combine and realign themselves to reduce the grain boundaries, as depicted in Figures 3.2 (d) and (e). The elemental mapping of Cd and Te for the sample deposited at room temperature is illustrated in Figures 3.3 (a) and (b), confirming the elements' uniform distribution throughout the deposition area. The EDAX spectra of Cd and Te for the sample deposited at different substrate temperature is depicted in Figure 3.4 (a)-(e). Furthermore, the atomic percentage of the deposited samples was studied and tabulated in Table 3.2. Note that the sample deposited at room temperature is Tellurium rich (Chapman et al. 2002), whereas the sample deposited at the higher T_s is Cadmium rich.

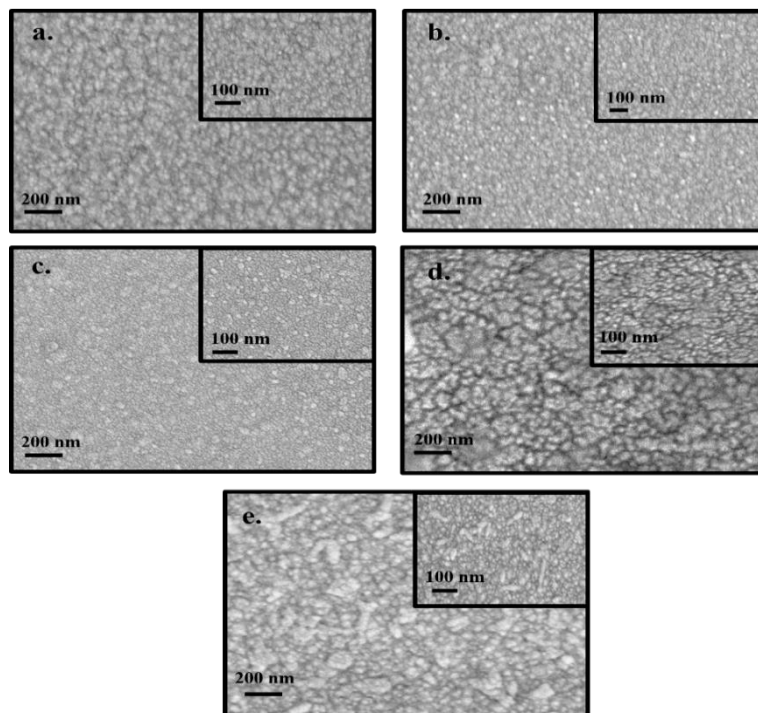


Figure 3.2 SEM micrograph of CdTe thin films deposited at a substrate temperature of a. 300 K b. 373 K c. 423 K d. 473 K e. 523 K

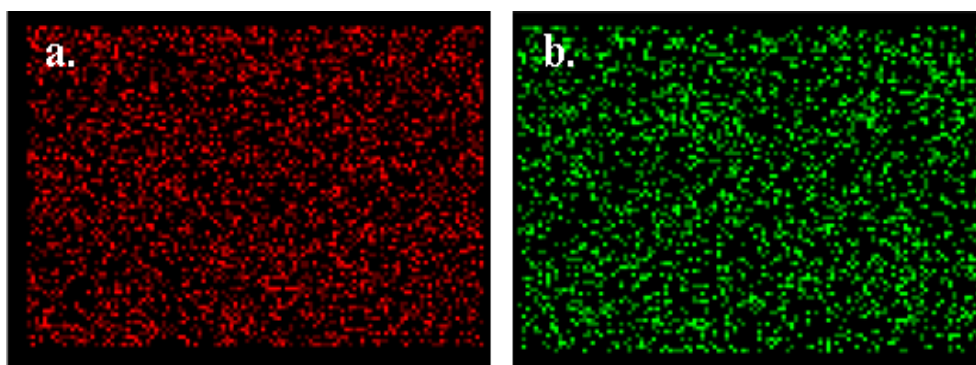


Figure 3.3 Elemental mapping of a. Cd b. Te for the sample deposited at room temperature.

Table 3.2 : Composition of CdTe samples at elevated substrate temperature

Substrate temperature	Cd	Te
300K	48.73	51.27
373K	48.21	51.79
423K	49.87	50.13
473K	49.09	50.91
523K	50.98	49.02

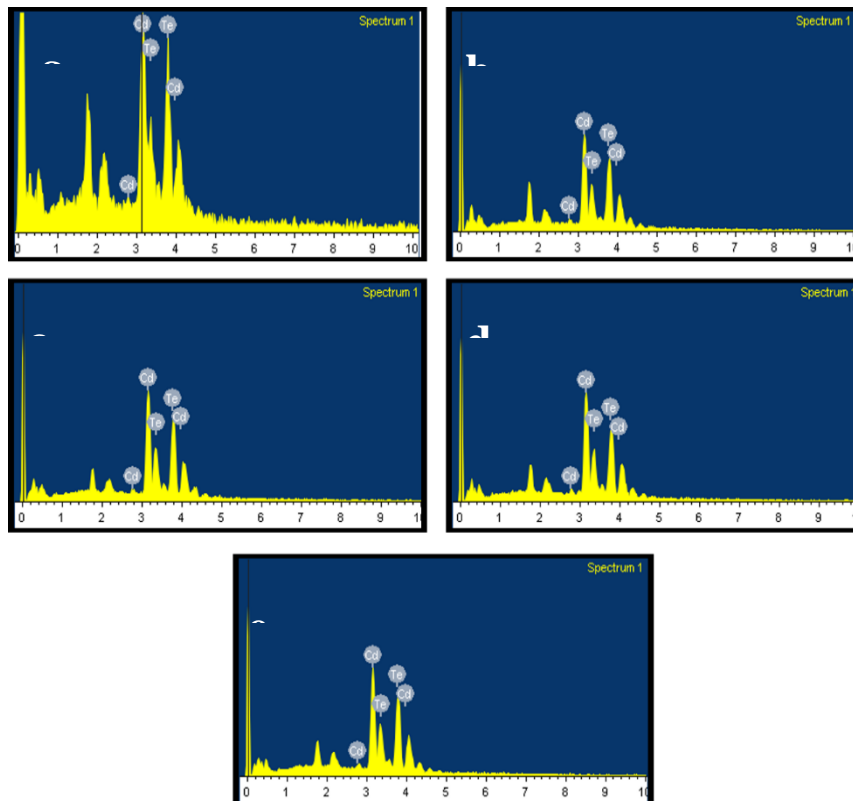


Figure 3.4 EDAX spectra of CdTe thin films deposited at substrate temperature of a. 300 K b. 373 K c. 423 K d. 473 K e. 523 K

3.3.1.3 Optical properties:

The optical absorbance spectra of CdTe thin films were studied using UV-Vis-NIR spectroscopy in the 300-1100 nm wavelength range, as shown in Figure 3.5. The optical absorbance increases with increased substrate temperature, possibly due to the increase in crystallite size. Furthermore, the optical band gaps of the deposited thin films were calculated by plotting the $(\alpha h\nu)^2$ versus $h\nu$. Figure 3.6 displays the band gap of the deposited samples, which can be determined by extrapolating the linear portion of the curve to the x-axis at the point where $(\alpha h\nu)^2$ equals zero. The transition was considered to be direct and allowed. The band gap of the CdTe thin films deposited at the substrate temperature of 300 K was found to be 1.5 eV which matches the literature finding (Nikale et al. 2011). The optical band gaps of the deposited films decreased with the increase in temperature, as charted in Table 3.3.

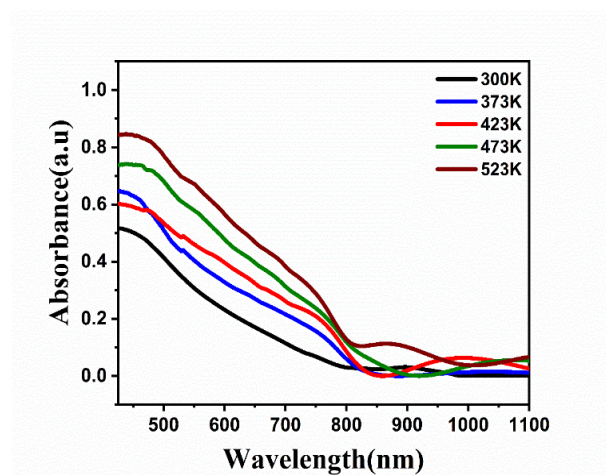


Figure 3.5 Absorbance spectra of CdTe thin films at different substrate temperature.

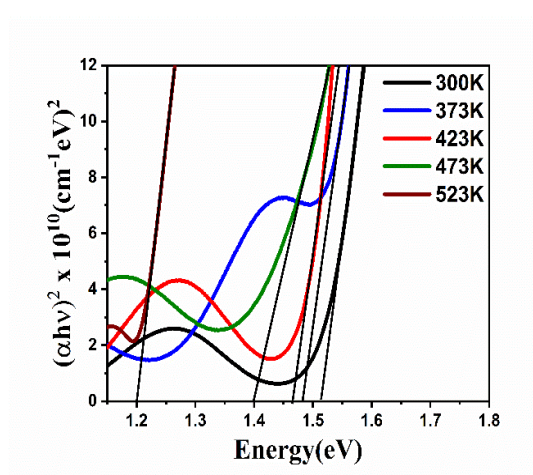


Figure 3.6 Band gap of CdTe thin films at different substrate temperature.

3.3.1.4 Electrical properties:

At the final stage of our experimental study, the electrical characterization of the deposited films was studied. The type of conductivity was determined by using the conventional hot probe method. The conductivity varies from p-type to n-type with the increment of the substrate temperature since CdTe thin films deposited at substrate temperatures 300 K, 373 K, and 423 K were Tellurium rich. In contrast, the film deposited at $T_s = 523$ K is found to be cadmium rich. It was confirmed from the EDAX

analysis (Shreekanthan et al. 2006a). The I-V characteristics of the deposited samples are depicted in Fig.7. The conductivity of the films was increased with the higher substrate temperature. It may be due to the improvement of crystallinity and change in carrier concentration in the sample. Note that the current (I) changes linearly with respect to the applied biasing voltage (V), which confirms the ohmic nature of the contacts, as shown in Figure 3.7.

Table-3.3: Change in the energy band gap of the deposited CdTe thin films:

Substrate temperature	CdTe (in eV)
300K	1.51
373K	1.48
423K	1.46
473K	1.39
523K	1.20

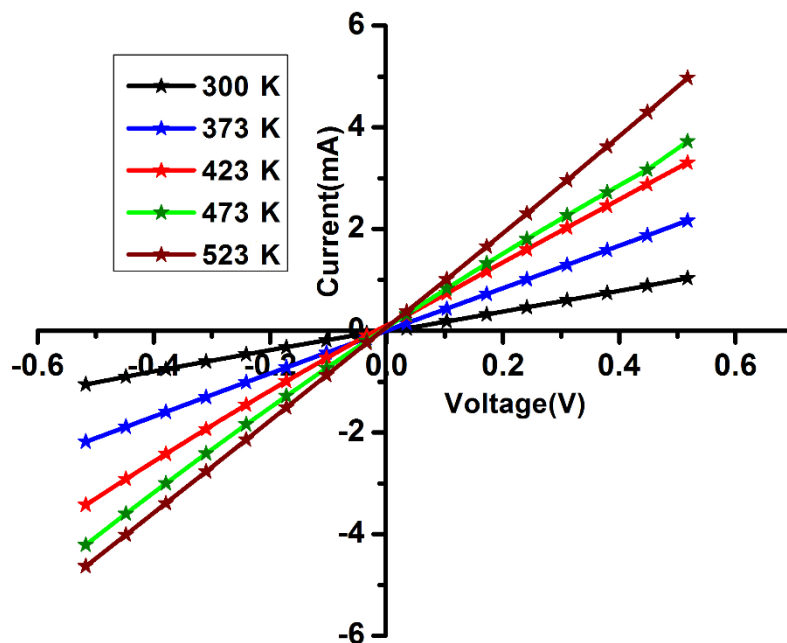


Fig 3.7: The variation of current with respect to the applied voltage for the CdTe thin films deposited at different substrate temperature.

3.3.2 Theoretical results:

3.3.2.1 Structural properties:

To begin with, the optimum bulk geometry of CdTe systems was obtained. Then the (110) surface slabs were constructed from the optimized bulk geometry and stacked along the normal direction. A sufficient vacuum of 10 Å thickness along the normal direction inside the unit cell has been considered during the slab and surface calculations. The optimized geometry of the CdTe (110) is depicted in Figure 3.8. This II-VI semiconductor exhibits a cubic structure with a lattice constant of 6.48 Å, matching our experimental results. The intralayer spacing of CdTe (110) was found to be 2.80 Å.

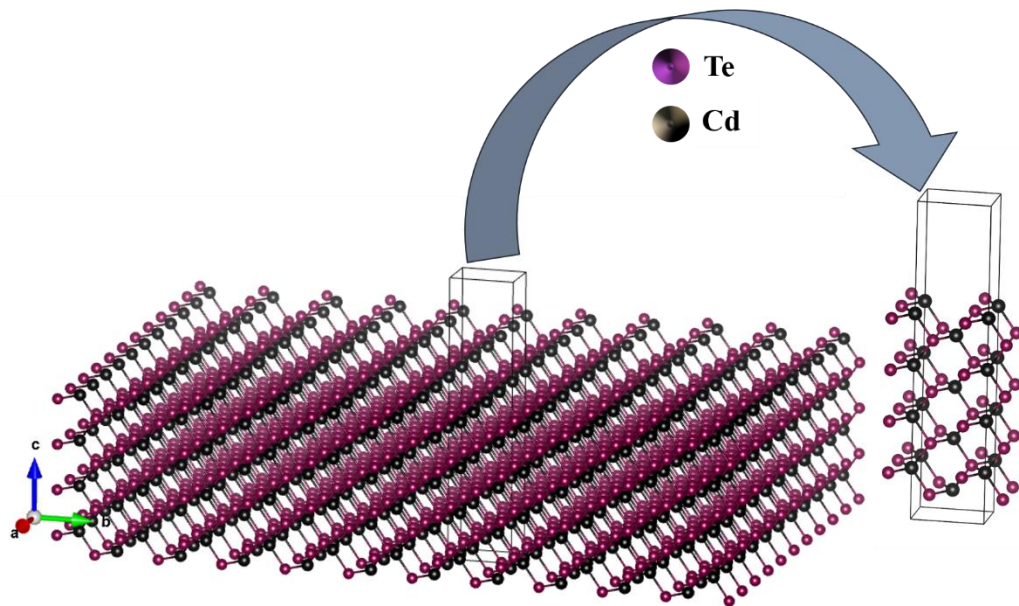


Figure 3.8: Optimized geometry of the CdTe (110), right side image shows the unit cell.

3.3.2.2 Electronic properties:

CdTe in the bulk form possesses a direct bandgap of 1.50 eV which agrees well with the experimental findings. (Pochareddy et al. 2021) The calculated band structure of the CdTe (110) is shown in Figure 3.9. Interestingly CdTe (110) also showed a direct bandgap of 1.60 eV at the Γ -point. To understand the band edge character, the atom

projected DOS for CdTe (110) was plotted and shown in Figure 3.10. The VBM comprises Te 5p and Cd 3d orbitals, whereas the CBM consists of Te 5p and orbitals.

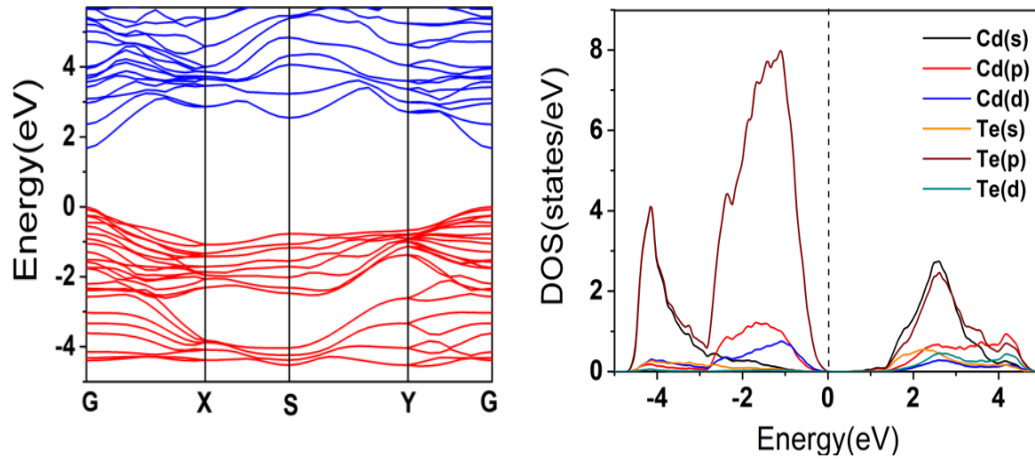


Figure 3.9 and 3.10: Band structure and DOS of CdTe (110)

3.3.2.3 Work function and band edge position:

The band edge position was calculated to understand the application of CdTe thin films in the PV cells. For this purpose, we first estimated the surface work function from the calculated average electrostatic potentials. Note that the work function is the minimum energy required to transfer an electron from the Fermi energy to the vacuum level. Therefore it can be calculated by using the equation 2.25. The vacuum level was determined by considering sufficient space in the unit cell. The work function for CdTe (110) was 4.71 eV, as shown in Figure 3.11. A proper energetic position of the band edges of the photovoltaic materials may significantly enhance the efficiency of the solar cells. The electronegativity was 4.96 eV for CdTe (110) by employing the Mulliken electronegativity formula. From the equation (2.26) and (2.27), the E_{VB} , and E_{CB} for CdTe(110), were found to be 1.26 eV and -0.34eV, respectively.

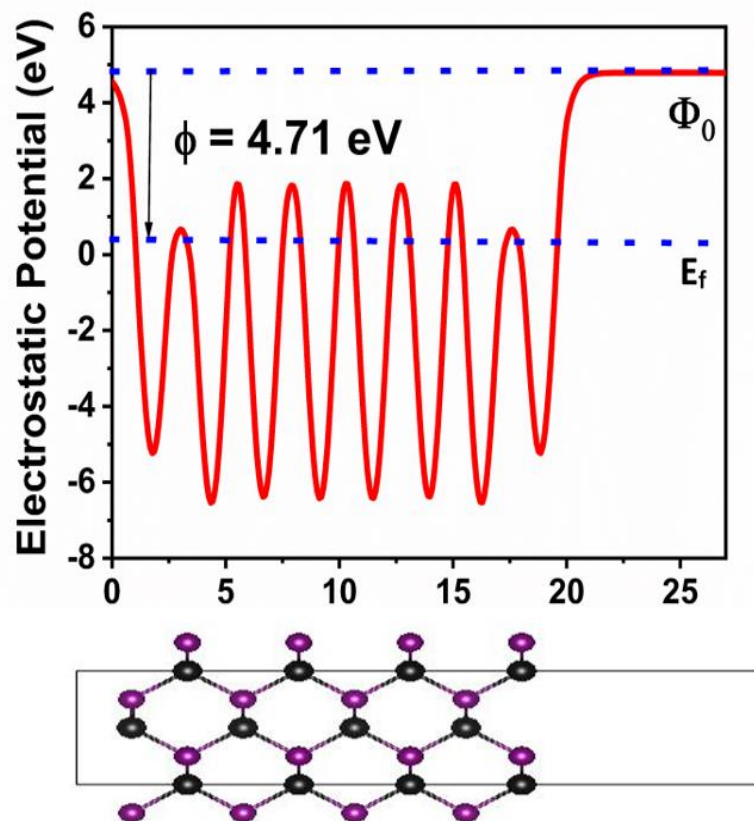


Figure 3.11: Average electrostatic potential of CdTe(110)

3.4 Summary:

In conclusion, the CdTe thin films were prepared in an ambient condition and thoroughly characterized using different characterization techniques. The absorption was found to be increased with an increase in substrate temperature. The conductivity was changed from p-type to n-type at higher substrate temperature, which may be helpful for solar cell applications.

CHAPTER 4

PREPARATION AND PROPERTIES OF ZnTe THIN FILMS DEPOSITED AT DIFFERENT SUBSTRATE TEMPERATURES

Overview:

This chapter explores the ideal conditions for depositing p-ZnTe thin films. Through an optimization process, it has been found that obtaining the desired stoichiometry condition is greatly dependent on the temperature of the substrate. Consequently, with varying substrate temperatures, an extensive analysis of the structural, morphological, elemental, optical, and electrical properties of the ZnTe thin films have been done.

4.1 Introduction:

In addition to CdTe, Zinc Telluride (ZnTe) is another important II-VI binary semiconducting material that has numerous applications in optoelectronic devices such as photodetectors (Cao et al. 2011), LEDs (Tanaka et al. 2003), solar cells (Wolden et al. 2016), etc., owing to the high absorption coefficient of 10^4 cm^{-1} (Islam et al. 2017) and direct wide band gap of 2.26 eV (Islam et al. 2017)(Acharya et al. 2007) (Ibrahim et al. 2004). Additionally, due to its high electro-optic coefficient, ZnTe is useful in generating and detecting terahertz (THz) radiation (Guo et al. 2007). ZnTe generally possesses p-type electrical conductivity. However, it is not easy to deposit the n-ZnTe due to the self-compensation effect. Several extrinsic doping methods are adopted to deposit the n-type ZnTe thin films. Due to its p-type electrical conductivity, it is regarded as the promising back contact material for the CdTe solar cells. Recently, the Cd alloyed ZnTe layer has been used as the absorber layer in tandem solar cells. (Sharma et al. 2023) Several methods have been used to deposit the thin films, such as electrodeposition (Bozzini et al. 2000) (Bouroushian et al. 2009)(Fauzi et al. 2013); closed space sublimation, (Park et al. 2011), molecular beam epitaxy (Wang et al. 2009) hydrothermal, (Wang et al. 2011) sputtering, (Gessert et al. 2013) metallo – organic chemical vapor deposition (MOCVD),(Shtrikman et al. 1988) and thermal evaporation or vacuum deposition. (Bacaksiz et al. 2009) Among all these methods, the thermal evaporation technique is used to deposit the thin films, which is a cost-effective and efficient method to obtain excellent quality thin films. The properties of the samples depend on the deposition parameters such as substrate temperature, annealing temperature, deposition rate, and source-to-substrate distance. The substrate temperature plays a key role as it provides a wide variety of possibilities and affects the composition and crystallinity of the deposited films.

Various research groups have shown the characteristics of ZnTe thin films at different substrate temperatures. (Rao et al. 2009)(Amutha et al. 2006)(Seyam 2012) However, there has not been any comprehensive experimental and theoretical analysis of the ZnTe layer and its uses in solar cells. This chapter delves into the structural, morphological, elemental, optical, and electrical properties of the ZnTe thin films deposited at different

substrate temperatures. Additionally, the electronic properties and band edge position of the sample are thoroughly examined using DFT.

4.2 Methodology:

4.2.1 Experimental methodology:

The thermal evaporation technique was used to deposit the ZnTe thin films on a glass substrate at different substrate temperatures. The pressure was maintained at less than 5×10^{-6} Torr during the synthesis process using a diffusion pump backed by a rotary pump. ZnTe powder (Alfa Aesar), purity of 99.9999%, was used to deposit the thin films. The glass substrate was meticulously cleaned before depositing, and subsequently, it was air annealed at a temperature of 200⁰C for 5 hours. A tantalum boat was used as a source. The films were deposited at different T_s to get the stoichiometry films. The deposition rate was maintained at nearly 46 nm/min. ZnTe powder was evaporated from a boat by applying a constant current. The thickness of the film was measured by the gravimetric method, and it was maintained at nearly 420nm. The structural properties of the films were demonstrated by the Rigaku Miniflex600 X-Ray diffractometer ($\lambda_{\text{CuK}\alpha} = 1.5402\text{\AA}$). The deposited films' surface morphology and elemental composition were studied using the Ultra 55 scanning electron microscopes. Absorption spectra of the deposited films were obtained by the Shimadzu MPC3600 UV-VIS-NIR spectrometer in the wavelength range of 300 nm-900 nm. The samples' electrical properties were studied using the Keithley 2400 source meter. The conductivity of the sample was measured by using the hot probe method.

4.2.3 Theoretical methodology:

To gain a deeper understanding of the electronic structure of ZnTe, Density Functional Theory (DFT) calculations were employed. The Vienna ab-initio simulation package (VASP) using the projected augmented wave (PAW) method was utilized, along with Generalized Gradient Approximation (GGA) and Perdew-Burke-Ernzerh (PBE) parameterization scheme to estimate the exchange and correlation potential. To

incorporate Van Der Waal's (vdW) interactions, the density functional DFT-D3 method was applied. A high wave function cutoff of 500 eV and force convergence criteria of 0.01 eV/Å were used to obtain accurate results. The optimum bulk geometry of the ZnTe system was obtained before constructing (110) surface slabs and stacking them along the normal direction. A vacuum thickness of 10Å was used during slab and surface calculations to avoid interaction between periodic images. Finally, the hybrid-DFT calculation with Heyd-Scuseria-Ernzerhof (HSE06) hybrid functional with 25% Hartree-Fock exchange energy contribution was utilized to estimate the proper bandgap and band edge position.

4.3 Results and Discussions:

4.3.1 Experimental results:

4.3.1.1 Structural properties:

The XRD pattern of ZnTe thin films deposited at the elevated substrate temperatures was studied, and it was found that the predominant peak at a 2θ value of 25.19° corresponds to the reflection from the (111) plane. This outcome matches with the JCPDS (150746). (Isik et al. 2020) Note that two additional peaks corresponding to (220) and (311) planes found at 2θ values of 42.66 and 49.36 , respectively, were observed at higher substrate temperatures, as depicted in Figure 4.1. All the deposited samples were polycrystalline. It was confirmed that ZnTe thin films possess a cubic crystal structure.

Table-4.1 contains the XRD parameters for the deposited samples, including their lattice parameters. It is worth noting that as the substrate temperature increases, the lattice parameters of the ZnTe thin films also increase. This is due to the internal stress in the film grains, which causes the lattice to expand. The average grain size of the pristine ZnTe thin films has also been measured and reported in Table-4.1. The crystallite size increases with substrate temperature as the atoms have greater mobility at higher temperatures, resulting in a reduced density of nucleation centers, and ultimately, fewer centers start to grow. The texture coefficient (TC) for the deposited thin films was estimated from the significant peak related to the (111) plane and is reported in Table-4.1. All films have a TC value greater than one, indicating an abundance of grains in that direction.

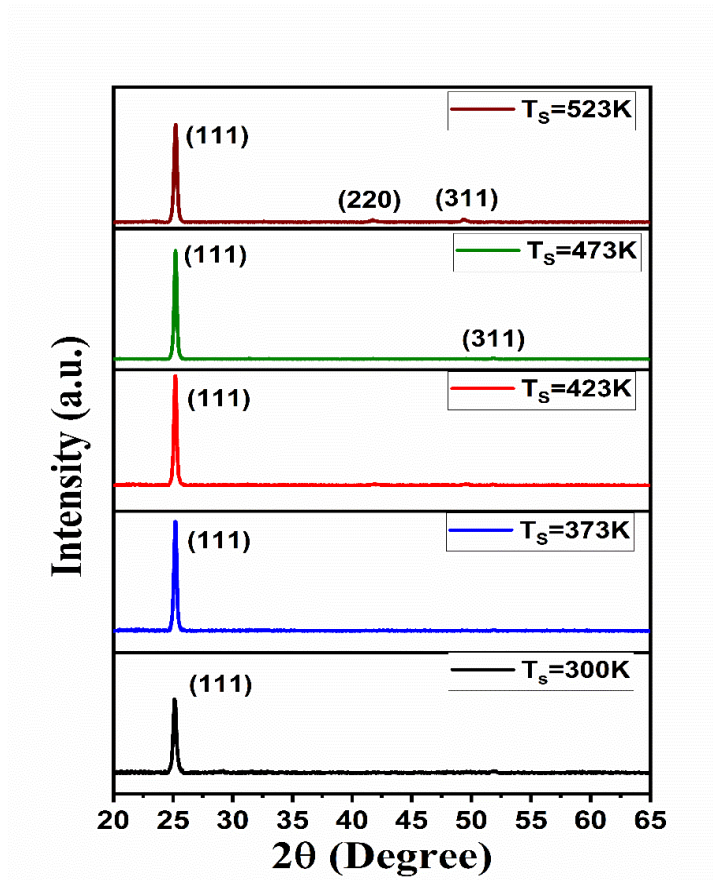


Fig 4.1: XRD pattern of ZnTe thin films deposited at different substrate temperatures.

Table 4.1: Structural parameters of ZnTe thin films at the different substrate temperatures

	Substrate temperature (in K)				
	300	373	423	473	523
2 θ (in degree)	25.19	25.20	25.19	25.18	25.14
d (in Å)	3.53	3.53	3.53	3.53	3.53
a (in Å)	6.11	6.11	6.11	6.11	6.11
D (in nm)	25.30	25.37	28.53	29.01	34.28
TC	1.21	1.30	1.42	1.50	1.67
Average grain size (in Å)	410	460	487	520	577

4.3.1.2 Morphological and elemental studies:

The FE-SEM was used to examine the surface morphology of all the deposited films. As shown in Figure 4.2 (a) - (e), all the samples were free from cracks and pinholes.

Table 4.1 reveals that an increase in substrate temperature results in an increase in average grain size. Granular morphology was observed in all deposited samples, and an increase in substrate temperature promoted grain growth, as can be seen in Figures 4.2 (d) and (e), where tiny grains combined, realigned themselves, and reduced grain boundaries. Figures 4.3 (a) and (b) illustrate the uniform distribution of Zn and Te elements throughout the deposition area of the sample deposited at room temperature. Figure 4.4 (a)-(e) shows the EDAX spectra of Zn and Te for the sample deposited at different substrate temperatures.

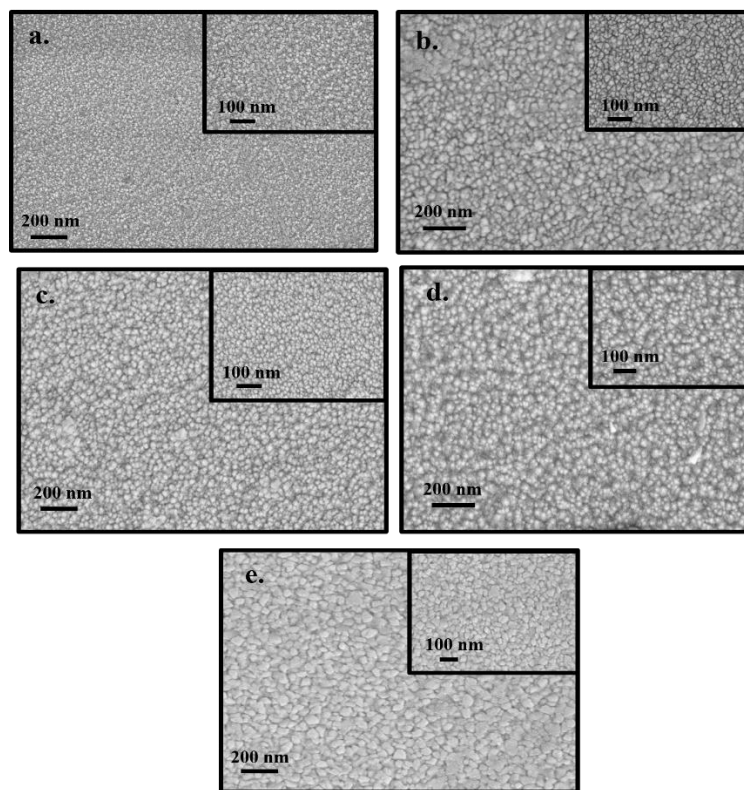


Figure 4.2 SEM micrograph of ZnTe thin films deposited at the substrate temperature of a. 300 K b. 373 K c. 423 K d. 473 K e. 523 K

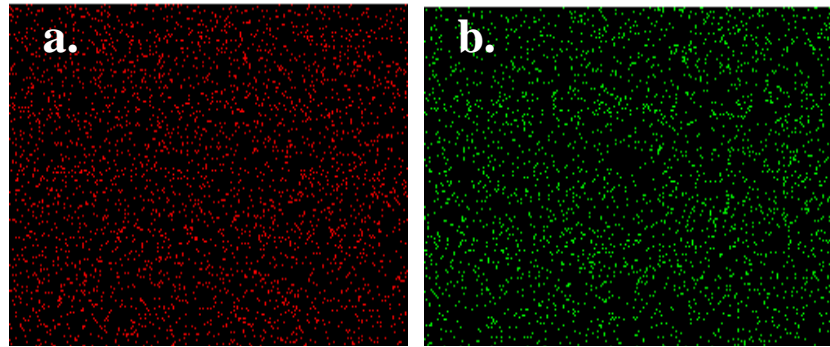


Figure 4.3 Elemental mapping of a. Zn b. Te for the sample deposited at 300K

Table 4.2: Elemental composition of ZnTe thin films at different substrate temperatures

Substrate temperature	Zn	Te
300K	45.63	54.37
373K	46.95	53.05
423K	47.23	52.17
473K	48.14	51.86
523K	49.01	50.99

Zinc and tellurium have different vapor pressures, causing a non-stoichiometric vapor. Film composition depends on the number of atoms/molecules settling on the substrate and the sticking coefficient. (Maissel et al. 1971) The films deposited at lower substrate temperature resulted in excess tellurium. When the substrate temperature increases, it causes tellurium to evaporate and increases the sticking coefficient of zinc. This results in a stoichiometric condition for ZnTe thin films, as depicted in Table 4.2.

4.3.1.3 Optical properties:

For ZnTe thin films, the absorbance was studied within the wavelength ranging from 300 to 900 nm. The absorbance was found to be decreased with an increase in substrate temperature, as depicted in Figure 4.5. The graphs of $(\alpha hv)^2$ vs. hv (seen in Figure 4.6) display a linear section that indicates Eqn. (2.6) holds for ZnTe films if $n = 1/2$. This implies that ZnTe films undergo direct allowed optical transitions. The linear portions of the graphs were extended to determine the optical bandgap (also seen in Figure 4.6). The optical bandgap was reduced with an increase in substrate temperature. The optical bandgap shift is due to the enhanced crystallinity and stoichiometry of the films deposited at high substrate temperatures. The optical band gap of ZnTe thin films deposited at room temperature was 2.24 eV, which matches the experimental findings. (Maki and Hassun 2016)

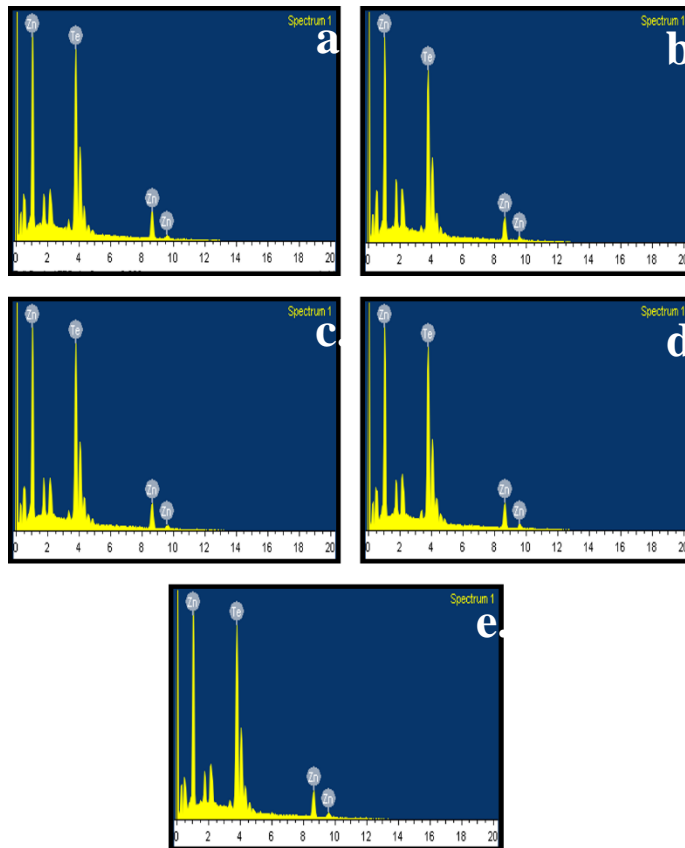


Figure 4.4 EDAX spectra of ZnTe thin films deposited at a substrate temperature of a. 300 K b. 373 K c. 423 K d. 473 K e. 523 K

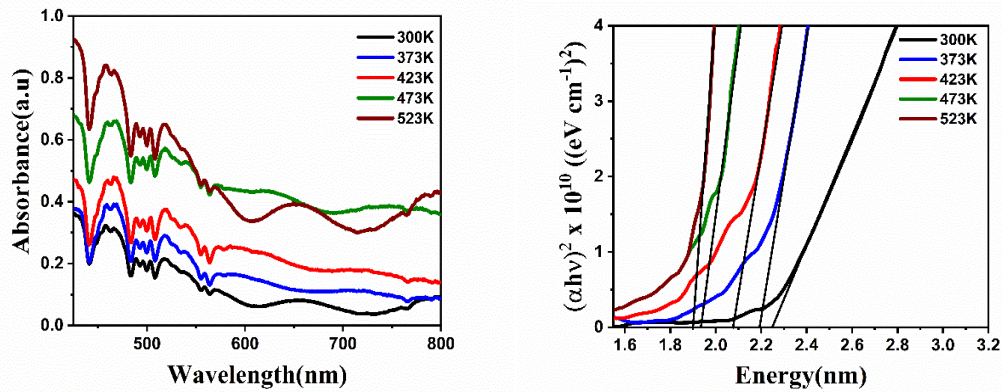


Fig 4.5 & 4.6: Absorbance spectra and band gap of ZnTe thin films deposited at different substrate temperatures.

Table 4.3: Change in the energy band gap of the deposited ZnTe thin films:

Substrate temperature	ZnTe (in eV)
300K	2.24
373K	2.18
423K	2.07
473K	1.93
523K	1.89

4.3.1.4 Electrical properties:

The majority carrier type of ZnTe films deposited at varying substrate temperatures was determined using the conventional hot probe technique, and it was discovered that all films were of p-type. Even when deposited at higher substrate temperatures, which are nearly stoichiometric, the films were still found to be p-type, possibly due to the observed self-compensation effect in ZnTe and other II-VI compound semiconductor films. (Desnica 1998) The excess of tellurium in films deposited at lower substrate temperatures was responsible for their p-type nature. The I-V plots depicted ohmic conduction, as shown in Figure 4.7. It was observed that the electrical resistivity of the films reduced as the substrate temperature increased. The films deposited at higher substrate temperatures have improved crystallinity and stoichiometry, decreasing resistivity. On the other hand, films deposited at lower substrate temperatures have

small grain sizes and a large grain boundary region that is highly disordered, resulting in a significant number of defect states known as trap states. These trap states act as effective carrier traps that hinder the flow of majority charge carriers between the grains. However, films deposited at higher temperatures are nearly stoichiometric and have larger grains, reducing the number of defect states and increasing the conductivity of the films.

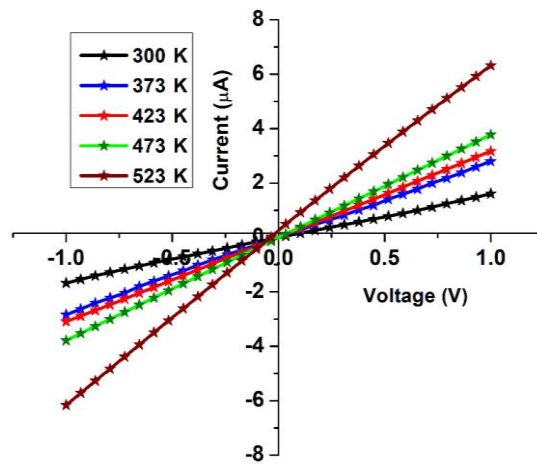


Fig 4.7: I Vs V characteristics of the ZnTe thin films deposited at different substrate temperatures

4.3.2 Theoretical results:

4.3.2.1 Structural properties:

Firstly, the optimum bulk geometry for ZnTe systems was obtained. From this optimized bulk geometry, (110) surface slabs were constructed and arranged along the normal direction. A vacuum thickness of 10 \AA was implemented within the unit cell along the normal direction to ensure accurate slab and surface calculations. Figure 4.8 displays the optimized geometry for ZnTe (110). This II-VI semiconductor exhibits a cubic structure with a lattice constant of 6.10 \AA , matching our experimental results. The intralayer spacing of ZnTe(110) was found to be 2.59 \AA .

4.3.2.2 Electronic properties:

ZnTe in the bulk form possesses a direct bandgap of 2.39 eV which agrees well with the experimental findings. (Mahmood et al. 2020) The calculated band structure of the ZnTe(110) is shown in Figure 4.9. Interestingly ZnTe(110) also showed a direct bandgap of 2.47 eV at the Γ -point. To understand the atom-projected DOS for ZnTe(110) was plotted and shown in Figure 4.10 to understand the band edge character. 4s, 3d orbitals of Zn and 5s, 5p orbitals of Te are dominated in the valence band maximum (VBM) of ZnTe, whereas the conduction band minimum is made-up of Zn 4s and Te-5p orbitals.

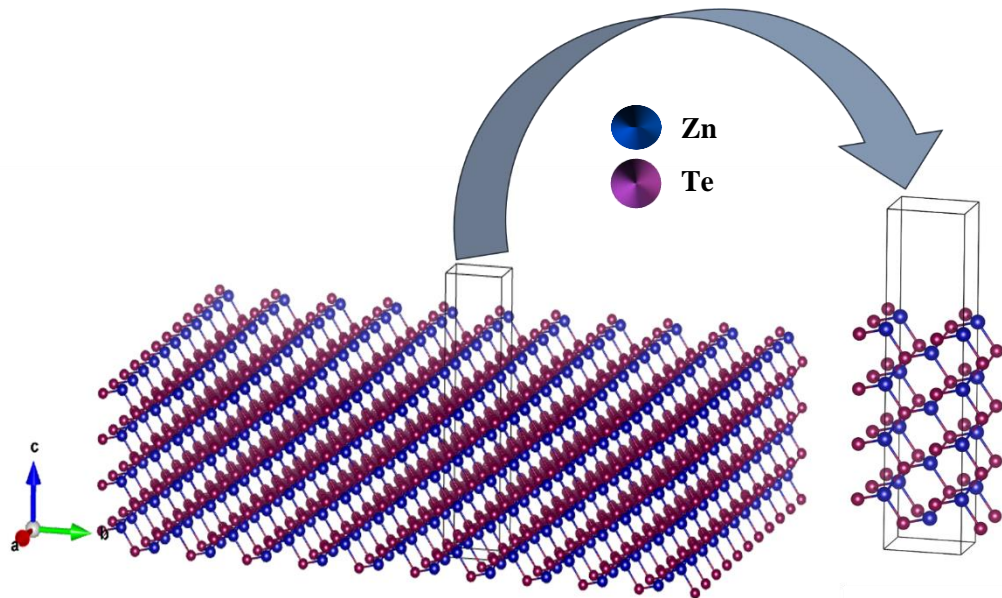


Fig 4.8: Optimized geometry of ZnTe(110)

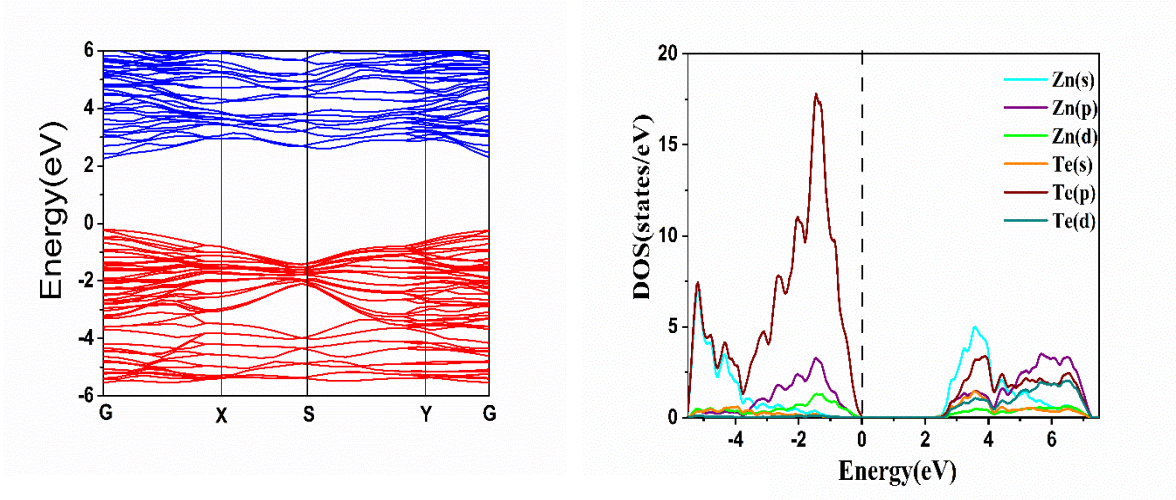


Fig 4.9 & 4.10: Electronic structure of ZnTe(110)

4.3.2.3 Work function and band edge position:

The band edge position was calculated to explore the suitability of ZnTe thin films for use in PV cells. The first step was to estimate the surface work function by analyzing the average electrostatic potentials. The work function was calculated using equation 2.25 and was found to be 4.81 eV, as shown in Figure 4.11.

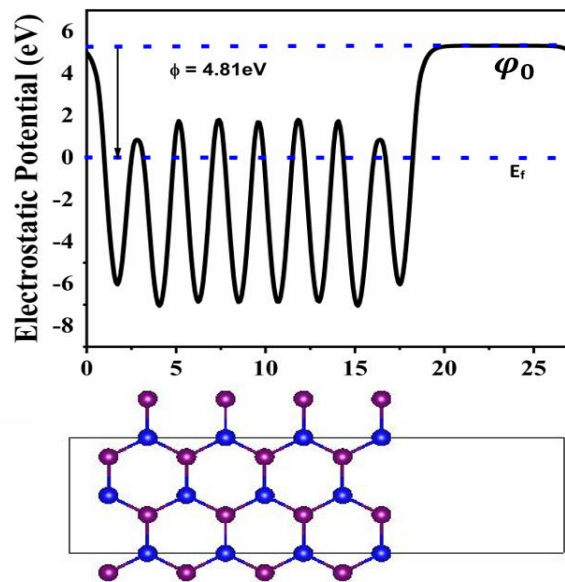


Fig 4.11: Average electrostatic potential of ZnTe (110)

Proper placement of the band edges in photovoltaic materials can significantly enhance the efficiency of solar cells. ' χ ' was found to be 5.02 eV from the Mulliken electronegativity formula. By using equations (2.26) and (2.27), the E_{VB} and E_{CB} for ZnTe(110) were found to be at 1.76 eV and -0.71 eV in the normal hydrogen electrode(NHE) scale.

4.4 Summary:

To sum up, the ZnTe thin films were prepared and characterized under ambient conditions. It was observed that the absorbance of the films increased as the substrate temperature rose. The ZnTe thin film also exhibited a broad band gap of 2.24 eV. Moreover, its conductivity was consistently p-type, regardless of the substrate temperature, making it suitable as a p-type layer for solar cells.

CHAPTER 5

***p*-ZnTe/*n*-CdTe HETEROSTRUCTURE PREPARATION AND PROPERTIES (ZnTe AS A BACK SURFACE FIELD LAYER (BSF) IN CdTe SOLAR CELLS)**

Overview:

*This chapter describes the preparation and properties of *p*-ZnTe/*n*-CdTe heterostructure. The ambient condition to obtain the *p*-ZnTe and *n*-CdTe was discussed in previous chapters. Based on that, the heterointerface was obtained. The theoretical properties and the band bending at the interface for this heterostructure were realized by using the DFT. The calculation confirmed that the wide band gap and high work function materials such as ZnTe could be used as the back surface field layer to minimize the recombination losses at the back surface of the CdTe thin film solar cell.*

5.1 Introduction:

In the previous chapters (Chapter 3 and Chapter 4), the properties of two essential binary semiconductors were discussed by varying the substrate temperatures. Some specific properties of both the semiconductors, such as high stability in the thin film form (Mrinalini et al. 2019), and the direct bandgap nature of these compounds, make them very suitable for photovoltaic solar cell applications. (Britt and Ferekides 1993a) However, a higher charge separation yield in the compounds is one of the main requirements for their effective use in photovoltaic applications, which is expected to improve cell efficiency.

So far, CdTe-based solar cells have attained a greater power conversion efficiency of 22.1%. (Poplawsky et al. 2016)(Green et al. 2021b) In this regard, type-II semiconductor heterojunction made of these semiconductors would be convenient as the photo-generated charge carriers can be spatially separated into the different parts of these systems. The major challenge in CdTe-based solar cells is to create good back contact. Enhancement of the energy conversion efficiency of the solar cell requires a connection with low electrical contact resistance, which is challenging to make in the case of CdTe thin films. Recently, two groups, Amin et al. and Gessert et al., have reported that the deposition of an extra ZnTe layer with high carrier concentration could fix the drawback mentioned earlier of CdTe solar cells. (Amin et al. 2007a; Gessert et al. 2009a)(Patra and Pradhan 2012) Note that CdTe is a highly resistive material. The buffer layer material should have high electrical conductivity and electron affinity to design a Schottky junction with this compound. The ZnTe in its p-type variant could be ideal. (Mitchell et al. 1988) Also, ZnTe has a direct bandgap of 2.2 eV, (Jiao et al. 2015), which is higher than CdTe. Therefore, it could make a type-II heterojunction with CdTe. In addition, both CdTe and ZnTe have a cubic crystal structure with a very similar lattice parameter. Hence the interface roughness is expected to be significantly less, resulting in a negligible scattering at the interface. It has been experimentally reported that the valence band offset of the ZnTe/CdTe heterointerface is very low (Späth et al. 2007), which is suitable for hole transport to metal contacts. Also, ZnTe acts as an electron reflector(Suthar et al. 2021b)(Sites and Pan 2007), which could lead to a minimal recombination rate at the interface. (Oklobia et al. 2019)(Hall et al. 2021) In this work, the primary aim was to study the suitability of using the ZnTe/CdTe

interface in photovoltaic solar cells. Therefore, stoichiometric ZnTe and CdTe thin films and a clean interface in thin-film form have been synthesized using the vapor deposition technique. Detailed characterization of the synthesized films and their heterointerface has been done using various characterization techniques. The electronic structure and interface properties of the interface have been further investigated by using density functional theory calculation. Finally, the accurate band positions and their alignment has been obtained to understand photo-generated charge carrier dynamics in the system.

5.2 Methodology:

5.2.1 Experimental Methodology:

To start with, glass substrates were ultrasonically cleaned. A tantalum boat was used, where CdTe and ZnTe powders were kept to prepare the thin films. CdTe and ZnTe, films of 400 nm (deposition rate of ~ 46 nm/min), were prepared at elevated substrate temperatures. To prepare the ZnTe/CdTe hetero-interface, the CdTe thin films were deposited at 523K on top of a silver-coated (back contact material) glass substrate. Then ZnTe was deposited on top of CdTe at room temperature. Finally, another contact layer of Ag is deposited on top of the ZnTe layer. A schematic diagram of deposited different films for heterojunction is shown in Figure 5.1. The junction area was about 0.2 cm x 0.2 cm. The morphological, structural, and electrical characterizations were performed for the synthesized film.

5.2.2 Theoretical methodology:

To gain a deeper insight, the electronic structure of the ZnTe/CdTe heterointerface was investigated by employing Density functional theory (DFT) calculation. The project augmented wave (PAW) method implemented in Vienna ab initio simulation package (VASP) was used. Generalized gradient approximation (GGA) was used, considering Perdew- Burke- Ernzerh (PBE) parameterization scheme to estimate the exchange and correlation potential. The long-range Van der-Waal interaction plays an essential role in these interfaces. The Van Der Waal's (vdW) interaction was introduced in the system employing dispersion correction for the density functional DFT-D3 method. A high wave function cut-off of 500 eV was used in this calculation to obtain accurate results. From the optimum bulk geometry of CdTe and ZnTe systems, the (110) surface slabs

were constructed. For individual semiconductors, eight layers of (110) surface were further relaxed with a sufficient vacuum of 10 Å thickness along the normal direction inside the unit cell. The force convergence criteria were set to 0.01 eV/Å. In each case, a $7 \times 7 \times 1$ Monkhorst K-point sample was used for Brillouin zone integrations. Finally, the hybrid-DFT calculation was employed using Heyd-Scuseria-Ernzerhof (HSE 06) hybrid functional with 25% Hartree-Fock exchange energy contribution to estimate the proper bandgap and the band edge position for all the structures.

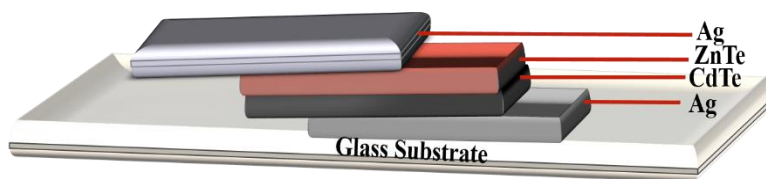


Figure 5.1: (Color online) Diagrammatic representation of deposited layers for the heterojunction

5.3 Results and Discussions:

5.3.1 Experimental results:

5.3.1.1. Structural properties:

In the case of the synthesized heterojunction thin films, both the predominant peaks from CdTe and ZnTe are present in the XRD pattern shown in Figure 5.2, which corroborates the formation of the hetero-interface.

Furthermore, in the case of ZnTe/CdTe heterostructure, the diffraction peaks slightly deviate towards the higher angle leading to a larger lattice which may be attributed to the larger ionic radius of Cd than that of Zn. (Ma et al. 2016)

5.3.1.2. Optical properties:

The absorbance was significantly improved in the ZnTe/CdTe heterojunction for low wavelength radiation, which was much higher than pristine CdTe and ZnTe, as shown in Figure 5.3. The optical bandgap of the heterojunction was estimated and compared with the pristine compound. The calculated band gap value of the heterojunction was 1.89 eV which lies in between the bandgap of ZnTe (2.24 eV) and CdTe (1.2 eV), as shown in Figure 5.4, confirming the absorption of visible light.

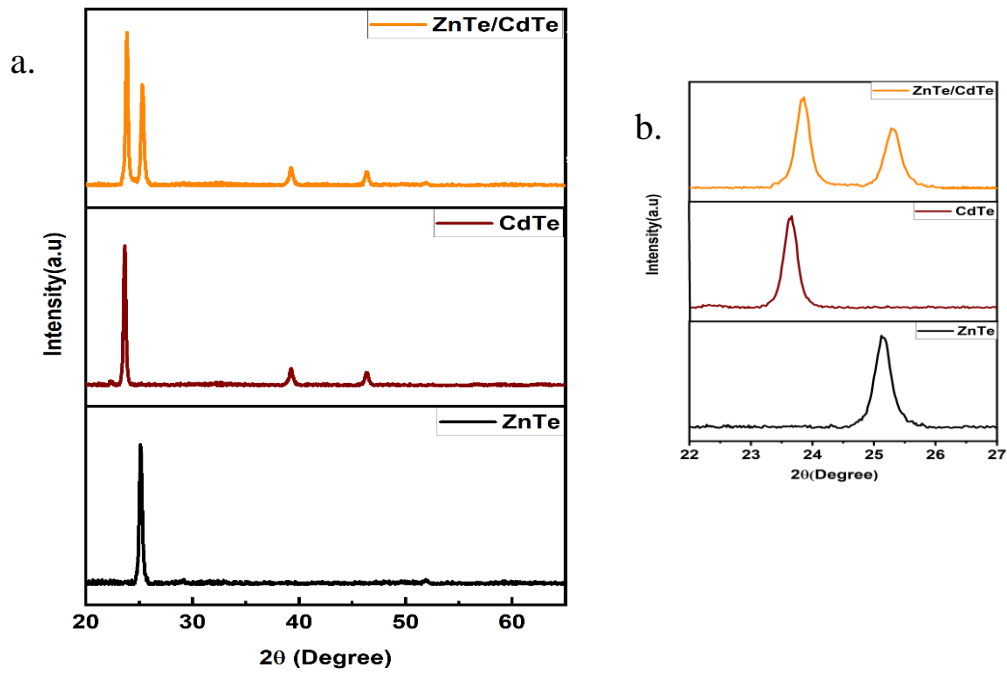


Figure 5.2: (Color online) The XRD pattern of ZnTe/CdTe deposited at the optimum condition within the 2θ ranging from a. $20^{\circ} - 65^{\circ}$ b. $22^{\circ} - 27^{\circ}$

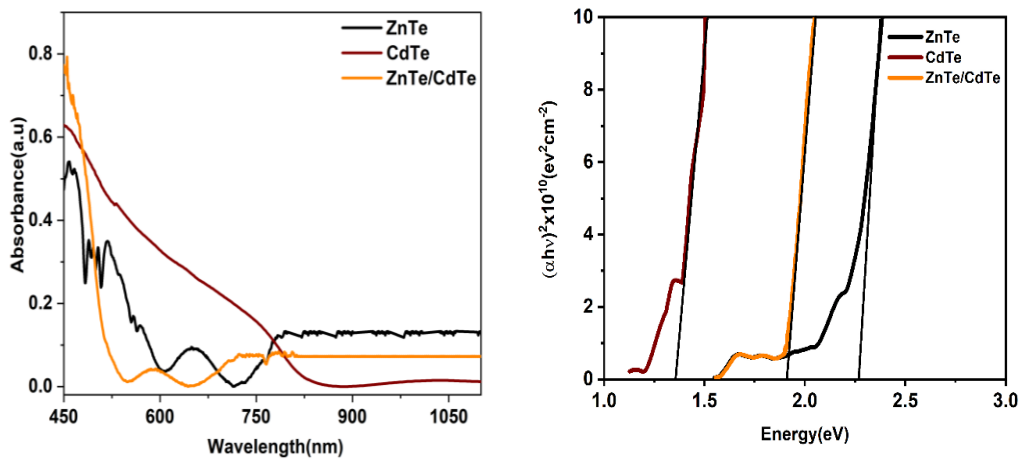


Figure 5.3 shows the absorption spectra, and Figure 5.4 depicts the band gap of ZnTe (black), CdTe (orange) thin films deposited in the optimized condition and ZnTe/CdTe hetero junction (brown)

The proposed hetero-junction works on the principle of segregating electrons and holes to opposite sides of the interface based on their unique lowest energy states. This spatial separation is achieved after the initial generation. Additionally, this configuration creates a "hidden" interface bandgap, which is smaller than either of the constituent semiconductors in the heterojunction. As a result, the energy required for electron/hole generation and recombination is reduced, allowing for an extended wavelength range that would otherwise not be possible. This has significant implications in optoelectronics applications. (Zheng et al. 2020)

When two semiconductors with differing band edge positions are brought together, their Fermi levels align at equilibrium, and their band edges shift after the band alignment. Charges migrate from one semiconductor to another due to the built-in electric field at the interface of the two semiconductors. This gives an idea of band bending or alignment at the junction. This band alignment will be discussed in the theoretical results section.

5.3.1.3 Electrical properties:

At the final stage of the experimental study, electrical characterization of the heterostructure was carried out. The I-V characteristics of the p-ZnTe/n-CdTe hetero-interface are shown in Figure 5.5, which indicates the rectifying behavior similar to a

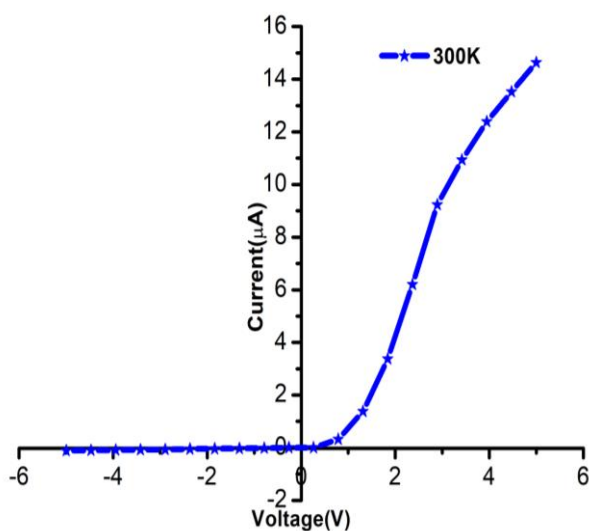


Figure 5.5: (Color online) I-V characteristics of p-ZnTe/n-CdTe heterojunction diode at room temperature.

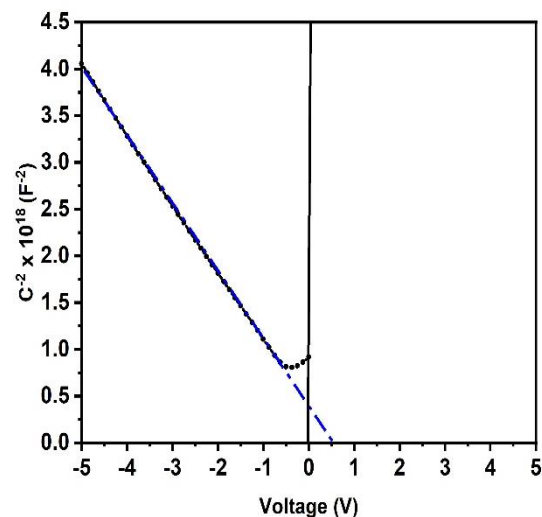


Figure 5.6: (Color online) the capacitance-voltage characteristic for p-ZnTe/n-CdTe heterojunction

typical p-n junction. To determine the barrier height of the interface ZnTe/CdTe, It is necessary to do the C-V characterization. Figure 5.6 depicts the voltage dependence of the heterojunction inverse square of the capacitance at the signal frequencies of 300 KHz. In an ideal abrupt junction, increasing depletion width with the voltage should decrease the capacitance with increasing reverse bias voltage and be frequency independent. In the case of ZnTe/CdTe, uniform carrier concentration exists, and the junction is abrupt. The junction capacitance can be expressed on a C^{-2} -V scale. Barrier height can be determined by the linear extrapolation of the $C^{-2}(V)$ function to $V=0$. In this interface, the barrier height was 0.55V, as shown in Fig.5.6.

5.3.2 Theoretical results:

5.3.2.1 Optimized structure parameters, Electronic structures:

In the case of the hetero-interface, the optimum interlayer spacing between ZnTe(110) and CdTe(110) is found to be 3.1Å which was higher than the intralayer spacing of ZnTe(110) and CdTe(110), i.e., 2.59 Å and 2.80 Å respectively. The optimized geometric structure of the hetero-junction is shown in Figure 5.7.

Interestingly CdTe(110) and ZnTe(110) and their heterointerface also showed direct bandgap nature. The band gap of 2.56 eV was found for CdTe(110)/ZnTe(110) heterojunction at the Γ -point, as shown in Figure 5.8. The atom-projected DOS was plotted for the hetero-structures to understand the band edge character, as shown in Figure 5.9. The VBM of the interface was made up of Te 5p, Zn 4s, Cd 4s, and Zn 3p orbitals, whereas CBM was dominated by Zn 4s, Te 5p, and Zn 3p orbitals. The interaction between s-Zn and p-Te states shows a significant hybridization at -5 eV.

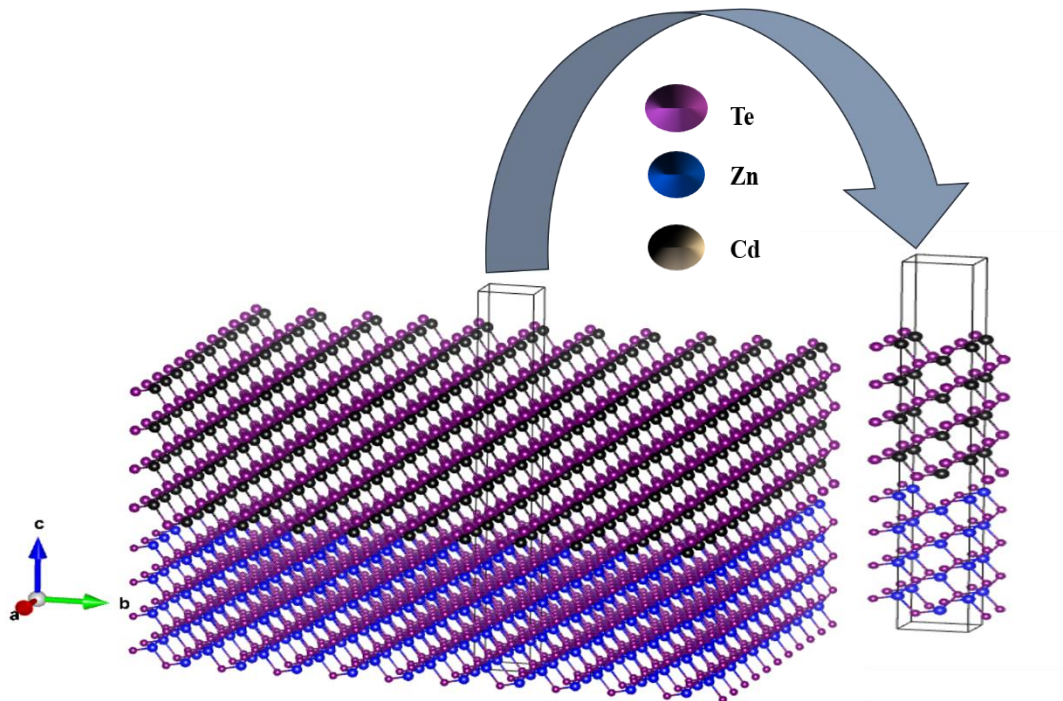


Figure 5.7: Optimized geometry of ZnTe/CdTe interface

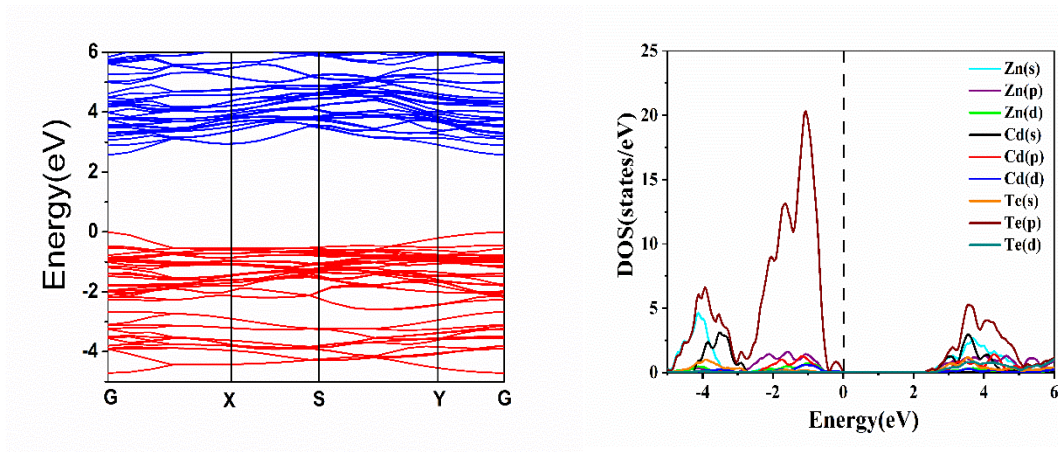


Fig 5.8 & 5.9: Electronic structure of hetero-structure

The band conduction structure, starting from 2.56 eV and forming the band gap, primarily consists of s/p-Cd/Zn and Te states. This region contains a blend of states of various elements.

5.3.2.2 Work function, band alignment, and the Charge Carrier Dynamics:

To understand the photovoltaic behavior and the usefulness of this hetero-interface in solar cells, relative band positions were studied, and their alignment in the heterojunctions. For this purpose, the surface work function of the heterojunction was estimated. The elemental work function was discussed in chapters 3 and 4. The work function for ZnTe/CdTe was 4.92 eV, as shown in Figure 5.10. A proper energetic position of the band edges of the photovoltaic materials may significantly enhance the efficiency of the solar cells.

When it comes to semiconductors, single-component have limited bandgap tailoring due to their intrinsic properties. However, by utilizing heterojunction in semiconductor devices, nearly unlimited and continuous bandgap variations can be achieved. Therefore in the next step, the band edge positions and their alignment in each of ZnTe, CdTe, and ZnTe/CdTe hetero-interface was studied and tried to understand the change in the band edge positions due to the formation of the hetero-junction by using the Mulliken electronegativity rules. The position of the CBM and VBM concerning the vacuum was calculated. Note that the value of the work function was more for ZnTe

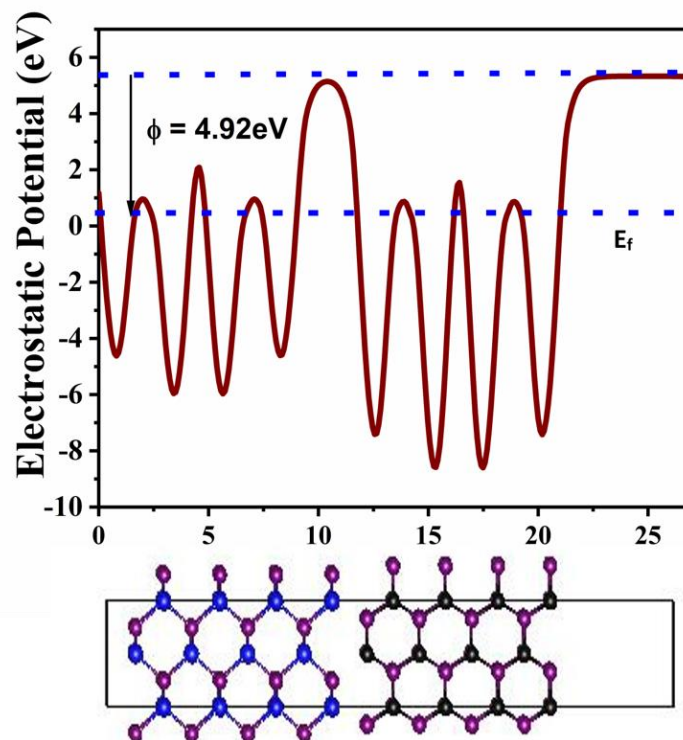


Fig 5.10: Average electrostatic potential of ZnTe/CdTe

than CdTe. So during the formation of the interface, electrons will move from CdTe to ZnTe until the Fermi level is aligned. At the equilibrium condition, the CB and VB of ZnTe moved upward by 0.31 eV, whereas the CB and VB of CdTe moved downward by 0.21 eV. As a result, a net valence band offset of 0.02 eV and a net conduction band offset of 0.89 eV was formed. These band offsets will help to separate the photogenerated charge carriers. The details of the aligned band-edge positions are depicted in Figure 5.11. When light irradiates on the CdTe absorber layer, photogenerated holes at the valence band of CdTe will easily flow through the valence band of highly conducting ZnTe due to a valence band offset. As a result, the positive charges will be pulled out and accumulated at the ZnTe part of the hetero-junction, leaving the photo-generated electrons in the CdTe portion. Finally, the hole accumulated in the ZnTe part will smoothly reach the back contact. Therefore, photoexcited electrons and holes will be well separated in the different parts of the hetero-interface. The photoelectrons which are piled up in the CdTe can be used for efficient photovoltaic reactions. Therefore the overall efficiency of the solar cell is expected to be improved significantly.

5.4 Summary:

The ZnTe/CdTe heterojunction showed improved optoelectrical behavior suitable for photovoltaic solar cell applications. Detailed theoretical investigations were carried out for ZnTe (110), CdTe (110), and ZnTe/CdTe heterointerface using hybrid density functional theory calculations. The theoretical result corroborates our experimental findings. The photovoltaic nature of the ZnTe/CdTe interface was further investigated by calculating the work functions of each system and estimating the proper band edge positions concerning the vacuum level. The valence and conduction band offsets were computed by aligning band edge positions of the respective parts of the heterojunction.

According to the calculation, a valence band offset created at the CdTe/ZnTe interface permits the free flow of photo-generated holes from CdTe to the back contact through ZnTe. Our present work not only demonstrates that the use of ZnTe as a back surface field layer (BSF) in CdTe solar cells would significantly improve the efficiency of the cell but also provides an idea to choose the novel BSF material to form the heterojunction, which in turn can control the recombination process.

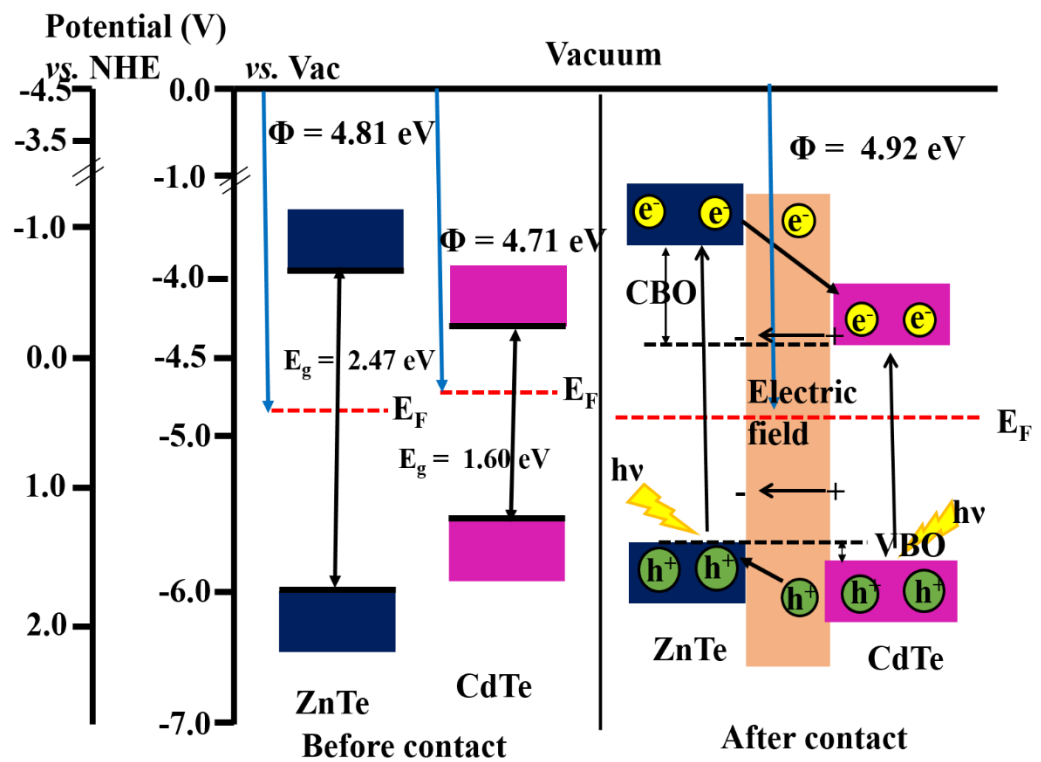


Fig 5.11: Band edge position and their alignment for ZnTe, CdTe and ZnTe/CdTe heterojunction

CHAPTER 6

INVESTIGATION OF CdSe AND ZnSe AS POTENTIAL BACK SURFACE FIELD LAYERS FOR CdTe-BASED SOLAR CELLS: A STUDY FROM FIRST PRINCIPLES CALCULATIONS

Overview:

In this chapter, the properties of two selenium-based materials, such as CdSe and ZnSe, were examined by using the DFT. Additionally, the applicability of these materials in CdTe solar cells was studied. Two critical parameters, i.e., charge transfer across the junction and proper band alignment at the interface, were explored.

6.1 Introduction:

The effective charge separation from the photo-generated excitons is one of the most crucial parameters to achieve high efficiency (Wang et al. 2018). When the light irradiates the semiconductor heterojunctions, the electrons should travel toward the n-type part of the junction, and holes should remain on the p-type part or propagate in the opposite direction (Husain et al. 2018). It can be achieved by employing proper band gap engineering and making a suitable band edge position in the thin-film heterojunction. In the case of CdTe-based solar cells, there exists high recombination of charge carriers due to the large effective masses of the charge carriers. Back surface field (BSF) layer material can be introduced in the CdTe-based solar cell (Amin et al. 2007b)(Gessert et al. 2009b) to reduce the recombination process. Dey et al. proposed a Cu₂Te BSF layer below the CdTe absorber layer and achieved a conversion efficiency of 22.51% (Dey et al. 2017). Ren et al. demonstrated that a buffer layer cell made of zinc magnesium oxide (ZMO) could improve the VOC and conversion efficiency of a CdTe solar cell. An efficiency of 16.76% was achieved by improving the thickness of the buffer layer (Ren et al. 2019).

In the present study, ZnSe and CdSe are used separately as the BSF layer in CdTe-based solar cells to enhance efficiency. CdSe is a II–VI semiconductor with a band gap of 1.7 eV (Ren et al. 2019) and is widely used in light-emitting diode and photocatalysis applications (Li et al. 2018)(Shenoy and Tarafder 2020). Similarly, ZnSe is a wide-bandgap semiconductor used to design photovoltaic cells. (Morkoç et al. 1994) CdSe and ZnSe have already been used as the window layer in CdTe solar cells (Li et al. 2018)(Khurram et al. 2017). However, up to our knowledge, the detailed electronic behavior of CdSe/CdTe and ZnSe/CdTe thin-film heterostructures and the charge transfer mechanism in these systems aiming toward their applications in the fields of the photovoltaic solar cell are not yet studied. In this work, using the first principle calculation, we investigated the detailed electronic structure of CdSe/CdTe and ZnSe/CdTe heterostructure. Finally, by employing the DFT, we have calculated the appropriate band edge position of the semiconductors and their heterostructures and estimated possible charge transfer mechanisms in these systems.

6.2 Computational Methodology:

The electronic structures of pristine ZnSe, CdTe, CdSe, and ZnSe/CdTe, CdSe/CdTe heterostructures are investigated by employing the density functional theory (DFT) calculations, as implemented in the Vienna ab initio simulation package (Kresse and Furthmüller 1996a). The projected augmented wave method was used in each calculation. The generalized gradient approximation was used, considering Perdew–Burke–Ernzerhof parameterization scheme to estimate the exchange and correlation potential (Grimme et al. 2010b). The long-range Van der-Waal interaction has been considered in all the heterostructure calculations employing dispersion correction for the density functional DFT-D3 method. A significant energy cut-off of 520 eV for wave function was used in each calculation to obtain accurate results. Begin with the energy-optimized bulk unit cell geometry of CdTe, ZnSe, and CdSe systems obtained by completely relaxing the cell parameters and atomic positions of the reported experimental structure. Next, the (110) surface slabs are constructed from the optimized bulk geometry. To understand the surface properties of the pure semiconductor, we have further relaxed the atomic positions in the surface-slab structure unit cell consisting of eight atomic layers (with 16 atoms). A 10 Å vacuum along the surface-normal direction was considered inside the unit cell to avoid the interaction between periodic images. The heterostructures are constructed from these optimized surface slabs by stacking them along the surface's normal direction. Two different heterostructures, ZnSe/CdTe and CdSe/CdTe, are constructed with 32 atoms in the unit cell. The initial separation between two different surface layers in each heterostructure is kept at a distance of 2.5 Å, which is the order of bond length of atoms in the interface region. All the atoms in the heterostructure are further relaxed inside the fixed unit cell by setting the force convergence criteria 0.01 eV Å⁻¹. Finally, the hybrid-DFT calculation for each surface slab and heterostructure has been employed to estimate the proper bandgap and band edge positions. We used Heyd–Scuseria–Ernzerhof (HSE 06) hybrid functional (Heyd et al. 2003) with a 25% Hartree–Fock exchange energy contribution. A 7 × 7 × 1 Monkhorst *K*-point sample was used for Brillouin zone integrations in each case. The band dispersion was investigated along the *K*-path G, X, S, Y, and G for all the structures.

6.3 Results and discussion:

6.3.1 Geometric-Structures:

To start with, the energy-optimized geometry of the pristine semiconductors and their heterostructures were obtained (i.e., CdTe, ZnSe, CdSe, ZnSe/CdTe, CdSe/CdTe) and studied their electronic properties. The ground state geometry of CdTe, ZnSe, and CdSe showed the zincblende structure (F-43m space group) with nearly the same lattice constant. The optimized bond lengths between Cd–Te, Cd–Se, and Zn–Se were 2.55, 2.64, and 2.20 Å, respectively. The lattice mismatch in ZnSe/CdTe and CdSe/CdTe heterostructures was 1.5% and 0.9%, respectively. The result showed that the scattering due to the formation of the interface would not be significant in the heterostructure, which in turn may not influence the recombination rate further (Koma 1999). The band-gap values of the energy-optimized structures were calculated using the hybrid HSE06 functional tabulated in Table 6.1, and they agree well with the reported experimental values (Pandey et al. 2005)(A. Chikwenze 2015)(Venkatachalam et al. 2007).

Table 6.1. Band gap energy, work function, and the band edge positions for pristine CdTe, ZnSe, and CdSe layers

System	E_g (eV)	Φ (eV)	E_{VB} (eV)	E_{CB} (eV)
CdTe	1.6	4.71	1.47	-0.13
ZnSe	2.56	5.11	2.19	-0.37
CdSe	2.14	5.30	2.51	0.37

Next, the formation energy E_{Form} was calculated to analyze the stability of the heterostructure by using the following formula.

$$E_{form} = E_{SC1} - E_{SC2} \quad (6.1)$$

E_{form} is the total energy of the relaxed hetero-structure, and E_{SC1} and E_{SC2} is the total energy of the first and second-layer semiconductor in the heterostructure, respectively. The formation energy per unit cell for ZnSe/CdTe and CdSe/CdTe was -0.138 and -0.396 eV, respectively. The negative formation energy indicates a strong interaction

between the layers and the stability of the interface. Optimized geometry structures of pristine semiconductors and their heterostructures are shown in Figure 6.1.

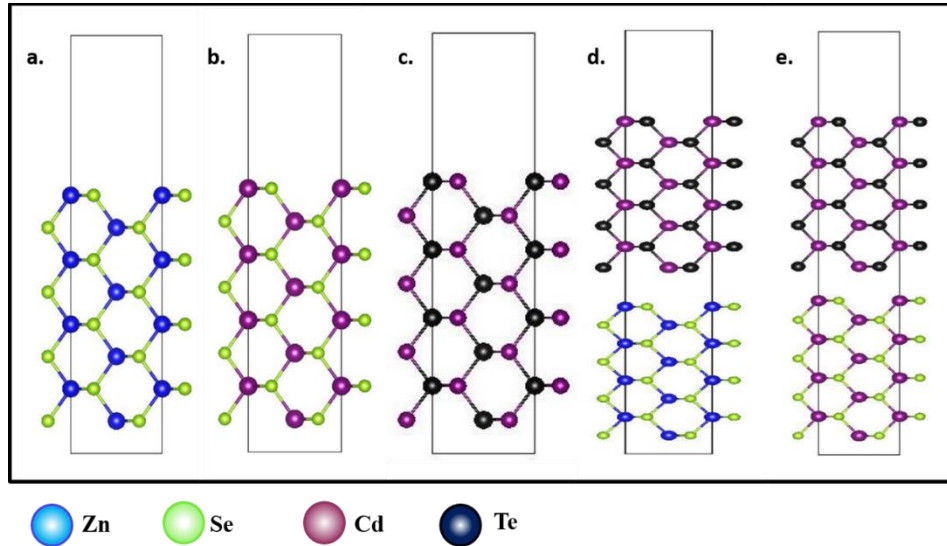


Figure 6.1: Optimized geometry structures of a) ZnSe, b) CdTe, c) CdSe, d) ZnSe/CdTe, and e) CdSe/CdTe heterostructures.

6.3.2 Electronic Structure

The effective charge separation and transformation of photo-generated charge carriers strongly affect photoconversion efficiency. To gain insight, it is necessary to analyze the electronic band structure of individual semiconductors layers present in the cell and their heterostructures (Kale and Lokhande 2000). In this work, the motivation was to choose a suitable BSF layer for CdTe-based solar cells to minimize the recombination losses at the back surface. A suitable BSF layer may significantly improve the open circuit voltage, short circuit current, fill factor, and hence the overall efficiency of the solar cells (AL-Oqla and Fares 2023). Wide band gap semiconductors are always preferable for BSF material because the band offset created between the BSF layer and the active layer help to push away the minority charge carriers from the active region, reducing the recombination losses at the back surface. Since CdTe is a p-type material (Britt and Ferekides 1993a)(Cusano 1963)(Yang et al. 2015), an ideal back surface layer should have a larger band gap than CdTe, and its conduction band minimum (CBM) should be energetically lower than that of CdTe CBM. To understand the band edge positions and their characters clearly, a detailed investigation of the electronic

structure of the pristine semiconductors and their interfaces was studied using the first principle calculation. The band structure of ZnSe, CdSe, CdTe, and their interfaces as shown in Figure 6.2. The band gaps of 2.56 and 2.14 eV were obtained for pristine ZnSe(110) and CdSe (110) slabs, respectively, which were much higher than that of a pristine CdTe (110) slab, which is only 1.60 eV. The theoretical band gap values for pristine semiconductors agree well with the reported experimental results (Kale and Lokhande 2000)(Sharma et al. 2020)(Gullu et al. 2020)(Schwab et al. 1992)(Mohammed et al. 2019).

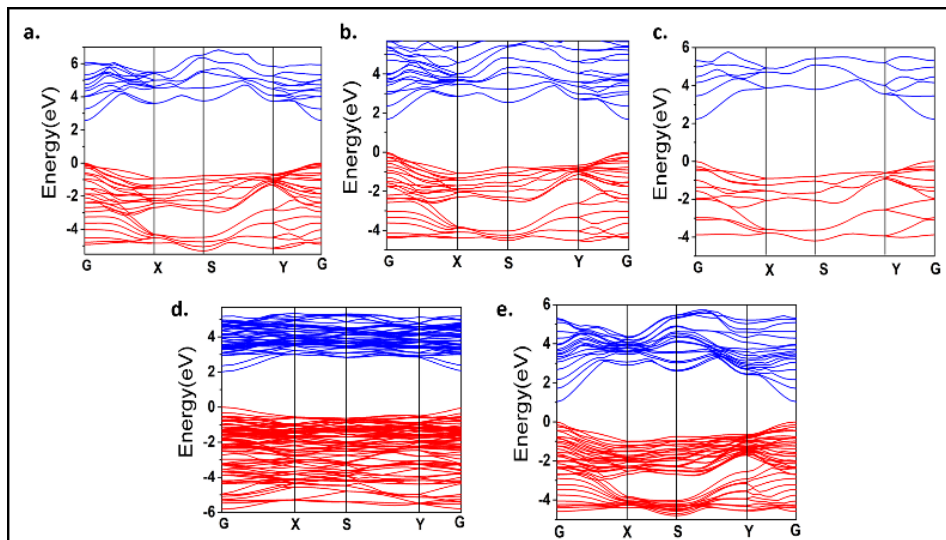


Figure 6.2: Electronic band structure of a) ZnSe, b) CdTe, c) CdSe, d) ZnSe/CdTe, and e) CdSe/CdTe heterostructures. Fermi energy is set at $E = 0$ in each graph. Red and blue color bands represent valence and conduction bands, respectively.

6.3.3 Optical Properties

In the context of solar cell application, detailed knowledge of the optical behavior of the semiconductors is essential as it indicates the light absorption process in the UV–vis region. The formation of heterojunctions may alter the optical behavior of the material present at the active layer in the cell. Therefore, the change in optical behavior of the CdTe thin film due to heterostructure formation with the BSF layers was studied. In this regard, the optimized geometry was used, and linear response theory was applied to estimate the complex dielectric function (ω) for the pristine semiconductors and their

heterostructures. Finally, the frequency-dependent absorption coefficients in the UV–vis light region are obtained by using the following relation

$$\alpha(\omega) = \sqrt{2}\omega \sqrt{\sqrt{\varepsilon_1(\omega)^2 + \varepsilon_2(\omega)^2} - \varepsilon_1(\omega)} \quad (6.2)$$

Here ε_1 and ε_2 are the real and imaginary parts of the complex dielectric function. The calculated optical absorption spectra of semiconductors and their heterostructures are shown in Figure 6.3. An improved absorption behavior was observed in the case of heterojunctions compared to each of the individual semiconductors. Note that the major peak in the absorption spectra was shifted toward the lower frequency range when the heterojunctions were formed. The heterostructures had high absorption intensity in a wide range from 400–700 nm and 350–700 nm for ZnSe/CdTe and CdSe/CdTe, respectively. This indicates a better light absorption in the visible light range than the individual pristine semiconductors.

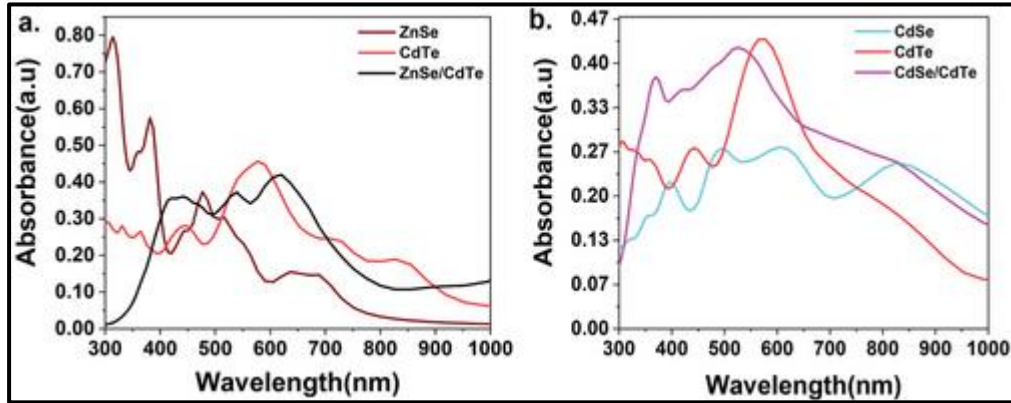


Figure 6.3: The absorption spectrum of a) ZnSe (brown), CdTe (red), and ZnSe/CdTe heterostructure (black), b) CdSe (cyan), CdTe (red) and CdSe/CdTe heterostructure (pink).

To understand the improved optical behavior in the heterostructure, the orbital nature of the band-edged positions was investigated by calculating the atom-projected partial density of states. In the case of pristine CdTe, the Cd-s and Te-p states contribute to the CBM, whereas Te-p states dominate the valance band maximum (VBM). Therefore the transition is mainly between s–p states. On the other hand, in the case of the ZnSe/CdTe heterostructure, the VBM consists of Te-p states, whereas both Cd-s and Te-p states are

present in the CBM. Similarly, in the case of the CdSe/CdTe heterostructure, the VBM is composed of Te-p states, whereas the main contribution of CBM comes from the Cd-s, Te-p, and Se-p states, as shown in the DOS plot in Figure 6.4. The absorption edge shift in the heterostructure was due to forming of a new hybridized electronic state near the band edge positions.

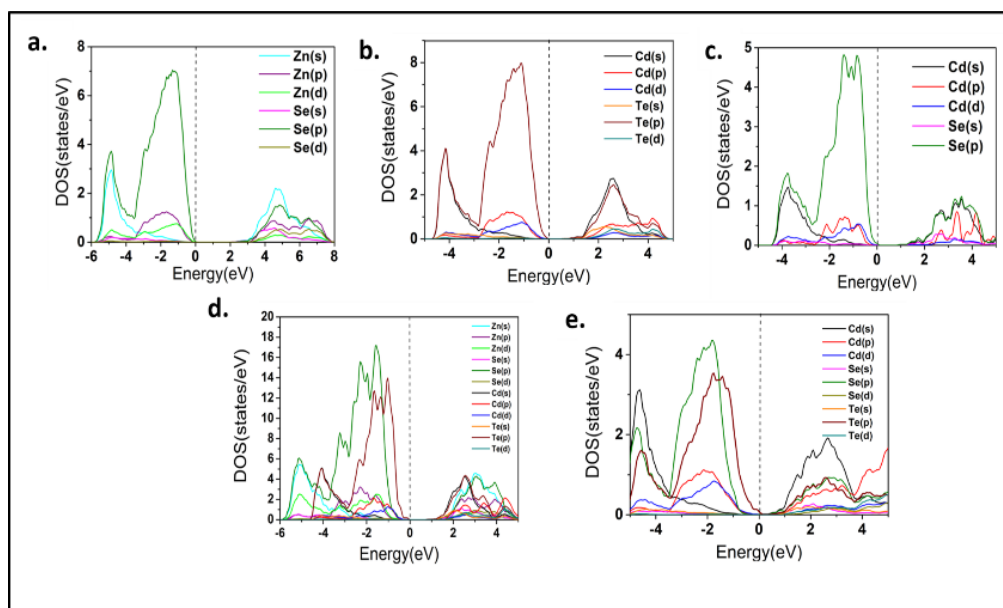


Figure 6.4: Partial density of states of a) ZnSe, b) CdTe, c) CdSe, d) ZnSe/CdTe, and e) CdSe/CdTe heterostructures. The Fermi energy is set at $E = 0$ in each graph.

6.3.4 Band Alignment and the Charge Carrier Dynamics

An accurate band edge position is essential to determine the dynamics of the photo-generated charges. The materials' work function helps to set the Fermi-energy position inside the semiconductor band gap region; hence, one can determine the band edge position concerning the vacuum level. Therefore, the work function of individual semiconductors and their heterostructure was investigated. For a semiconductor, the work function was estimated by constructing a surface with a large vacuum in the unit cell along the surface's normal direction and calculating the average Hartree potential. The work functions for ZnSe, CdSe, CdTe, ZnSe/CdTe, and CdSe/CdTe were found to be 5.11, 5.30, 4.71, 4.53, and 4.61 eV, respectively, as illustrated in Figure 6.5. In the case of interfaces, the calculated values of work functions were lower than the pristine semiconductors, which indicates that the formation of the interface is well-ordered and

the charge transport process is also coherent (Peng et al. 2012).

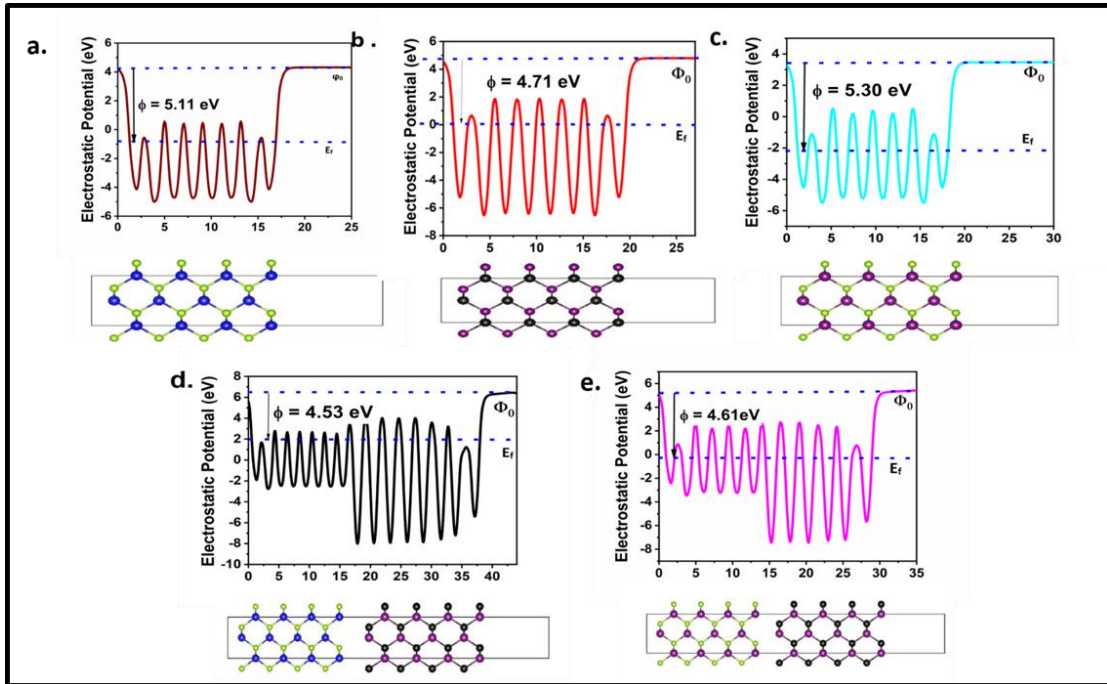


Fig 6.5: The estimated work function of a) ZnSe (110), b) CdTe (110), c) CdSe (110), d) ZnSe/CdTe, and e) CdSe/CdTe

The ionization potential of Te is less than the Se; as a result, the work function of CdTe is expected to have a lower value than that of CdSe. Similarly, ZnSe shows a higher work function than CdTe due to the lower ionization energy of Cd than Zn. Note that the layer with a lower work function decides the direction of the intrinsic charge transportation at the interface, consistent with the differential charge distribution plot, as shown in Figure 6.6. Therefore, due to the formation of the ZnSe/CdTe interface, the lower work function of the CdTe layer will be positively charged, and the movement of electrons will be from CdTe to ZnSe. At the same time, the ZnSe side of the junction is expected to be negatively charged due to the high electrostatic induction mechanism. Similarly, in the CdSe/CdTe interface, the CdTe side of the heterostructure will be positively charged, and CdSe will be negatively charged (Mohanta et al. 2020)(Mohanta et al. 2019).

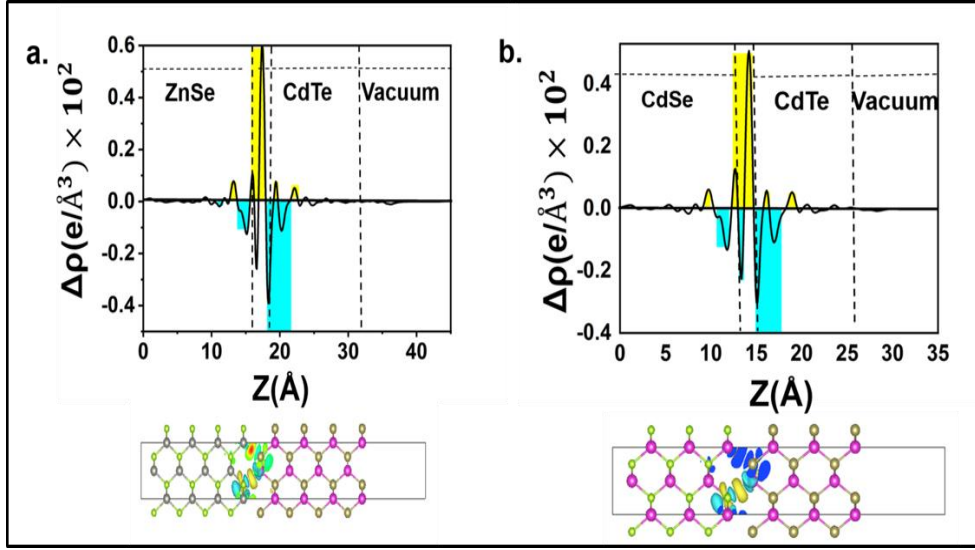


Figure 6.6: Charge density difference plots for a) ZnSe/CdTe and b) CdSe/CdTe heterostructures. The yellow and cyan color indicates the charge accumulation and charge depletion regions, respectively.

To understand the charge separation process at the interface, the charge density difference was calculated by using.

$$\Delta\rho = \rho_{interface} - \rho_{sc1} - \rho_{sc2} \quad (6.3)$$

Here ρ represents the charge density of the interface and pristine semiconductors. We observed the accumulation of electronic charge at the ZnSe side of the ZnSe/CdTe interface (denoted by yellow color) and depletion of the electron on the CdTe side (indicated by cyan color). Similarly, in the case of CdSe/CdTe heterostructures, the electron accumulates on the CdSe side, which is depleted from the CdTe part of the heterojunctions, as shown in Figure 6.6.

With the help of calculated work functions for different pristine semiconductors and their heterostructures, the band edge positions, their alignment, and the dynamics of photo-generated charge carriers were investigated. The valence band and conduction band edge position of different semiconductors were obtained using equations 2.26 and 2.27.

The χ values for the CdTe, ZnSe, and CdSe are 4.96, 4.8, and 5.14 eV, respectively. The E_{VB} and E_{CB} for the ZnSe were found to be at 2.19 and -0.37 eV, respectively, concerning the normal hydrogen electrode (NHE) scale. For CdSe, The E_{VB} and E_{CB} were found to be 2.51 and 0.37 eV concerning NHE, and for CdTe, the E_{VB} and E_{CB} were found to be at 1.47 and -0.13 eV, respectively. The valence band offset (VBO) and conduction band offset (CBO) for both the heterostructures were also estimated. The VBO and CBO for ZnSe/CdTe heterostructures were 0.08 and 1.04 eV, respectively. In the case of the CdSe/CdTe heterostructure, the VBO and CBO values were 0.14 and 0.68 eV, respectively. The details of the band edge position and calculated band offsets are shown in Figure 6.7a.

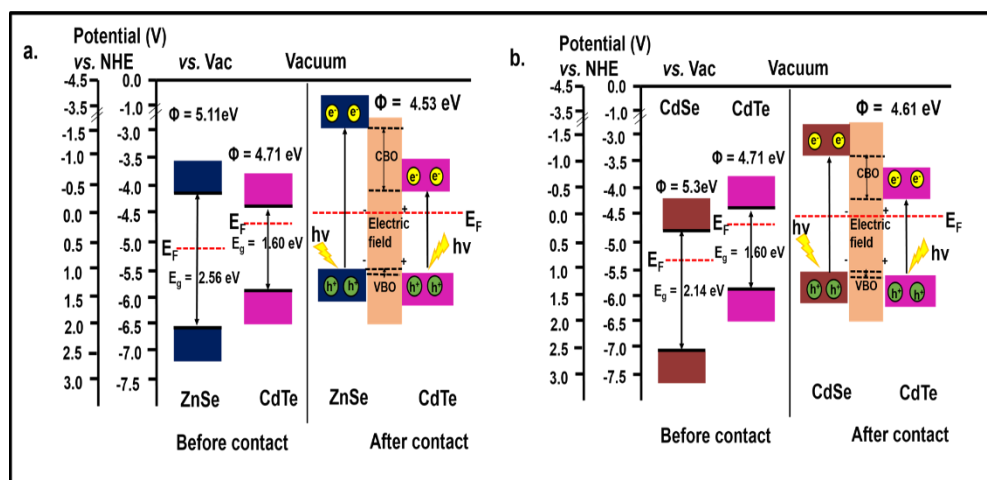


Figure 6.7: Relative band edge position and alignment in ZnSe, CdTe, CdSe, a) ZnSe/CdTe heterostructure, and b) CdSe/CdTe heterostructure with respect to the vacuum level.

Note that when the two layers come into contact, band bending of CdTe and ZnSe bands is expected near the interface due to realignment of the Fermi level. Since the work function of ZnSe is higher than CdTe, intrinsic electrons will flow from the CdTe side to the ZnSe side through the interface. Therefore, an intrinsic electric field will be generated at the interface region at the equilibrium condition. Upon light illumination, the internal electric field will accelerate photo-generated holes at CdTe toward ZnSe across the contact region. Notably, the upward bending of the CdTe CB band would act as a barrier for photo-excited electrons in CdTe and prevent the further diffusion of electrons into the CB of ZnSe. Similarly, the downward bending of ZnSe VB will help

to transport the holes created at CdTe VB efficiently to the ZnSe VB. (Xu et al. 2018)(Di et al. 2019) A similar phenomenon was observed in CdSe/CdTe heterojunctions, as shown in Figure 7b. A schematic representation of the process is shown in Figure 6.8. Therefore, both the ZnSe and CdSe can be used as the back surface field layer to separate the electron from the excitons and transport it to the back contact layer. The larger band offsets in the case of the CdSe/CdTe heterojunction indicate that an efficient photo-generated charge separation process can be achieved using this heterostructure in the solar cells.

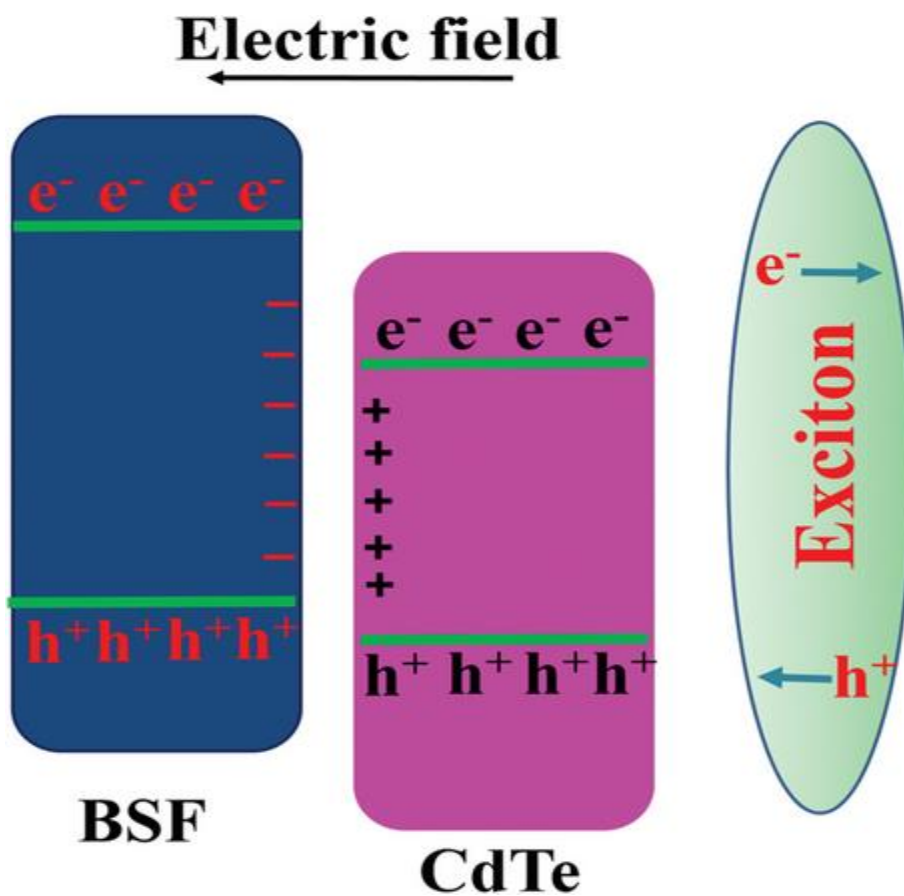


Figure 6.8: A schematic diagram for the photo-generated charge carrier separation process in BSF-layer/CdTe heterostructure.

6.4 Summary:

In conclusion, the suitability of CdSe and ZnSe thin films as back surface field layers in the CdTe solar cells was investigated. The hybrid- DFT calculation was used to study

the detailed electronic structure of ZnSe, CdSe, CdTe, ZnSe/CdTe, and CdSe/CdTe heterostructures. Both ZnSe/CdTe and CdSe/CdTe formed type-II heterojunctions having a band gap of 2.0 and 1.1 eV, respectively. Furthermore, both the heterojunctions showed improved light absorption behavior, and the absorption edge was red-shifted in the case of CdSe/CdTe. The proper band edge positions concerning NHE for the pristine semiconductors and their interfaces were estimated using the Mulliken electronegativity method. The obtained result showed that the band edge positions of the constituent semiconductors were significantly changed due to the formation of the hetero-structure, and a band offset both in the valence band and the conduction band was created. Due to the band offset at the interface, charges were redistributed at the interface region. In the case of ZnSe/CdTe, the intrinsic electrons will efficiently move from ZnSe to CdTe, and holes will move from the VB of CdTe to ZnSe. Similarly, for CdSe/CdTe, the intrinsic electrons will move from the CB of CdTe to CdSe, and holes will move from the VB of CdSe to CdTe. As a result, a local field will be created at the interface region, which will help to separate the photo-generated electrons and holes in the two different parts of the heterojunction. This field will also help to efficiently transport the photo-generated charges to the contacts and significantly reduce the recombination loss in the solar cells.

CHAPTER 7

SYNTHESIS AND CHARACTERIZATION OF Cu DOPED CdTe THIN FILMS FOR SOLAR CELL APPLICATIONS

Detailed theoretical, experimental studies on the pristine metal chalcogenide nanostructures and their application in the CdTe solar cells have been discussed in the previous chapters. One disadvantage of CdTe is the challenge of reaching high Carrier density, which is hindered by self-compensation resulting from intrinsic defects such as vacancies, interstitial defects, and grain boundaries. Improving the energy yield performance of CdTe solar cells is a major challenge, mainly due to their low acceptor density. To achieve higher PCE, dopants can be used. Based on this, the next aim is to examine the behavior of doped CdTe thin films for solar cell applications. This chapter describes the structural, morphological, and optical properties of the undoped and Cu-doped CdTe thin films.

7.1 Introduction:

Semiconductor-based multilayer-junction solar cell technology has become prominent for harvesting renewable energy from sunlight. The efficiency of solar cells can be improved significantly with a controlled modification of layer structures. CdTe thin-film could be an effective material in this technology because of its interesting electronic and optical behavior. The laboratory framework has already reported high efficiency of up to 15.8% of CdTe/CdS-based multilayer solar cells (Britt and Ferekides 1993b). The efficiency could be further improved using a multilayer of the same semiconductor containing different types of injected carriers. One advantage is that the lattice mismatch will be minimal, and the grain size is expected to be significant. CdTe thin films exhibit interesting optoelectronic properties. The band gap of CdTe and doped CdTe thin films are in the good range for photovoltaic application. Therefore, controlled doping of these materials with p and n-type carriers and multilayers of doped films in the solar cell may significantly improve cell efficiency. On the other hand, photo corrosion is one of the significant problems in photovoltaic devices. Multilayers with suitable materials that provide reasonable band offsets in valence and conduction bands may resolve that issue. CdS/CdSe and CdTe/CdS are good examples of type II semiconductors where a significant valence band offset suitably separates and transports the hole from the photo-generated excitons and reduces the photo corrosion process (Amani-Ghadim et al. 2022; Khan et al. 2020; Lu et al. 2020; Monika et al. 2023; Nasir et al. 2020). However, depositing a clean crack/pinhole-free interface is also challenging. It was reported that CdCl₂ helps in the passivation of grain boundaries which in turn helps to improve the interface morphology of Cd-based semiconductor multilayers such as CdTe/CdS (Duffy et al. 2000; Edwards et al. 2000; Ghosh et al. 2013; Moutinho et al. 1997).

CdTe is an II-VI binary semiconductor with a direct band gap of 1.5 eV. Also, the absorption coefficient is very high in this material. It can be made in both p-type and n-type semiconductors using suitable dopants (Dzhafarov et al. 2005; Gordillo et al. 1995b; Hwang et al. 1996; Rajavel and Summers 1992; Zhao et al. 2016). Therefore CdTe thin film can be used as an efficient absorber layer in solar cells. According to commercial perception, it is also an essential thin film as the compound is highly stable

in thin-film form and has less production cost than Si PV cells. On the other hand, using a carrier-injected multi-layer structure of CdTe in the solar cell may provide excellent efficiency as the interface scattering and recombination rate can be controlled upon controlling the p and n doping of the system. However, a detailed investigation of p and n-type doped CdTe and their junction is essential. In this work, we have considered CdTe as a parent compound and synthesized the p-counterpart of the CdTe-based solar cell by doping Cu atoms in the polycrystalline CdTe films. The CdTe polycrystalline films can be grown by several methods such as closed space sublimation (CSS) (Albin et al. 2002; Bonnet 2000; Ferekides et al. 2000), chemical vapor deposition (Chou et al. 1986; Chu 1988), sputtering (Kulkarni et al. 2017; Potter and Simmons 1990), pulsed laser deposition (PLD) (Pandey et al. 2005), molecular beam epitaxial method (Farrow et al. 1981; Ringel et al. 1991b), screen printing (Matsumoto et al. 1984; Nakano et al. 1986), thermal evaporation (Ablekim et al. 2020; Brus et al. 2014; Khairnar et al. 2003). Among all these methods, thermal evaporation provides excellent purity of the film due to the high vacuum condition. Also, this technique provides a high deposition rate. Therefore we have used this technique to synthesize the Cu-doped CdTe system and study the effect of copper concentration on the structural and optical properties of the CdTe thin film.

7.2. Experimental details

The thermal evaporation technique was used to deposit the undoped and Cu-doped CdTe thin films on a glass substrate. The glass substrate was cleaned ultrasonically. Less than 5×10^{-6} Torr pressure was maintained during synthesis using a diffusion pump backed by a rotary pump. CdTe (purity 99.9999%, powder) and Cu (99.995%, powder) were used to make the film. A tantalum boat was used as a source. The films were prepared at room temperature, and air annealed at 100 °C to get the stoichiometry films. The deposition rate was maintained at nearly 46 nm/min. CdTe powder and Cu powder were co-evaporated from a boat. The thickness of the film was measured by the gravimetric method, and it was maintained at nearly 420nm. The structural properties of the films were demonstrated by the Rigaku Miniflex600 X-Ray diffractometer ($\lambda_{\text{CuK}\alpha} = 1.54\text{\AA}$). The surface and elemental composition of the films were studied by Ultra 55 scanning electron microscopes. The absorption spectra of CdTe and Cu-doped

CdTe films were obtained by the Shimadzu MPC3600 UV–VIS-NIR spectrometer in the 300 nm-2000 nm wavelength range. The thickness of the film was measured by the gravimetric method. In this study, the thickness of 420 nm was maintained for all the samples.

7.3. Results and discussion:

7.3.1. X-ray diffraction analyses:

Figure 7.1 shows the XRD pattern of the CdTe and Cu-doped CdTe thin films. It was observed that all the films were polycrystalline in nature with the cubic structure of CdTe (JCPDS card No.-00–015-0770) and showed a predominant peak at $2\theta = 23.7^\circ$ which corresponds to (1 1 1) plane. Using Bragg's law, the inter-planar spacing (d_{hkl}) was estimated from the XRD data.

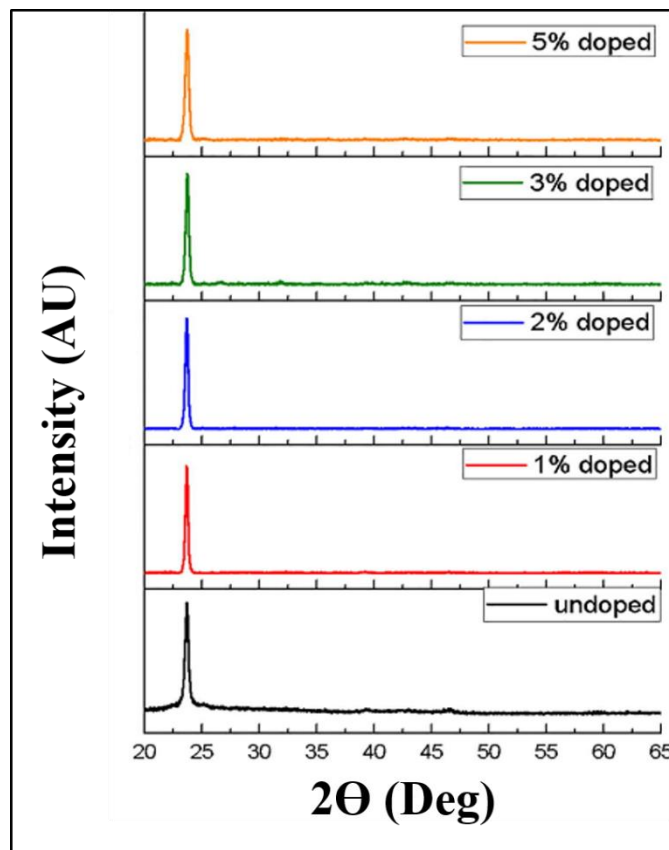


Fig. 7.1. XRD images of the deposited films show the shifting of the 2θ value towards a higher angle.

The Debye Scherrer's formula was used to calculate the crystallite size (D in nm) (Holzwarth and Gibson 2011). The Microstrain of the sample was then evaluated by using the following equation:

$$\epsilon = \frac{\beta \cos \theta}{4} \quad (7.1)$$

Where 'β' is the FWHM of the diffraction peak and 'θ' is the Bragg angle.

The lattice parameter for the cubic crystal system was calculated by using the relation as (Kumar et al. 2005),

$$\frac{1}{d_{hkl}^2} = \frac{h^2 + k^2 + l^2}{a^2} \quad (7.2)$$

Where h, k, l are the Miller indices, 'd' is the interplanar spacing, and 'a' is the lattice constant. The values of all these parameters were measured for different doping concentrations and listed in Table 7. 1.

Table 7.1 XRD data of Cu-doped CdTe thin films with different doping concentrations.

Doping Percentage	2θ (in deg)	d (in Å⁰)	a (in Å⁰)	D (in nm)	ε × 10⁻³
Undoped	23.684	3.753	6.501	25.690	1.40
1%	23.672	3.755	6.504	28.835	1.25
2%	23.676	3.754	6.503	26.575	1.36
3%	23.711	3.749	6.494	23.949	1.51
5%	23.723	3.747	6.490	21.573	1.67

The shift in the 2θ value towards a higher angle was observed with an increment of the doping concentration. However, the interlayer distance was not altered. From the XRD plot, it was observed that the peak intensity reduced with an increment of the Cu concentration, indicating that the impurity atoms are present in the system.

The change in crystallite size with a change in doping concentration is shown in Figure 7. 2. We observed that the crystallite size decreases almost linearly up to 3% doping concentration. A significant change was observed in the case of 5% doping. Since the crystallite sizes are reduced in higher doping concentrations, the microstrain is expected

to increase due to the enhancement of the surface energy, which is confirmed by the strain versus doping concentration plot shown in blue color in Figure 7.2.

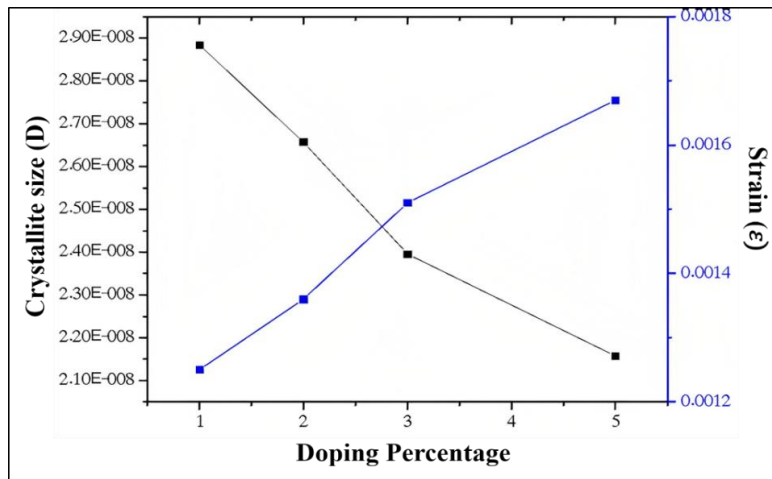


Figure 7.2. Change in crystallite size (black) and strain (blue) due to a change in doping concentration.

7.3.2 Morphological studies

Next, the surface morphology of the deposited thin films was studied by using scanning electron microscopy (SEM). All the deposited films were crack and pinhole-free, as shown in Figure 7.3. The composition analysis was performed by using EDAX, confirming the presence of Cd, Te, and Cu. A uniform distribution of Cu was found on the deposited thin films. The average grain size and elemental composition (found from EDAX) are tabulated in Table 7.2. In the case of Cu-doped CdTe, the Cu atom was expected to replace the Cd atom. Due to a significant difference in atomic radii of Cu and Cd, considerable microscopic strain will be experienced by the doped sample. This will reduce the grain size of the sample. A significant change in grain size was observed for the 5% Cu-doped CdTe sample.

Table 7. 2. Average grain size and elemental analysis of deposited films.

Doping percentage	Cd	Te	Cu	Average grain size (in nm)
Undoped	49.87	50.13	0	61.430
1%	47.74	50.73	1.5 3	82.007
2%	46.89	50.91	2.2 0	69.047
3%	46.82	49.93	3.2 5	61.132
5%	48.71	45.72	5.5 7	51.185

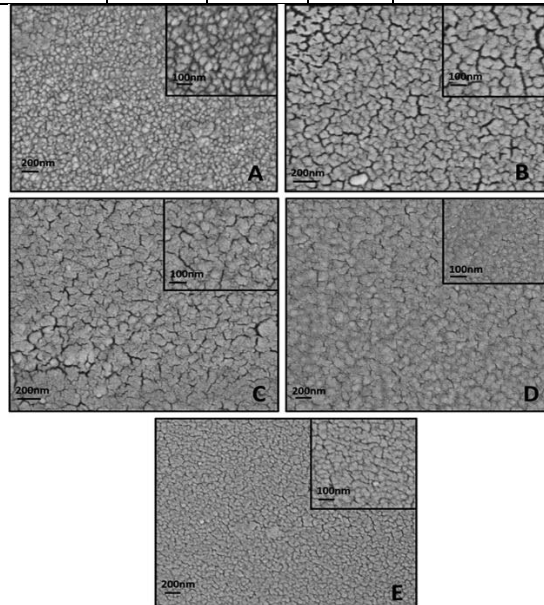


Figure 7.3. SEM images of undoped CdTe thin film (A), 1% Cu doped CdTe thin Film (B), 2% Cu doped CdTe thin film(C), 3% Cu doped CdTe thin film (D), and 5% Cu doped CdTe thin film. (E).

7.3.3 Optical properties:

7.3.3.1 Transmittance:

The deposited film's transmittance was decreased with increasing Cu content, shown in Figure 7.4. This is mainly because of the enhancement of the scattering process. In

the case of 5% Cu-doped film, the transmittance reduced drastically. Note that the grain sizes significantly decreased in the 5% Cu-doped sample. Therefore the scattering due to the grain boundary dominated in this case which affects the transmission process, and the transmittance was reduced significantly.

7.3.3.2 Optical band gap calculation:

The absorption spectra of the deposited films were plotted in Figure 7.5. The optical band gap of semiconductor thin films can be calculated from Tauc's relation. The optical band gap of undoped and doped CdTe thin films was analyzed by plotting the graph of photon energy versus $(\alpha h\nu)^2$, considering the direct transition. The value of the bandgap was then estimated by extrapolating the linear portion of the spectra where $(\alpha h\nu)^2 = 0$. The band gap of the undoped CdTe thin film was 1.52 eV. The band gap was decreased with an increase in the doping percentage. Replacing a Cd with a Cu atom in the lattice produces electron deficiency. The acceptor level due to these doped Cu atoms should appear inside the band gap near the valence band, which reduces the optical band gap of the system. On the other hand, no significant change in the bandgap with higher doping concentrations assures the control of the trap states and impurity scattering. The optical band gap for undoped and doped films is tabulated in Table 7.3.

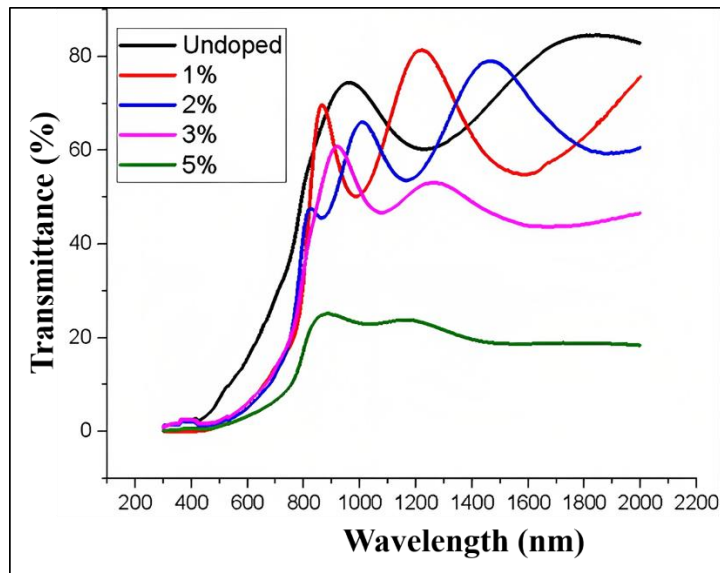


Figure 7.4. Transmittance plot of undoped and Cu-doped CdTe thin films.

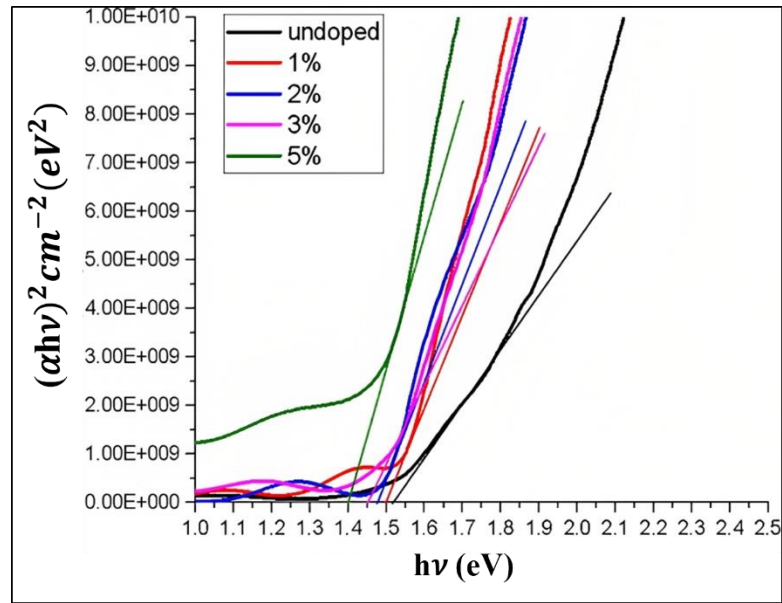


Fig. 7.5 Tauc's plot for undoped and Cu-doped CdTe thin films shows that the band gap decreases with increased doping percentage. This is maybe due to defect states.

Table 7.3. Band gap and average transparency of the deposited films

Doping Percentage	Band Gap (in eV)	Average Transparency (%)
Undoped	1.52	82
1%	1.50	81
2%	1.48	79
3%	1.45	60
5%	1.40	21

7.4 Summary:

CdTe and Cu-doped CdTe thin films were prepared using PVD. Characterization of deposited films was done by using XRD, SEM, and EDAX analysis that assured the quality of the sample. The optical properties of the synthesized sample showed that the band gap and the carrier concentration of the CdTe thin film could be effectively controlled while making the p-counterpart of the CdTe-based p-n junction solar cell.

The band gap is slightly decreased with the increase of doping concentration. However, these films can be used to absorb light for longer wavelengths. The optoelectronic behavior of the doped CdTe sample can be improved by up to 3% Cu doping. Therefore, up to 3% Cu-doped CdTe is suitable for the p-counterpart of highly efficient CdTe-based p-n junction solar cells.

CHAPTER 8

SULFUR ALLOYED Sb_2Se_3 AND A NEW 2D MATERIAL FOR SOLAR CELL APPLICATIONS

Overview:

In the previous chapter, the effect of doping on the CdTe absorber layer was discussed. Cadmium is one of the top 6 deadliest and most toxic materials known. The cadmium telluride films are typically recrystallized in a toxic compound of cadmium chloride. In CdTe, Cadmium is relatively abundant; but the Tellurium (Te) is a scarce element (1-5 parts per billion in the Earth's crust). In this chapter, the properties of Sb_2Se_3 and S alloyed Sb_2Se_3 systems were studied with the aim of using them as an absorber layer in the next generation solar cells. Additionally, a two-dimensional Mxenes, ScHfNNOH, has been investigated and found to be suitable for the application in solar cell. Finally, using Sb_2Se_3 and ScHfNNOH, a heterostructure junction was constructed, and thoroughly investigated from the first principles calculation, aiming to its application in solar cell.

8.1 Introduction:

Recently, Sb_2Se_3 has gained significant attention in solar cell technology due to its magnificent optoelectrical behavior. It is a non-toxic, earth-abundant compound with a band gap of 1.2 eV (Patrick and Giustino 2011b) and a high absorption coefficient ($>10^5 \text{cm}^{-1}$) (Zhou et al. 2014) and would be very appropriate to use as an absorber layer in the solar cell. (Chen et al. 2017b; Li et al. 2016a; Tumelero et al. 2016). High carrier mobility of about $10 \text{cm}^2/\text{V}\cdot\text{s}$ was estimated in this material (Chen et al. 2017a). In 2009, Messina et al. synthesized the first Sb_2Se_3 -based solar cell synthesized and achieved a PCE of 0.66% (Messina et al. 2009). Recently, the PCE achieved by the Antimony selenide solar cell is 7.48% (Wen et al. 2018). AS OF NOW, the PCE of Sb_2Se_3 solar cells falls short of the theoretical value of 23.8% (Filip et al. 2013). It is generally accepted that the band gap of the absorber layer is a significant factor in establishing the PCE (Yang et al. 2016). With control over the band gap, the open-circuit voltage (V_{oc}) and short-circuit current density (J_{sc}) can be optimized for maximum power conversion efficiency (PCE). When there's an increase in V_{oc} , it usually comes with a decrease in J_{sc} because of the rise in band gap and vice versa.

A class of 2D materials called MXenes has been successfully synthesized, showing potential for various applications in materials science and engineering, including transparent conducting layers in solar cells (Bai et al. 2021; Kumar et al. 2021a) (Tang et al. 2019), electrodes in Li-ion batteries (Du et al. 2018; Kim et al. 2015; Li et al. 2019), Field effect transistors (Liu et al. 2020; Xu et al. 2016, 2022), photocatalysts (Guo et al. 2016; Kuang et al. 2020; Xu et al. 2022; Zubair et al. 2022), and optical nanodevices (Hasan et al. 2021; Michael et al. 2019). Therefore, Mxenes attracted many researchers to study the experiment and the theoretical observations. Most of the mxenes are metallic in nature. However, a few of them, such as Ti_2Co_2 , Hf_2Co_2 , Sc_2Co_2 , and Sc_2CF_2 , possess semiconducting behavior (Khazaei et al. 2013). Mxene based on transition metal nitrides, exhibit exceptional thermal stability and are ideal for preparing absorber layers at high temperatures (Fleming et al. 2007; Hou et al. 2010). Additionally, they possess excellent barrier properties (Lingwal and Panwar 2005). Gao et al. first reported the preparation of titanium nitride nanotubes and the interface with the Ti by following the nitridation (Jiang et al. 2009). In 2016, researchers

successfully synthesized a two-dimensional Ti_4N_3 nitride MXene (Urbankowski et al. 2016). This success has inspired further scientific efforts to study the family of 2D TMNs, with a particular focus on nitride MXenes.

This chapter discussed the detail investigation of electronic structure and optical properties of different Sulphur doped Sb_2S_3 layers, a new ScHfNNoH – Mxene and their heterostructures, from first principles calculations. Interestingly, this particular Mxene showed semiconducting properties with a wide band gap, therefore could be used as a window layer in the Sb_2Se_3 based solar cell. Finally, considering $\text{Sb}_2(\text{S}_{0.7}\text{Se}_{0.3})_3$ as the optimal absorber layer, the optical absorbance of the absorber layer, window layer, and their heterostructure was studied using the density functional theory.

8.2 Theoretical methodology:

The electronic structures of pristine Sb_2Se_3 , Sb_2S_3 , and S alloyed Sb_2Se_3 were investigated using the density functional theory (DFT) calculations, as implemented in the Vienna ab initio simulation package. (Kresse and Furthmüller 1996a) The projected augmented wave method was used in each analysis. The generalized gradient approximation was used, considering Perdew– Burke– Ernzerhof parameterization scheme to estimate the exchange and correlation potential (Grimme et al. 2010b). A significant energy cut-off of 520 eV for wave function was used in each calculation to obtain accurate results. Begin with the energy-optimized bulk unit cell geometry of the pristine and alloyed systems obtained by completely relaxing the cell parameters and atomic positions of the reported experimental structure. Next, the (130) surface slab (which is energetically most stable surface) of different S doped Sb_3Se_2 was constructed from the optimized bulk geometry. To understand the surface properties, the atomic positions in the surface-slab structure unit cell consisting of 40 atoms were further relaxed. A 10 Å vacuum along the surface-normal direction was considered inside the unit cell to avoid the interaction between periodic images. Finally, the hybrid-DFT calculation for the surface slab was employed to estimate the proper bandgap. Heyd–Scuseria–Ernzerhof (HSE 06) hybrid functional (Heyd et al. 2003) with a 25% Hartree–Fock exchange energy contribution was used. A $7 \times 7 \times 1$ Gamma K -point sample was used for Brillouin zone integrations in each case. The band dispersion was

investigated along the *K*-path G, X, S, Y, G, and S for S4(130). Furthermore, The 2D Mxenes ScHfNNOH with the vacuum, consisting of 48 atoms, was relaxed by considering the energy convergence criteria of 520 eV. For the energy optimization, the U_{eff} of 3 eV was used for the Sc and Hf atoms. The heterostructures were constructed from these optimized surface slabs by stacking them along the surface's normal direction. All the atoms in the heterostructure were further relaxed inside the fixed unit cell by setting the force convergence criteria 0.01 eV \AA^{-1} . Finally, the DFT+U calculation was used for the surface slab and heterostructure to estimate the proper band gap.

8.3 Results and discussion:

8.3.1 Crystal structure of S alloyed Sb_2Se_3 :

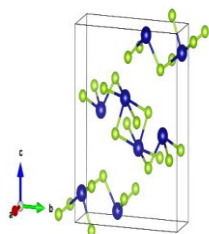
Physical properties are intricately linked to overall energy. For instance, a crystal's equilibrium lattice constant is the constant that reduces the total energy to a minimum. By calculating the total energy, it is possible to determine any physical property that is associated with it. Here the Sb_2Se_3 crystal structure was considered and optimized using the density functional theory. The experimental data are consistent with the conclusion that Sb_2Se_3 has a *pnma* space group orthorhombic structure (Lokhande et al. 2002; El Radaf 2019). The lattice parameter was found to be $a = 4.03 \text{ \AA}$, $b = 11.53 \text{ \AA}$, $c = 12.84 \text{ \AA}$, $\alpha = \beta = \gamma = 90^\circ$. The main aim was to tune the band gap of Sb_2Se_3 for solar cell applications. To achieve this, the first attempt was to alloy with different materials. Modifying the dopant content can significantly impact the band gap and band dispersion, resulting in a lower effective mass of the carriers and increased electrical conductivity and mobility. The content of the S in Sb_2Se_3 was changed from 50% to 100%. Furthermore, all the structures were optimized and allowed to attain the minimum energy state. The optimized structures are depicted in Figure 8.1.

The samples were named as follows,

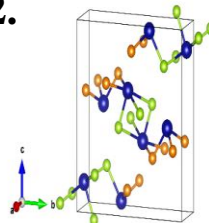
Pristine Sb₂Se₃	S1
<i>Sb₂(S_{0.5}Se_{0.5})₃</i>	S2
<i>Sb₂(S_{0.6}Se_{0.4})₃</i>	S3
<i>Sb₂(S_{0.7}Se_{0.3})₃</i>	S4
<i>Sb₂(S_{0.8}Se_{0.2})₃</i>	S5
<i>Sb₂(S_{0.9}Se_{0.1})₃</i>	S6
Pristine Sb₂S₃	S7

In the case of pristine Sb₂Se₃, the bond length, Sb-Se, was 3.03 Å, whereas for Sb₂S₃, the bond length, Sb-S, was 2.87 Å. The reason for the stronger bonding between S and Sb compared to Se and Sb is likely due to S having a smaller atomic radius and a higher electronegativity than Se. This leads to a more optimal bonding arrangement between S and Sb.

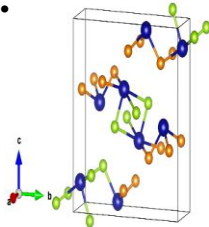
S1.



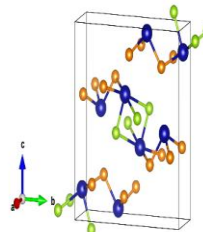
S2.



S3.



S4.



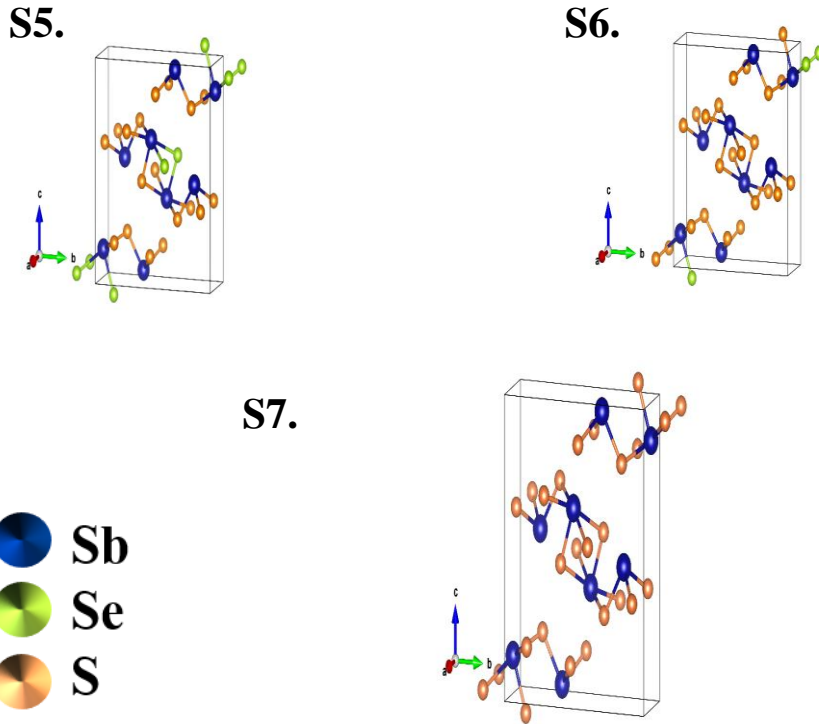


Figure 8.1: Optimized bulk geometry of $\text{Sb}_2(\text{S}_x\text{Se}_{1-x})_3$ for $x =$ (S1) 0, (S2) 0.5, (S3) 0.6, (S4) 0.7, (S5) 0.8, (S6) 0.9, (S7) 1.0.

8.3.2 Electronic properties of S alloyed Sb_2Se_3 :

8.3.2.1 Band structure:

The optical and electrical properties are essential in checking the material's suitability for application in solar cells. The electronic properties of all the samples were studied. The electronic band structures of the samples are shown in Figure 8.2 along the high symmetry points. GGA underestimated the band gap for all samples (Caracas and Gonze 2005; Carey et al. 2014). Therefore, hybrid functional HSE 06 was used to calculate the accurate band gap of the structures. The band gap for Sb_2Se_3 and Sb_2S_3 was 1.22 eV and 1.85 eV, respectively, which matches the experimental findings (Kumar et al. 2021b)(Ghosh and Varma 1979). Note that all the samples possess an indirect band gap, as shown in Figure 8.2. It is possible that the increased covalence of $\text{Sb}_2\text{Se}_{1-x}\text{S}_x$ is a result of higher S-dopant concentrations. This is due to the smaller atomic radius of S compared to Se, resulting in stronger S-Sb covalent bonds than Se-

Sb bonds. Consequently, there is an increase in the band gap. The bandgap and the position of VBM and CBM for all the samples are charted in Table 8.1.

Table 8.1: Band gap and the position of VBM and CBM for S alloyed Sb_2Se_3

X	0 (S1)	0.5 (S2)	0.6 (S3)	0.7 (S4)	0.8 (S5)	0.9 (S6)	1.0 (S7)
E_g (eV)	1.22	1.29	1.42	1.50	1.57	1.68	1.85
VBM (eV)	-0.20	-0.23	-0.20	-0.22	-0.22	-0.23	-0.24
CBM (eV)	1.01	1.06	1.22	1.28	1.34	1.44	1.61
High symmetry points	Y-Z	Z-B	Z-B	Y-G	Z-G	Z-G	Y-G

8.3.2.2 Density of states:

To understand the change in band gap for different compositions of S and Se, the PDOS of all the structures were studied and depicted in Figure 8.3. All the major peaks were located in the energy interval -6 to 0 eV (VB). In the case of Sb_2Se_3 , the VB was dominated by Se-p and Sb-p, and Sb-s states. In contrast, the CB was dominated by the Sb-p and Se-p.

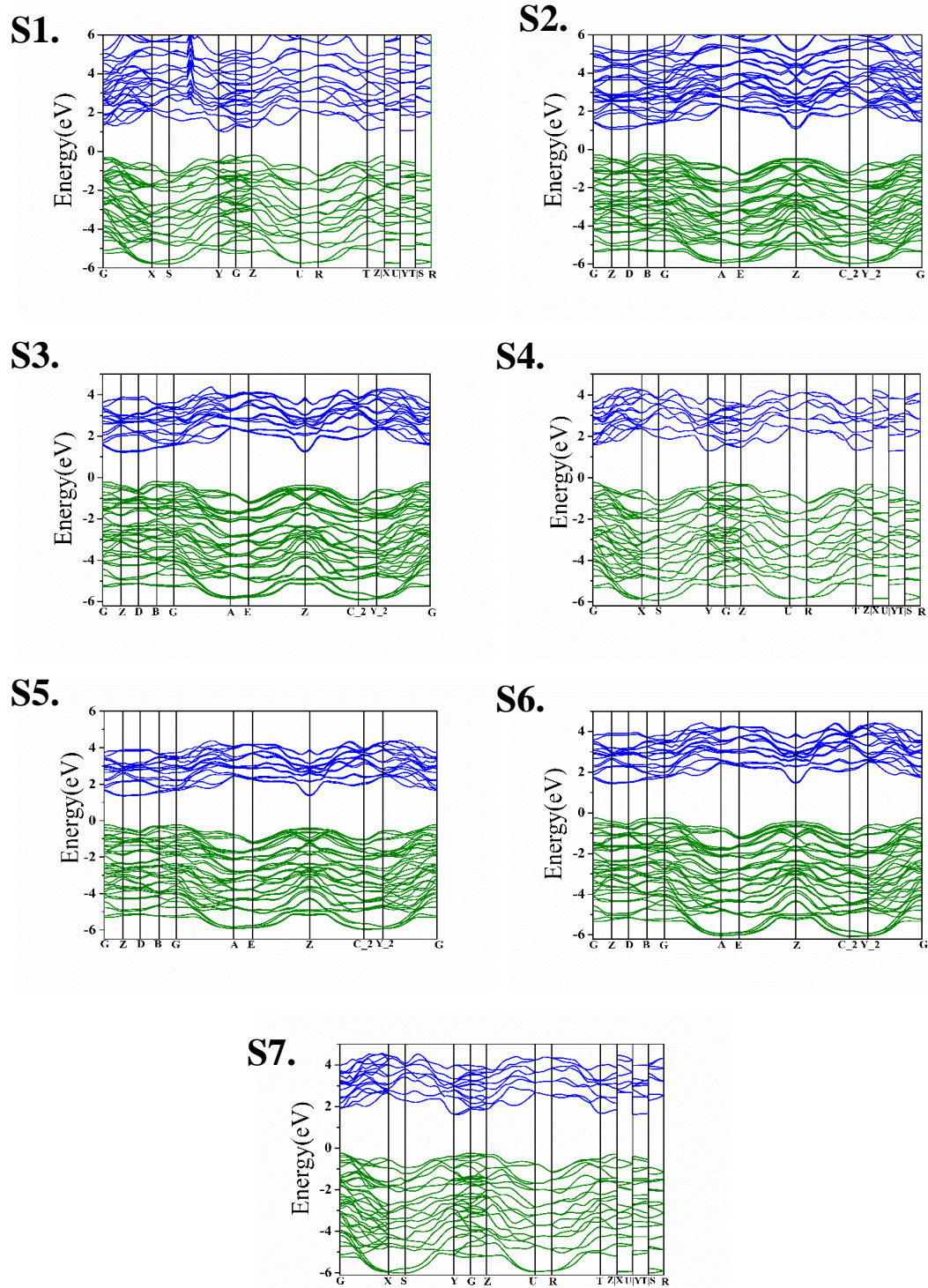


Figure 8.2: Band structure of $\text{Sb}_2(\text{S}_x\text{Se}_{1-x})_3$ for $x =$ (S1) 0, (S2) 0.5, (S3) 0.6, (S4) 0.7, (S5) 0.8, (S6) 0.9, (S7) 1.0 using HSE06 functional.

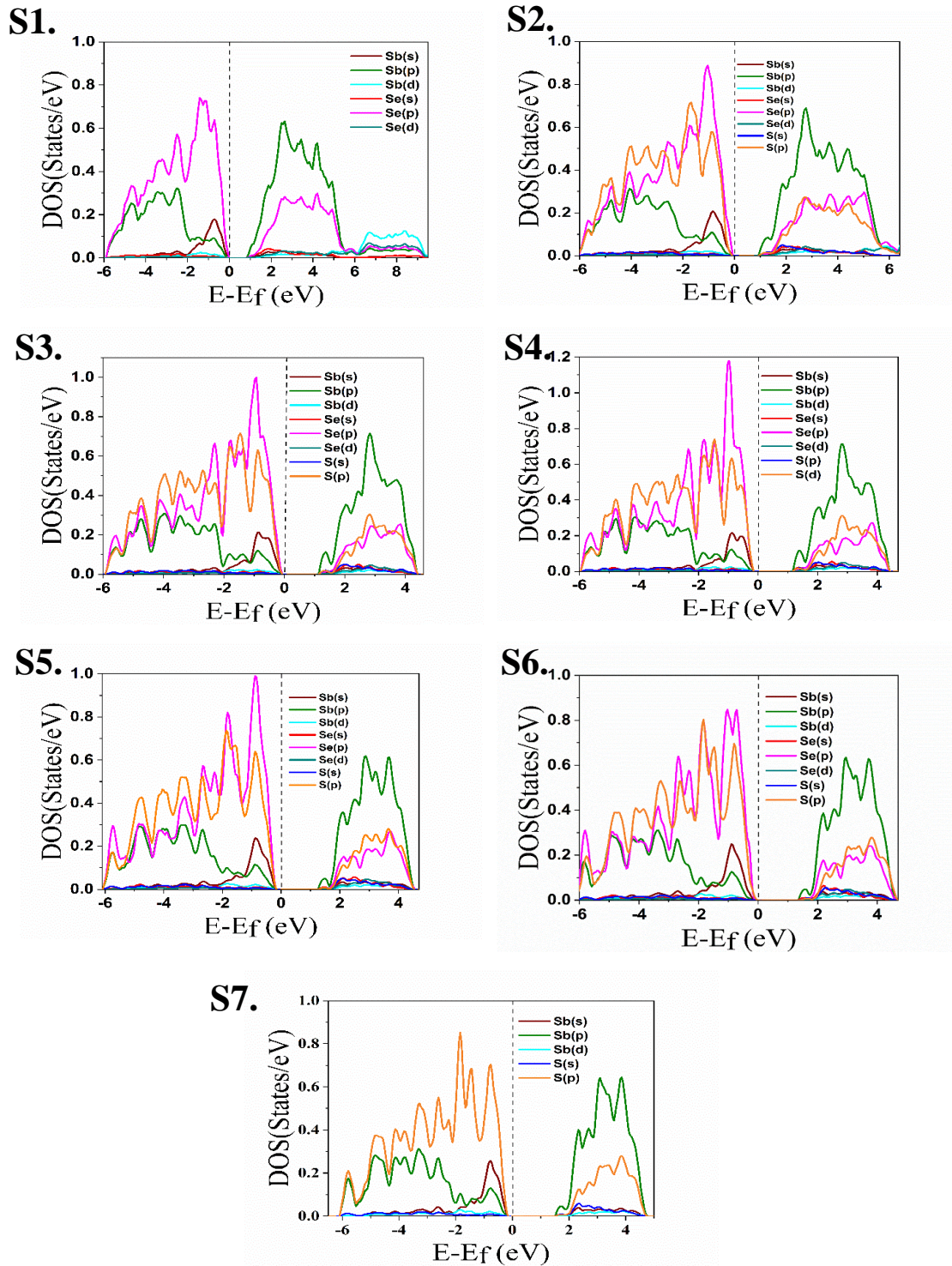


Figure 8.3: DOS of $\text{Sb}_2(\text{S}_x\text{Se}_{1-x})_3$ for $x =$ (S1) 0, (S2) 0.5, (S3) 0.6, (S4) 0.7, (S5) 0.8, (S6) 0.9, (S7) 1.0 using HSE06 functional

The change of DOS with the increase in S content was studied and shown in Figure 8.3 (S2) – (S6). Slight broadening in the peak was observed in the energy range $-6 - 0$ eV, which may be attributed to the covalence in the alloyed compounds ($\text{Sb}_2(\text{S}_x\text{Se}_{1-x})_3$),

and was consistent with the band gap calculation. The VB of S2-S6 was composed of Se-p, Sb-p, Sb-s & S-p, and the CB was made of Sb-p, S-p, and Se-p orbitals. Figure 8.3 shows that the VB of pure Sb_2S_3 is comprised of Sb-p, S-p, and S-p orbitals, while the CB is comprised of Sb(p) and S(p) states (S7).

From the above analysis, it was confirmed that there exists a graded band gap from 1.22 eV to 1.85 eV by changing the S content from 0 to 1 (0, 0.5, 0.6, 0.7, 0.8, 0.9, 1.0) in $\text{Sb}_2\text{S}_x\text{Se}_{1-x}$ samples. The aim of tuning the band gap was achieved, but all were indirect. In the case of indirect band gap material (for example, Si), the absorption coefficient is less, and to fabricate a solar cell few hundred micrometers will be required instead of 1 or 2 micrometers. The next aim is to search for a material with a direct band gap as CdTe. To achieve that, the structure which showed the indirect band gap of nearly 1.5 eV (same as the CdTe band gap) sample S4 was considered for further studies.

To begin with, the optimized structure of the S4 was obtained, depicted in Figure 8.1 (S4). Then, the (130) surface was constructed from the optimized structure, as (130) shows the minimum energy. Further, the unit cell structure of S4(130) was allowed to relax. Then the electronic properties of the system were studied by using the density functional theory. In this case, to get the accurate band gap, HSE06 functional was used. The optimized geometry, band structure, and DOS for the S4 (130) are depicted in Figure 8.4. The VB of the sample was composed of S-p, Se-p, whereas the CB was made up of Sb-p, Se-p, and Sb-s. As can be seen in the figure, the sample exhibited an intriguing direct band gap at the Gamma point of 1.80 eV. Whenever there is a change in the dimension of the system, i.e., from bulk to surface (3D to 2D), the density of states of the material changes. As the density of states fluctuates, the lowest occupied energy level may undergo a shift towards higher energies (or lower energies for holes), resulting in an increase in the gap. The magnitude of this shift is contingent on the effective mass, with a lower mass leading to a stronger shift. For instance, when the mass of the direct band is larger than the indirect band, then there is a possibility of energy states crossing. From the electronic properties calculation, it can be concluded that this S4 sample ($\text{Sb}_2(\text{S}_{0.7}\text{Se}_{0.3})_3$) (130) can be used as the absorber layer in solar cells for visible light absorption.

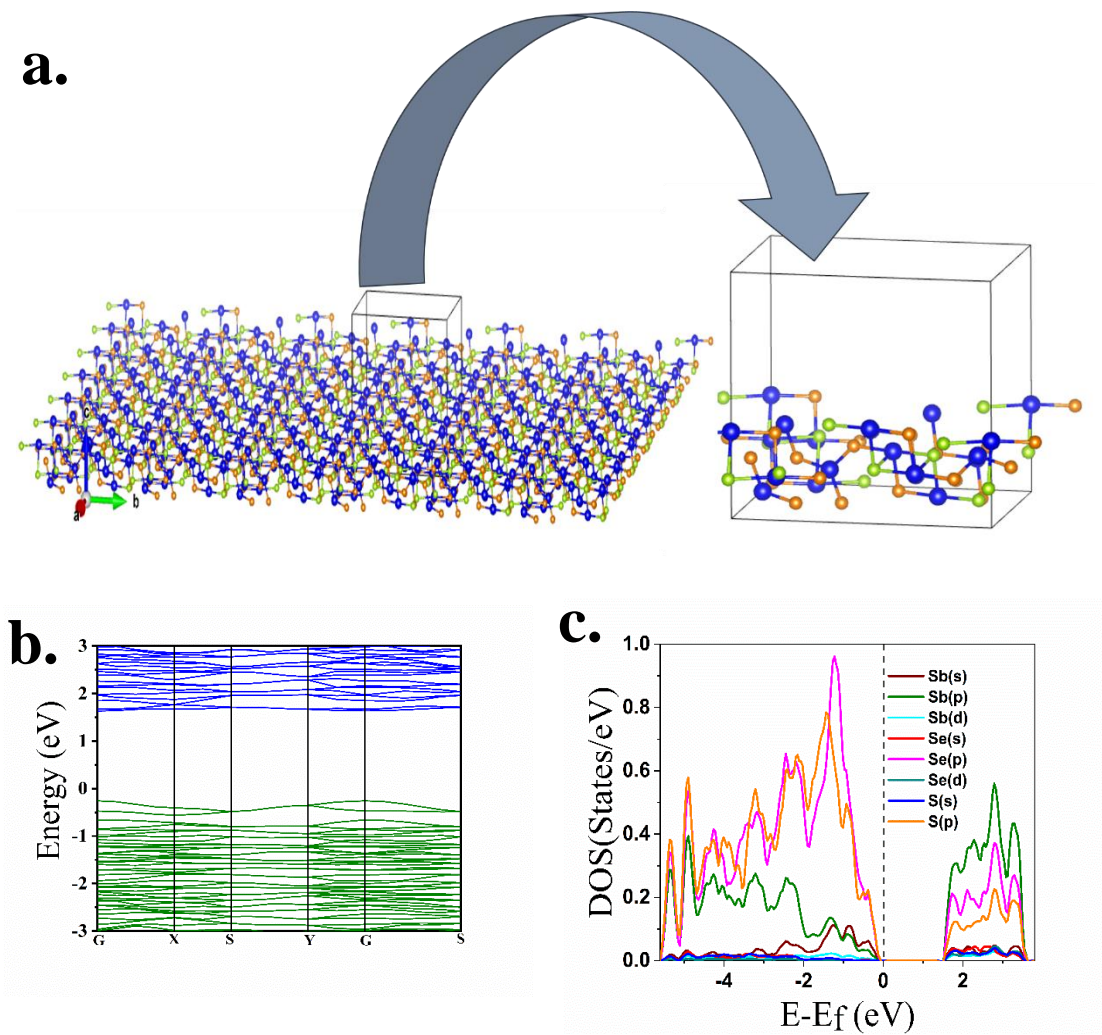


Figure 8.4: a. Optimized geometry, b. Band structure, and c. DOS of S4 using HSE06 functional.

8.3.3 Introduction to mxenes and S4(130)/mxenes interface:

It is widely recognized that MXenes possess exceptional conductivity. However, as demonstrated in Figure 8.5, a number of semiconducting MXenes have also been discovered. One of these is ScHfNNOH, a double transition metal MXene with a significant wide band gap. To confirm the structural stability of the recently predicted MXenes, an initial calculation of geometry optimization and the DOS was done and depicted in Figures 8.5 a and b. The optimized bond length Sc-N and Hf-N was 2.09 Å and 2.06 Å, respectively.

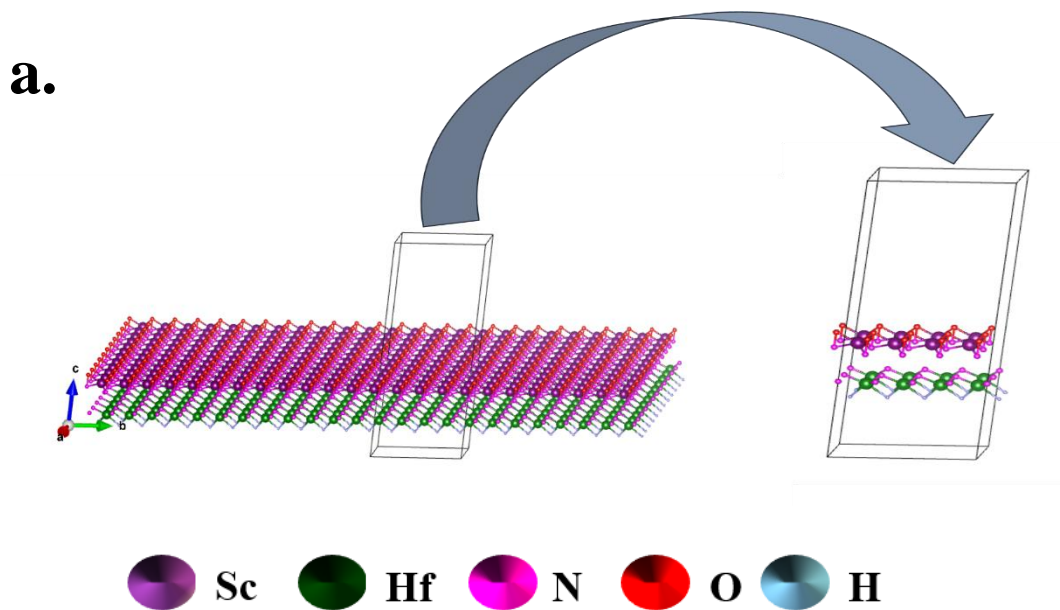


Figure 8.5: a. Optimized geometry of ScHfNNOH

DOS gives a deeper knowledge of the electronic properties of the materials. From Figure 8.5 b, it can be concluded that the VB of the Mxenes was made of Sc-d, Hf-d, N-p, and Sc-p orbitals, whereas the CB was mainly composed of Hf-d, Sc-d orbitals. Furthermore, the band structure of the proposed Mxenes was studied and depicted in Figure 8.5 c. The material possesses an indirect band gap of 2.11 and which was indirect.

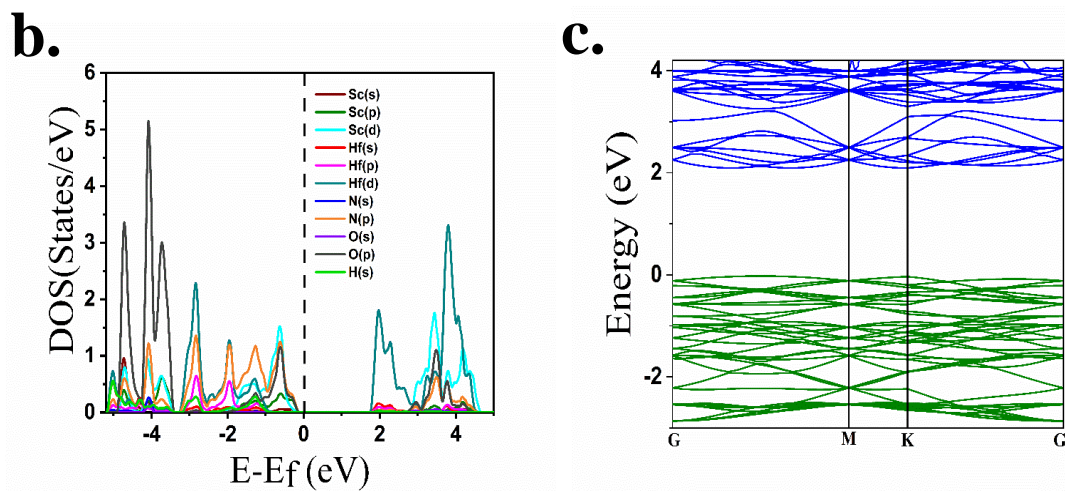


Figure 8.5: b and c: Electronic properties of ScHfNNOH

As this material is a wide band gap material, It can be used as the window or buffer layer in photovoltaic cells.

It is necessary to study the interface behavior to understand the material's applicability in solar cells. From the above discussion, it was observed that S4(130) is the potential candidate for the absorber layer in the solar cell. The interface was constructed by taking the S4 (130) along with the ScHfNNOH (2D mxenes) and introducing the vacuum in the z direction to restrict the interaction between the periodic images. Then the structure was allowed to attain the minimum energy, and the optimized geometry is shown in Figure 8.6 a. To gain a deeper insight into the electronic properties of the material, the DOS of the interface was studied and depicted in Figure 8.6 b. From this, it can be noted that the VBM was dominated by the Se-p orbitals. On the other hand, the CBM was composed of the Sb-p, S-p, and Hf-d orbitals. As can be seen in Figure 8.6 c, the interface exhibits an indirect band gap of 0.95 eV.

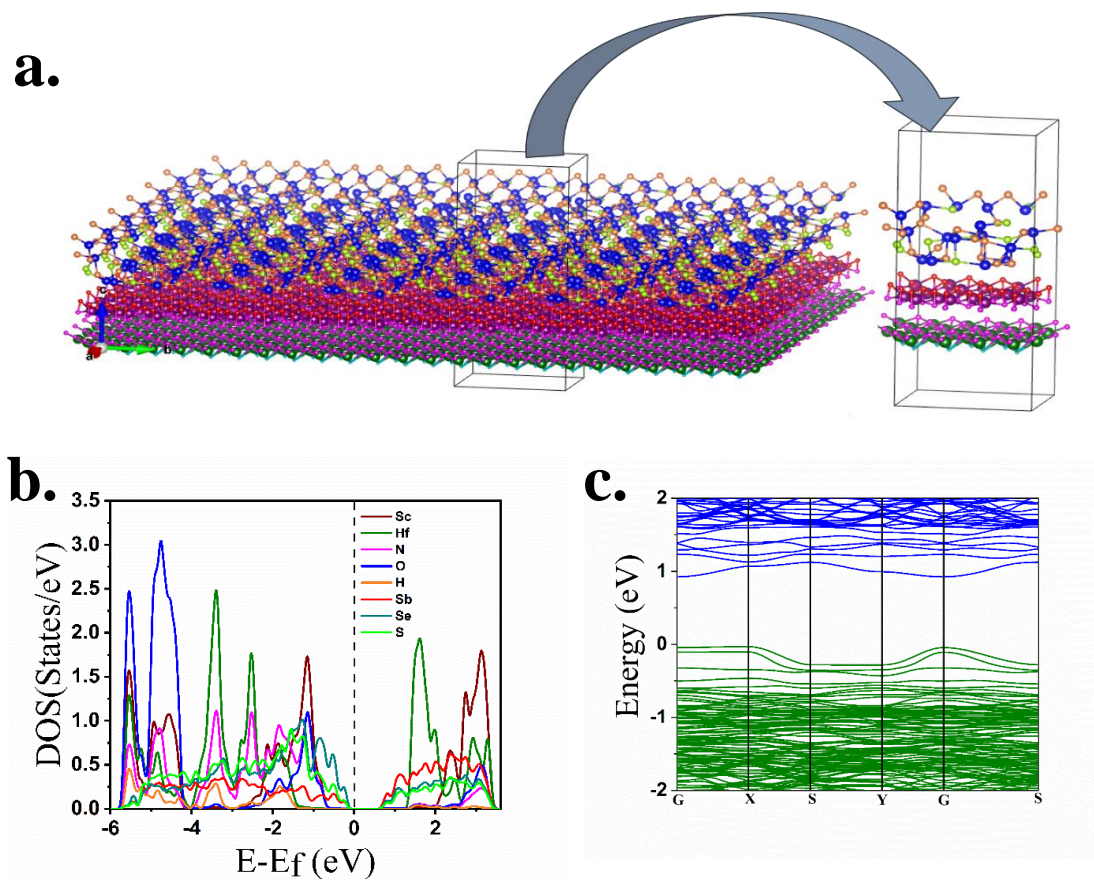


Figure 8.6: a. Optimized geometry of the heterostructure b, c. Electronic properties of the heterostructure.

Optical absorption was calculated to realize the application of these materials and their heterostructure. Linear response theory was used to calculate the absorbance of the S4 (130), Mxenes, and their heterostructure. The absorbance spectra of the samples are depicted in Figure 8.7. The optical absorption analysis found that the S4(130) sample can be used as the visible light absorption layer in the solar cells. The Mxenes, ScHfNNOH being the wide band gap semiconductor, can be used as the window layer, which this study introduced for the first time. The heterostructure showed the absorbance peak within the energy range of 1 eV to 3 eV, which indicates that it will absorb light from the UV- Visible to near IR regions of the solar spectrum. Moreover, these materials are suitable for the fabrication of solar cells.

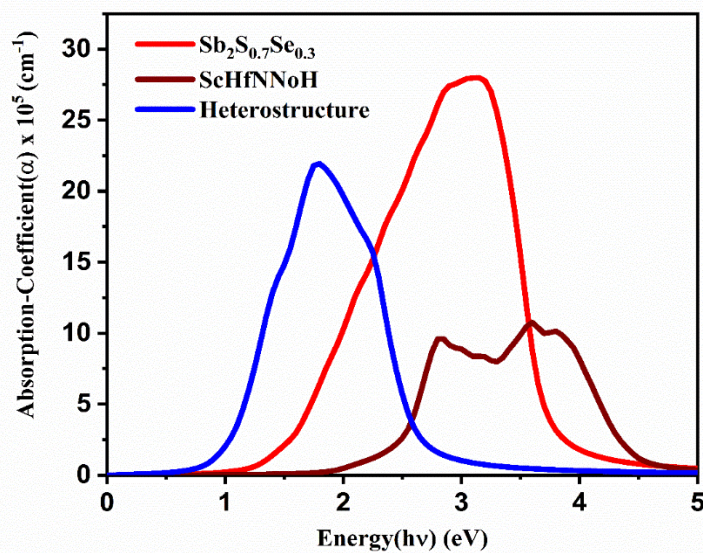


Figure 8.7: The optical absorbance spectra of S4 (130), mxenes, and their heterostructure were estimated using the DFT.

8.4 Summary:

The S alloyed Sb_2Se_3 was studied, and the sample $Sb_2(S_{0.7}Se_{0.3})_3$ can be used as the potential absorber layer in the solar cells in place of CdTe (as it is toxic in nature) as it possesses the direct band gap and nearly identical as the CdTe. It was reported for the first time that this specific S alloyed sample (130) surface has a direct band gap. Direct band gap materials are typically preferred because they only require the photon energy

to match the band gap energy without interacting with phonons. This enables the use of thinner PV cells with less absorbing material, resulting in a lighter weight. Then another essential 2D material, mxenes, ScHfNNOH, was introduced, and this material was also studied and reported for the first time, which showed the semiconducting behavior. This is a wide band gap mxenes and can be used as the window layer for the solar cells. Interestingly, the heterostructure showed an indirect band gap of 0.95 eV, which can absorb sunlight in a wide range of wavelengths near the IR region. In the future, many parameters related to the interface, such as carrier concentration, band bending, and the suitability of these materials in other applications, can be studied. Furthermore, the functional group can be changed and studied for the better performance of the solar cell in future studies.

CHAPTER 9

ZnS_xSe_{1-x} THIN FILMS: A STUDY INTO ITS TUNABLE ENERGY BAND GAP PROPERTY USING AN EXPERIMENTAL AND THEORETICAL APPROACH

Overview:

In Chapter 8, Sb₂ (S_xSe_{1-x})₃ /mxene was introduced in place of the CdTe absorber layer to make a Cd-free solar cell. CdS is generally used as the window layer in CdTe solar cells. The next step is to replace the CdS layer with another alloyed chalcogenide nanostructure, i.e., ZnS_xSe_{1-x}. Recently, ZnS and ZnSe thin films have been drawing tremendous attention towards optoelectrical devices due to their optimal wide band gap energy. By alloying ZnS and ZnSe films to obtain ZnS_xSe_{1-x} thin films, the band gap of the ZnS_xSe_{1-x} film can be tuned to a value according to the device's requirements. This chapter includes the deposition and characterization of the ZnS_xSe_{1-x} thin films by changing the x value, i.e., 0, 0.10, 0.25, 0.50, 0.75, 0.90, 1. Furthermore, the detailed theoretical analysis based on density functional theory calculation has also been provided.

9.1 Introduction:

In the current years, the II–VI compound semiconductors are extensively studied for thin film photovoltaics because of their attractive properties. In a thin film solar cell, the buffer layer enhances its overall cell efficiency. Among the various II–VI group members such as ZnSe, ZnS, and CdS, CdSe is generally favored due to its highest cell efficiency (Contreras et al. 2005). But because of its small optical band gap of ~ 2.42 eV, photons with energy more significant than its band gap get absorbed in the CdS layer (Ashraf et al. 2009). Moreover, the toxicity of CdS has driven research in finding Cd-free materials such as $\text{Zn}_{1-x}\text{Mg}_x\text{O}$, ZnTiO (Hwang et al. 2018), ZnS (Bhattacharya and Ramanathan 2004), ZnO, and ZnSe (Xin et al. 2016). Among these materials, ZnSe and ZnS are generally preferred due to their non-toxicity nature, wide band gap, and vast availability in the earth's crust. ZnS and ZnSe have a variety of applications, especially in heterojunction devices such as LEDs (Jin et al. 2018), lasers with short wavelengths (Vasilyev et al. 2016), and thin film electroluminescent devices (Lee et al. 2014). Both ZnS and ZnSe are n-type semiconductors and have a wider band gap than that of CdS. A variety of techniques are available to deposit ZnS and ZnSe thin films, such as chemical bath deposition (Bhattacharya et al. 2004; Lokhande et al. 1998), spray pyrolysis (Lohar et al. 2014; Zeng et al. 2013), sputtering (Shao et al. 2003; Yudar et al. 2017), thermal evaporation (Benyahia et al. 2015; Zedan et al. 2016), etc. As both these compounds have almost the same crystallographic structure (i.e., zinc blende and a variation of less than 5% in their lattice constants), therefore, it is relatively easier to form their alloys.

Recently, the preparation of the ternary alloy of $\text{ZnS}_x\text{Se}_{1-x}$ has gained much interest due to its tunable optical properties (Agawane et al. 2014). By alloying ZnS and ZnSe thin films, band gap modification of the $\text{ZnS}_x\text{Se}_{1-x}$ thin films is possible by modulating the composition, i.e., by varying the composition's, the band gap of the films can be altered, which can be useful for solar cell application. Numerous techniques like molecular beam epitaxy (MBE) (Shen et al. 2003), atomic layer epitaxy (ALE) (Song et al. 2000), selenisation (Agawane et al. 2014), chemical vapor transport (CVT) (Kannappan et al. 2013), spray pyrolysis (Patil et al. 2018), chemical vapor deposition (CBD) (Agawane et al. 2014), sputtering (Ganguly et al. 2001), and thermal

evaporation (Chuo et al. 2014) are available to deposit $\text{ZnS}_x\text{Se}_{1-x}$ films. Among these techniques, the thermal evaporation technique is quite a more straightforward method to grow high-quality films with good crystallinity and uniformity. Hence, in the present study, thin films of $\text{ZnS}_x\text{Se}_{1-x}$ ($x = 0, 0.10, 0.25, 0.50, 0.75, 0.90, 1$) were grown on well-cleaned glass substrates via vacuum thermal evaporation technique. The various properties of the obtained $\text{ZnS}_x\text{Se}_{1-x}$ thin films were then analyzed as a function of their compositions, 'x.' In addition, the Density Functional Theory (DFT) analysis was carried out on the proposed compositions using Vienna Ab-initio Simulation Package (VASP). The obtained properties of the films were then compared with their theoretical counterpart.

9.2 Methodology

9.2.1 Experimental details

The pristine ZnS, ZnSe, and their alloyed films with different compositions ($\text{ZnS}_x\text{Se}_{1-x}$) were deposited on pre-cleaned glass substrates using a thermal evaporation system. The substrate was placed at a vertical height of 13 cm from the evaporation source, and an average deposition rate of 20 nm/min was maintained throughout the deposition. A homogenous mixture of ZnS (99.995%, Sigma Aldrich) and ZnSe (99.999%, Alpha Aesar) powder was used to deposit the ternary thin films. During the deposition process, a substrate temperature of 373 K was fixed, and a vacuum pressure of 2×10^{-6} Torr was maintained. All the films were then subjected to annealing at 373 K for 60 mins duration and, thereby, leading to the formation of stoichiometric films. Using the gravimetric method, the films' thickness was determined and fixed at ~ 350 nm for the various compositions. An X-ray diffractometer (Rigaku MiniFlex 600) with Cu K_α radiation was employed to obtain the structural information of the thin films. The morphological studies of the films were determined by an FE-Scanning electron microscope (Carl Zeiss). The composition of the $\text{ZnS}_x\text{Se}_{1-x}$ thin films was determined using an energy dispersive spectroscopy (EDS) attached to the FE-SEM system by analyzing the emitted X-rays from the sample that occurred during the bombardment of an electron beam with the samples. The optical characteristics of the $\text{ZnS}_x\text{Se}_{1-x}$ films

were analyzed in the wavelength range of 330–800 nm by a double beam UV–Vis–NIR Spectrometer (UV-3600, Shimadzu).

9.2.2 Computational technique

The Density Functional Theory (DFT) calculation was employed to calculate the structural and electronic properties of binary and ternary compounds using the Projected Augment Wave (PAW) method implemented in the Vienna Ab-initio Simulation Package (VASP) (Blöchl 1994; Jung et al. 2006; Kresse and Furthmüller 1996b). To describe the exchange and correlation potential, a generalized gradient approximation (GGA) of the Perdew-Burke-Ernzerhof (PBE) scheme was utilized. A cut-off frequency of 500 eV was set for the expansion of the plane wave. The geometry optimization was carried out in each case by setting the convergence criteria to be 1×10^{-5} eV for energy and $0.01 \text{ eV } \text{Å}^{-1}$ for force. To accurately calculate the optical energy band gap of the various compositions, the hybrid DFT calculations were carried out using the Heyd-Scuseria-Ernzerhof (HSE 06) hybrid functional with 25% Hartree-Fock exchange energy contribution as PBE underestimates the bandgap due to the presence of Artificial Self Interaction (Perdew and Wang 2018). The optical properties were studied using the Quantum ATK (Smidstrup et al. 2020).

9.3 Results and Discussion

The interplanar spacing ‘d’ and lattice parameter ‘a’ of the thermally grown $\text{ZnS}_x\text{Se}_{1-x}$ films were calculated using the equation 2.4. The average crystallite size ‘D’ was estimated using equation 2.3. The X-ray diffractograms of thermally deposited $\text{ZnS}_x\text{Se}_{1-x}$ thin films are shown in Figure 9.1. All the films are found to be polycrystalline in nature and have a cubic (zinc blende) structure with a preferential orientation along the (1 1 1) plane. The diffraction peak at $2\theta = 27.11^\circ$ (Fig. 1a) can be attributed to undoped ZnSe (JCPDS no. 00-037-1463) films, whereas the peak at 28.50° can be assigned to pure ZnS (JCPDS no. 00-005-0566) films. No additional peak(s) corresponding to both ZnS and ZnSe phases was observed from the XRD diffractograms. From Figure 9.2, it can be observed that as the composition ‘x’ increases, the predominant (1 1 1) diffraction peak shifts towards higher 2θ values.

This confirms the incorporation of ‘S’ atoms into the ZnSe lattice and, thus, the formation of ternary $\text{ZnS}_x\text{Se}_{1-x}$ thin films. The various structural parameters calculated for the films are presented in Table 1. The decrease in ‘lattice constant’ and ‘interplanar spacing’ is due to dissimilar ionic radii of Se^{2-} (198 pm) and S^{2-} (184 pm). Therefore, as the sulfur content increases, the interplanar distance, as well as the lattice constant, decreases. The lattice constant and interplanar spacing parameters obtained for undoped ZnSe and ZnS thin films are similar to the reported JCPDS card data.

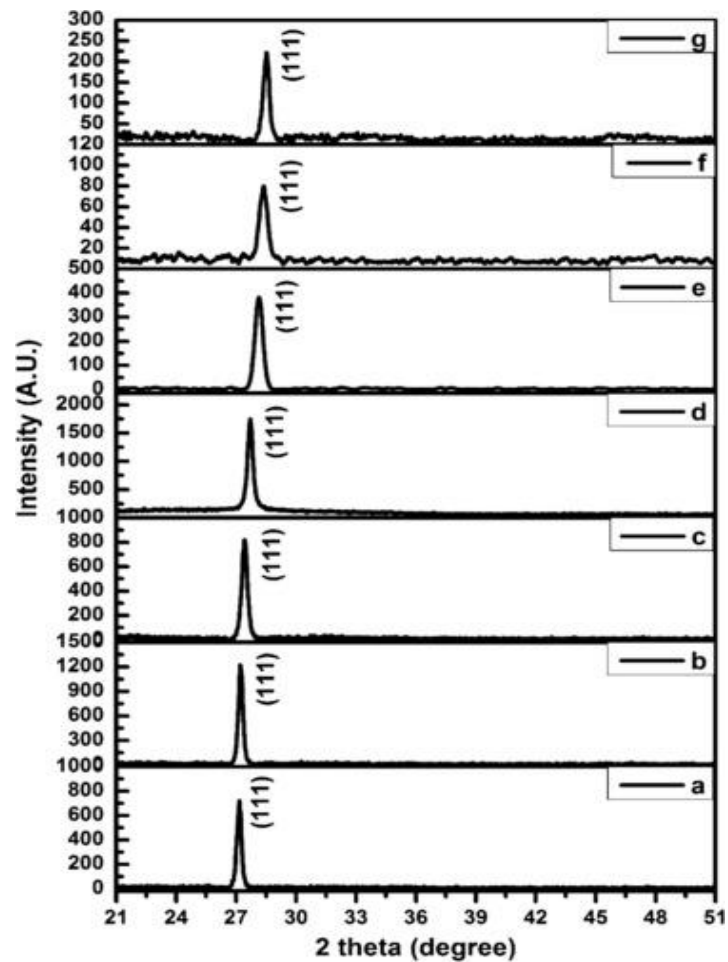


Fig. 9.1 XRD diffractograms of $\text{ZnS}_x\text{Se}_{1-x}$ films for $x =$ (a) 0, (b) 0.10, (c) 0.25, (d) 0.50, (e) 0.75, (f) 0.90, and (g) 1.

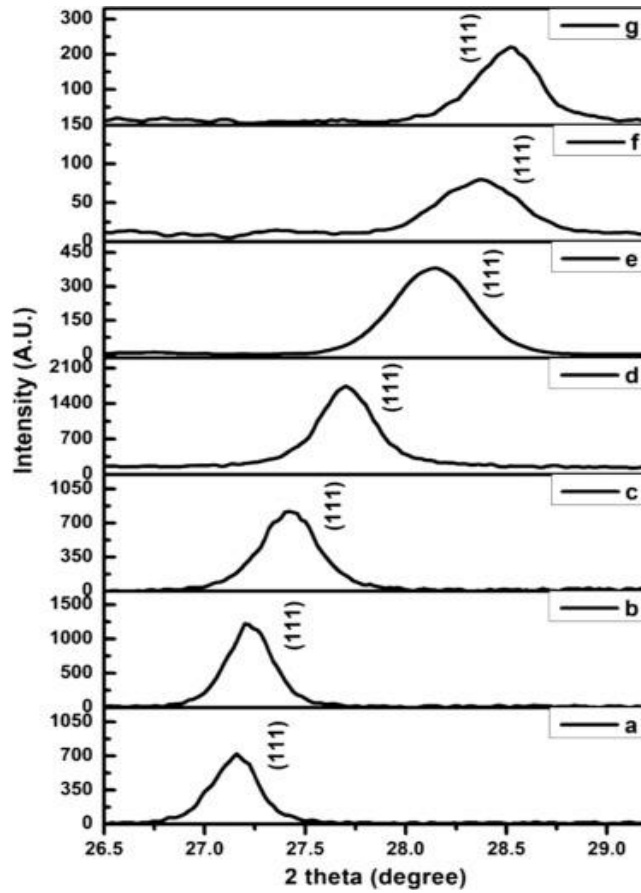


Fig. 9.2. Variation of the (1 1 1) peak position of the ZnS_xSe_{1-x} thin films for $x =$ (a) 0, (b) 0.10, (c) 0.25, (d) 0.50, (e) 0.75, (f) 0.90, and (g) 1.

Table 9. 1. Structural parameters of ZnS_xSe_{1-x} films.

Sample	Compositio n	2θ (degree)	Crystallite size, D (nm)	Interplanar spacing, d_{hkl} (Å)	Lattice constant, a (Å)
a	ZnSe	27.16	33.76	3.2806	5.6822
b	$ZnS_{0.10}Se_{0.90}$	27.20	29.98	3.2759	5.6740
c	$ZnS_{0.25}Se_{0.75}$	27.41	22.79	3.2513	5.6314
d	$ZnS_{0.50}Se_{0.50}$	27.69	28.70	3.2190	5.5755
e	$ZnS_{0.75}Se_{0.25}$	28.12	18.02	3.1708	5.4919
f	$ZnS_{0.90}Se_{0.10}$	28.37	19.92	3.1434	5.4445
g	ZnS	28.51	21.97	3.1283	5.4183

Using VASP, the geometry of the ZnS_xSe_{1-x} films was obtained, and the structural parameters were calculated and compared with the experimentally acquired data. The

optimized structures of pure ZnS, ZnSe, and their respective alloys are represented in Fig. 9.3. The energy-optimized ZnSe and ZnS exhibit zincblende structure with a lattice parameter of ‘a’ = 5.66 Å and 5.40 Å respectively, which is in good agreement with the experimental value.

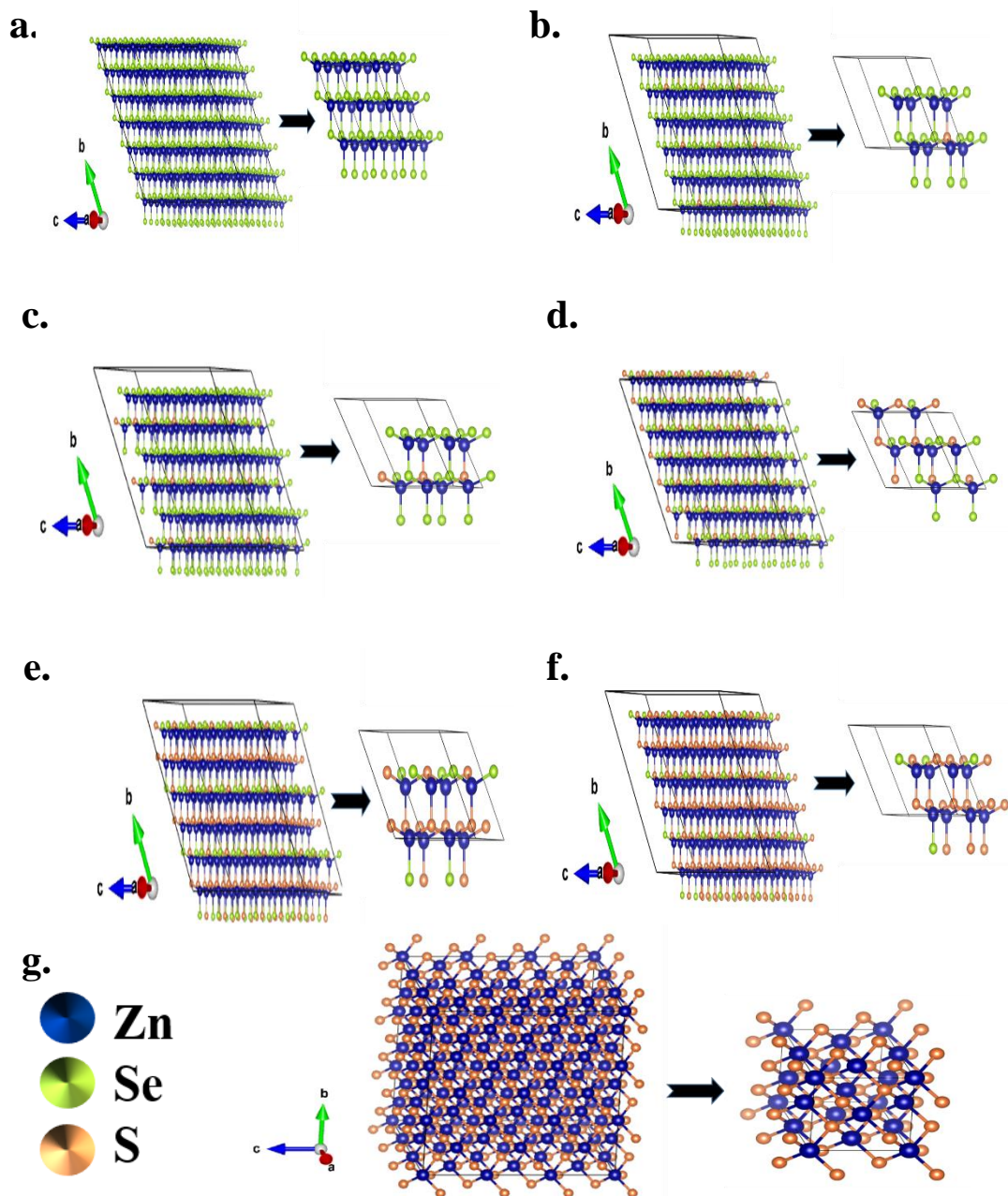


Fig. 9.3. Optimized geometry of $\text{ZnS}_x\text{Se}_{1-x}$ films for $x =$ (a) 0, (b) 0.10, (c) 0.25, (d) 0.50, (e) 0.75, (f) 0.90, and (g) 1.

The FE-SEM micrographs of the $\text{ZnS}_x\text{Se}_{1-x}$ thin films are displayed in Figure 9. 4. Even at 1 μm resolution, no cracks or pinholes are observed on the $\text{ZnS}_x\text{Se}_{1-x}$ films,

and all the films are uniformly deposited throughout a large area. In addition, it can also be noticed that sulfur incorporation changes the morphology of the films. Initially, at lower sulfur concentrations, the films tend to be granular, and as the composition ‘x’ increases, the granular features of the films disappear, as shown in Fig. 9.4 insets.

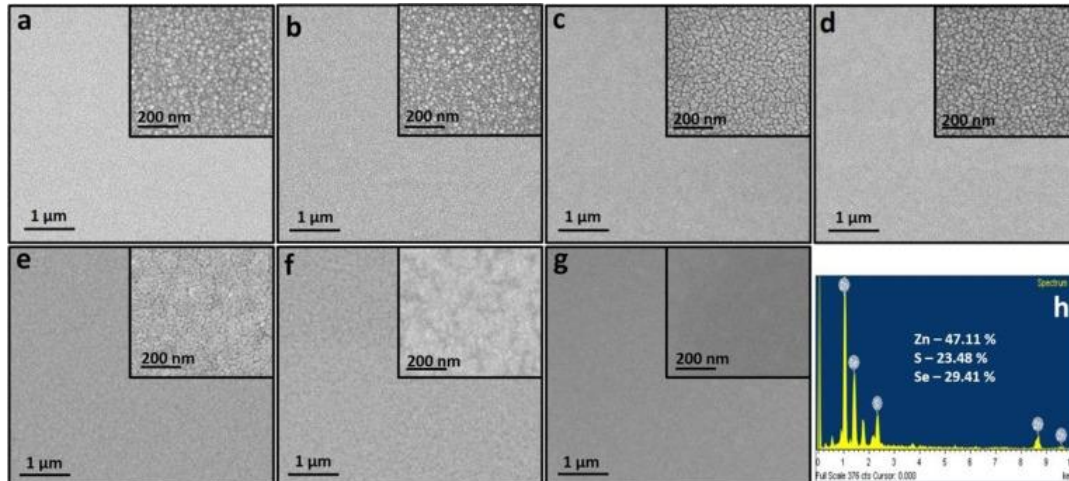


Fig. 9.4. FESEM images of $\text{ZnS}_x\text{Se}_{1-x}$ films for $x =$ (a) 0, (b) 0.10, (c) 0.25, (d) 0.50, (e) 0.75, (f) 0.90, and (g) 1.

The EDAX spectra associated with the $\text{ZnS}_{0.50}\text{Se}_{0.50}$ thin film is illustrated in Figure 9.4h, and the presence of Zn, S, and Se in respective quantity was verified. The various atomic composition of the films obtained from EDAX analysis is charted in Table 2. The obtained elemental composition of the films matches well with the expected values. The EDAX mapping of Zn, S, and Se elements of the $\text{ZnS}_{0.50}\text{Se}_{0.50}$ film is depicted in Figure 9.5, and it can be observed that all the elements are homogeneously distributed across the surface area, and no individual agglomeration of the elements was witnessed on the surface of the films.

Table 9.2. Composition and energy band gap of ZnS_xSe_{1-x} thin films.

Sample	Composition	Atomic percentage (%)			Band gap, E_g (eV)	Theoretical Band gap, E_{gt} (eV)
		Zn	S	Se		
a	ZnSe	48.81	–	51.19	2.59	2.28
b	$ZnS_{0.10}Se_{0.90}$	48.63	04.92	46.45	2.64	2.36
c	$ZnS_{0.25}Se_{0.75}$	48.02	12.37	39.61	2.73	2.38
d	$ZnS_{0.50}Se_{0.50}$	47.11	23.48	29.41	2.82	2.49
e	$ZnS_{0.75}Se_{0.25}$	47.68	36.50	15.82	3.04	2.77
f	$ZnS_{0.90}Se_{0.10}$	47.97	44.71	7.32	3.21	3.02
g	ZnS	51.14	48.86	–	3.38	3.28

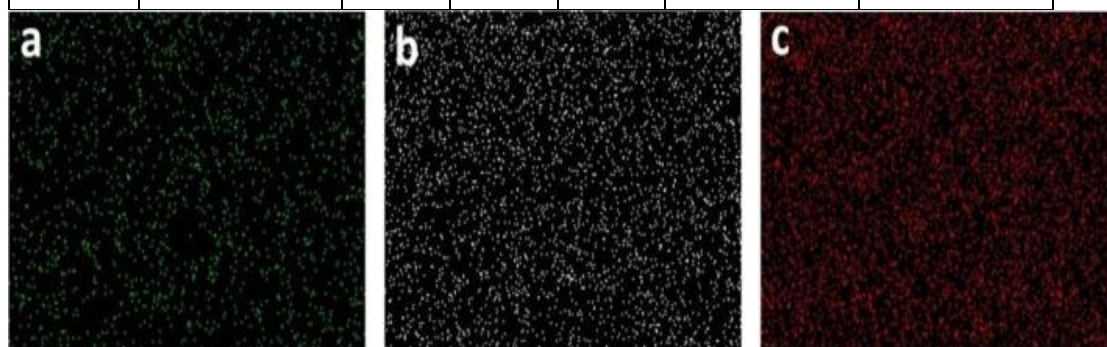


Figure 9.5. Elemental mapping images of $ZnS_{0.50}Se_{0.50}$ thin films (a) Zn, (b) S, and (c) Se.

To study the optical properties of the ZnS_xSe_{1-x} films, the optical transmittance and absorbance spectra of the films were determined in the wavelength range of 330–800 nm at room temperature. The transmittance spectra of the ZnS_xSe_{1-x} thin films are displayed in Figure 9.6. From the transmittance plot, it can be observed that the transmittance of the films increases with an increase in the sulfur content.

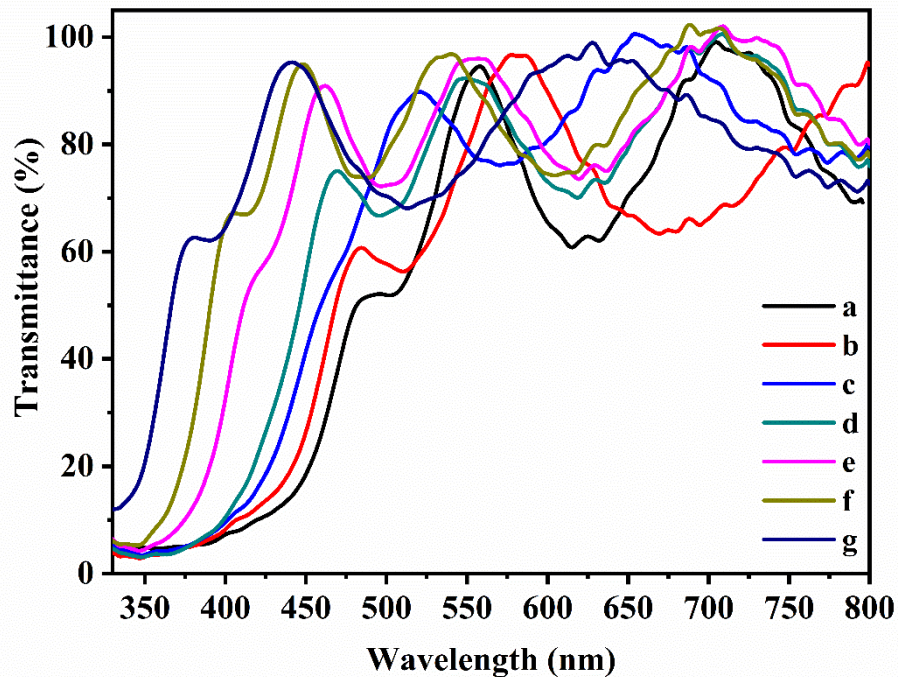


Fig. 9.6. Transmittance plot of $\text{ZnS}_x\text{S}_{1-x}$ films for $x =$ (a) 0, (b) 0.10, (c) 0.25, (d) 0.50, (e) 0.75, (f) 0.90, and (g) 1.

The band gap (E_g) of $\text{ZnS}_x\text{Se}_{1-x}$ thin films was obtained using Tauc's relation (Tauc 1972). Figure 9.7 depicts the variation of photon energy ($h\nu$) with $(\alpha h\nu)^2$. The linear extrapolation of the plot in Figure 9.7 to the intercept at $(\alpha h\nu)^2 = 0$ provides the optical band gap of the material. This verifies the occurrence of direct band gap transition for the thermally obtained $\text{ZnS}_x\text{Se}_{1-x}$ thin films. The band gap values obtained for $x = 0$ and $x = 1$ corresponds to that of undoped ZnSe and ZnS thin films (Barman et al. 2019; Kale and Lokhande 2004), respectively.

To understand the optical properties of $\text{ZnS}_x\text{Se}_{1-x}$ films via theoretical investigation, the band structure of pristine ZnSe, ZnS, and their alloys, as depicted in Figure 9.8, was studied. A direct band gap of 2.28 eV for ZnSe agrees well with the experimental value of 2.59 eV at the gamma point. Similarly, for pristine ZnS, the band gap of 3.28 eV at the gamma point agrees with the experimental value of 3.38 eV. The energy band gap values obtained using the proposed theoretical model are comparable to the experimentally obtained values, as mentioned in Table 9.2. The incorporation of S in ZnSe broadens the band gap of the semiconductor and thereby extends the light

absorption from the visible light region to UV territory leading to the potential application in optoelectronic devices (Kumar et al. 1998).

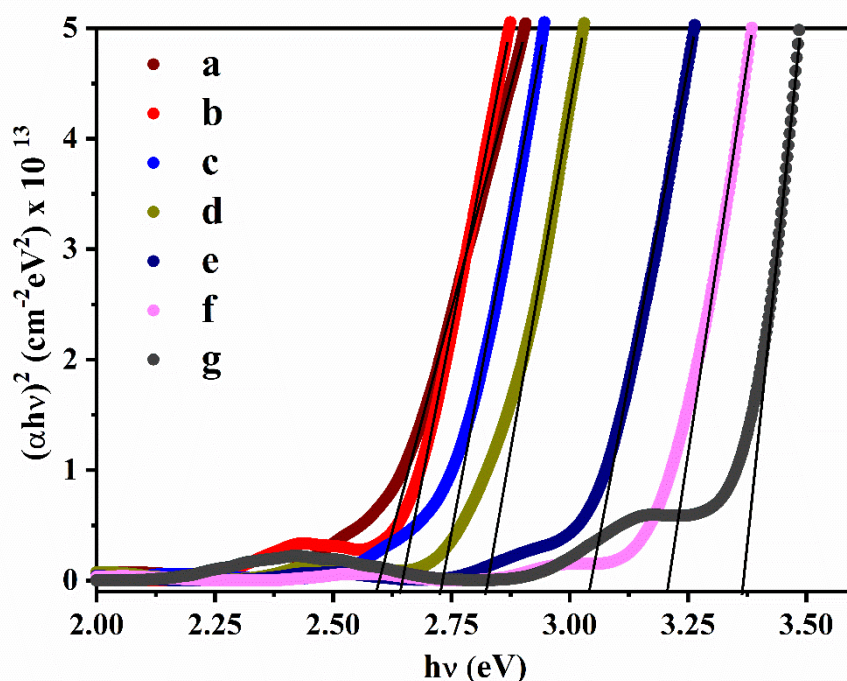


Figure 9.7. Tauc's plot of $\text{ZnS}_x\text{Se}_{1-x}$ films for $x =$ (a) 0, (b) 0.10, (c) 0.25, (d) 0.50, (e) 0.75, (f) 0.90, and (g) 1.

Further, to comprehend the orbital character at band edges, the atom-projected density of states is plotted for the $\text{ZnS}_x\text{Se}_{1-x}$ films, as shown in Figure 9.9. The valence band of ZnSe (figure 9.9a) offers the highest contribution of Zn 3p, Zn 3d, Zn 4s, and Se 4p states, whereas the conduction band comprised of Zn 4s, Zn 3p, Zn 3d, and Se 4p states. In the case of ZnS (Figure 9.9 g), the valence band is comprised of Zn 4s, Zn 3p, Zn 3d, and S 3p states, whereas the conduction band is of Zn 4s, Zn 3p, Zn 3d, S 3s, S 3p states. In the ternary system, the valence band shows the highest contribution from Zn 4s, Zn 3p, Zn 3d, S 3p, Se 4p states, and the conduction band from Zn 4s, Zn 3p, Zn 3d, S 3p, Se 4s, Se 4p states. The increase in band gap energy with increasing S concentration may be attributed to the decrease in peak from Se 4p states present in the valence band, as displayed in the DOS plot. The peak from S 3p state increases steadily with the increase in S concentration, while the Se 4p states peak decreases.

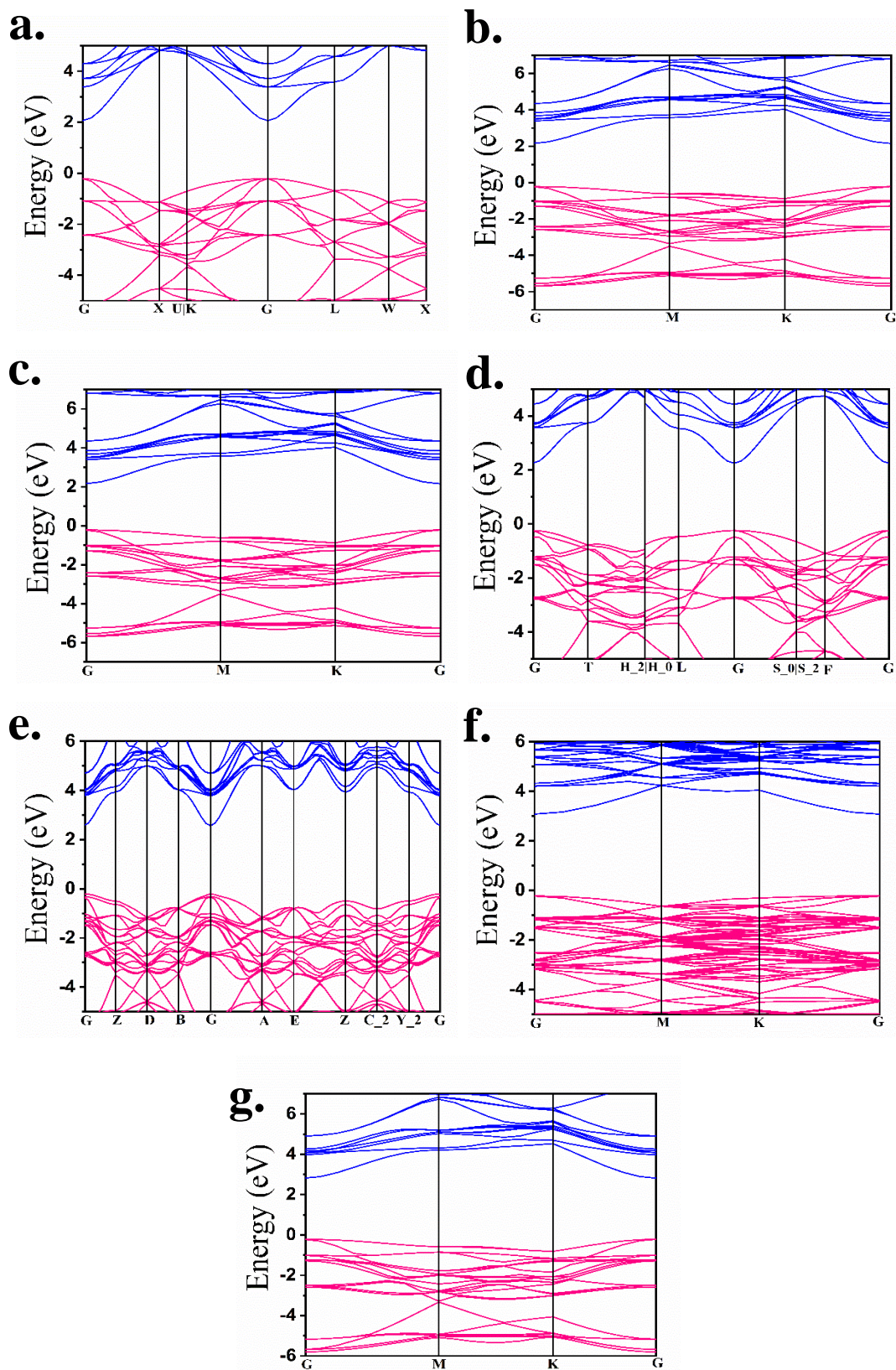


Figure 9.8. Calculated band structure of $\text{ZnS}_x\text{Se}_{1-x}$ thin films for $x =$ (a) 0, (b) 0.10, (c) 0.25, (d) 0.50, (e) 0.75, (f) 0.90, and (g) 1 using HSE06 functional

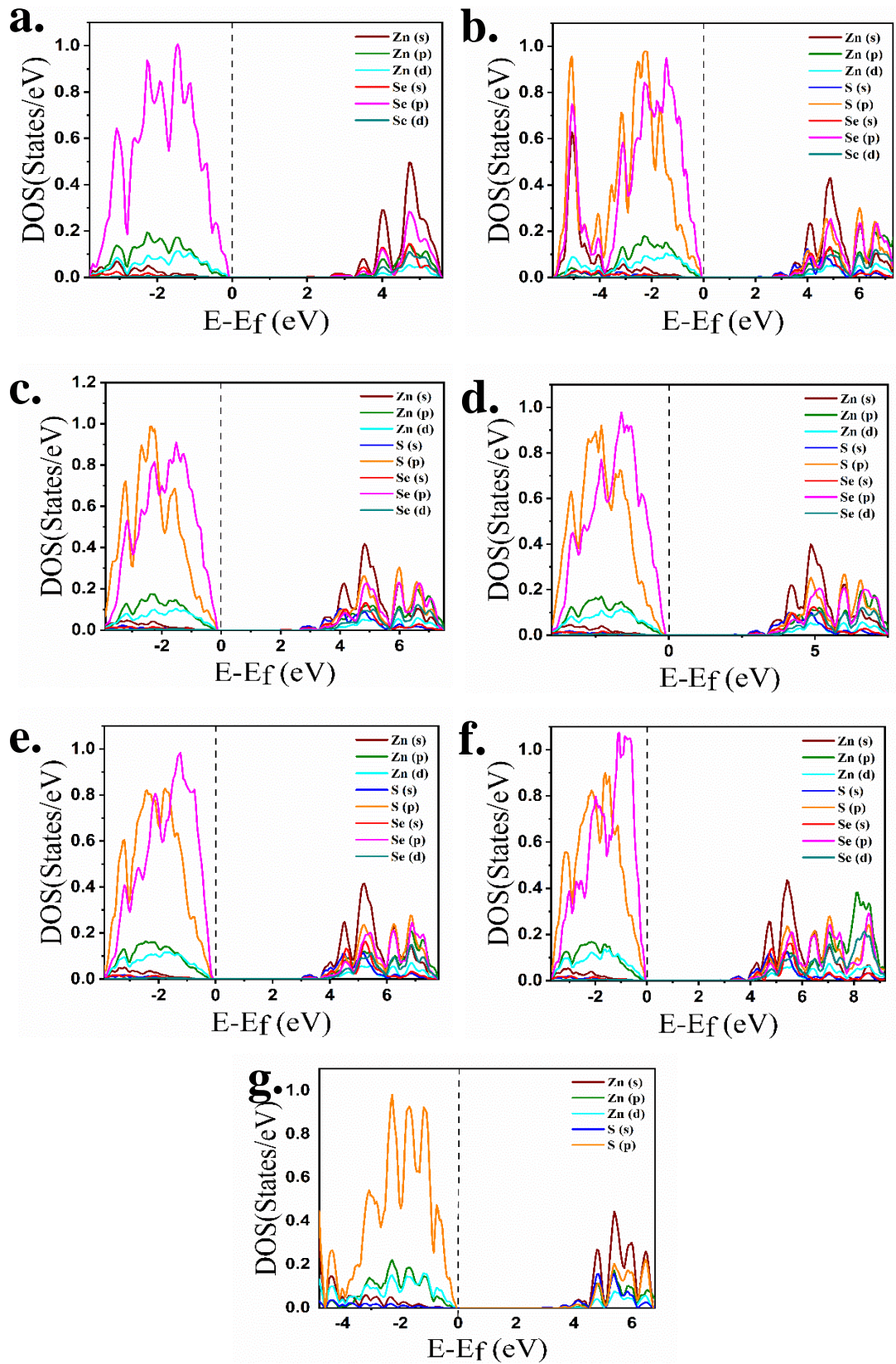


Figure 9.9. PDOS of ZnS_xSe_{1-x} thin films for x = (a) 0, (b) 0.10, (c) 0.25, (d) 0.50, (e) 0.75, (f) 0.90, and (g) 1

The absorbance spectra of all the structures were acquired using Quantum ATK and analyzed. The calculated result is illustrated in Figure 9.10. The presence of multiple peaks in the absorbance plot depicts the transition of electrons from the filled valence band to the empty conduction band of the ZnS_xSe_{1-x} films (Homann et al. 2006). The value of $\alpha(\omega)$ for ternary alloys increases gradually and shows the maximum absorption in the energy range of 3.0–4.0 eV, confirming the formation of ZnS_xSe_{1-x} alloy.

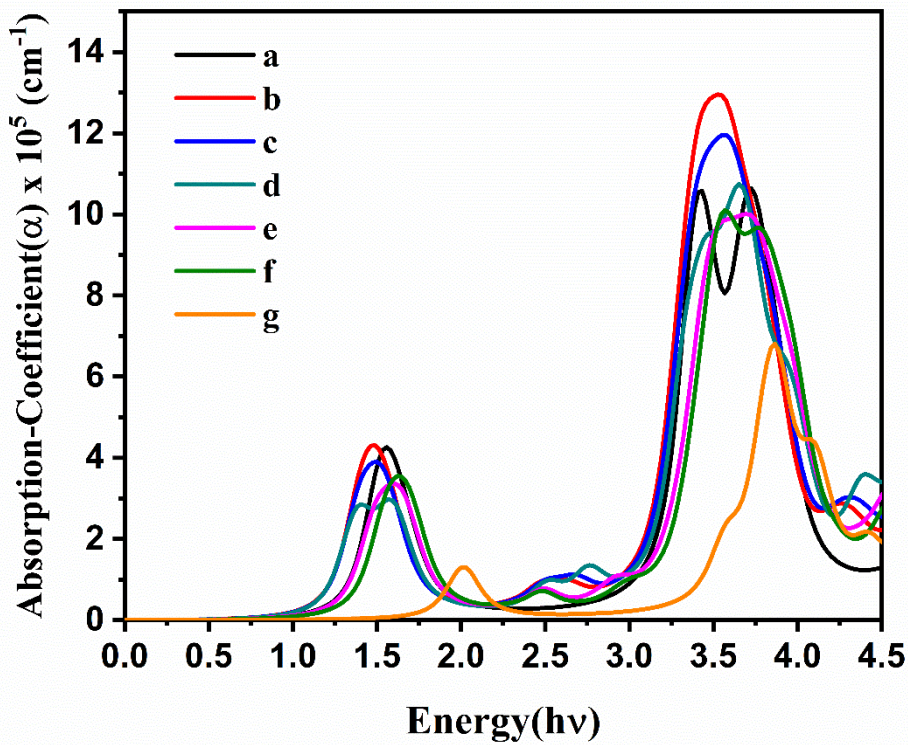


Figure 9.10. Theoretical absorption co-efficient of ZnS_xSe_{1-x} films for $x =$ (a) 0, (b) 0.10, (c) 0.25, (d) 0.50, (e) 0.75, (f) 0.90, and (g) 1.

Figure 9.11 depicts that the energy band gap of ZnS_xSe_{1-x} thin films varies non-linearly with the composition ‘x.’ The degree of the non-linear variation can be addressed by the below quadratic equation (Jana et al. 2007).

$$E_g(x) = a + bx + cx^2 \quad (9.1)$$

In the above equation, the parameter ‘b’ represents the characteristics of a particular alloy system known as the “bowing parameter” (Barman et al. 2020). A

polynomial fitting of the experimental energy band gap (E_g) and theoretical band gap (E_{gt}) values can be expressed as:

$$E_g(x) = 2.61 + 0.41x + 0.59x^2 \quad (9.2)$$

$$E_{gt}(x) = 2.33 + 0.21x + 1.13x^2 \quad (9.3)$$

The values of the bowing parameter reported in the present study are close to the reported values (Chuo et al. 2014; Homann et al. 2006). Similar non-linear variation in the optical band gap was also reported in $\text{Cd}_x\text{Zn}_{1-x}\text{S}$ and $\text{Cd}_x\text{Zn}_{1-x}\text{Se}$ alloy systems (Azizi et al. 2016)(Borse et al. 2007)(Sutrave et al. 2000). In addition, the experimental bowing parameter closely resembles the theoretical counterpart value.

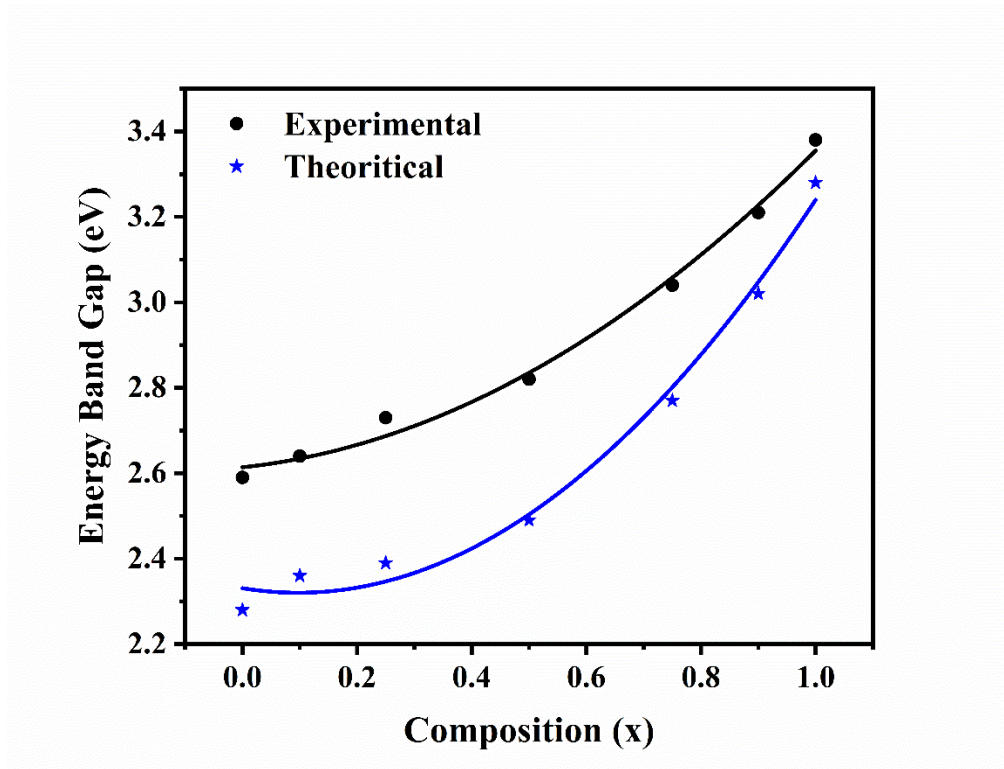


Figure 9.11. Variation of the energy band gap of $\text{ZnS}_x\text{Se}_{1-x}$ thin films with composition 'x.'

9.4: Summary:

A thermal evaporation technique was employed to deposit ternary $\text{ZnS}_x\text{Se}_{1-x}$ films on glass substrates successfully. The films were investigated using both experimental and theoretical approaches. The formation of $\text{ZnS}_x\text{Se}_{1-x}$ thin films was confirmed by XRD

analysis. The optimal geometry of the films was determined using VASP. The films were found to be polycrystalline and have a cubic structure with preferential orientation along the (1 1 1) plane. No pinholes or cracks were observed from the SEM studies. EDAX analysis confirmed the presence of Zn, S, and Se in appropriate quantities. Optical studies suggest that sulfur incorporation enhances the transmittance of the $\text{ZnS}_x\text{Se}_{1-x}$ films, i.e., more the sulfur concentration, the higher the transmittance in the visible wavelength region; this material can be used as the window layer in solar cells. The electronic structure of ZnS, ZnSe, and their alloys were investigated using the hybrid-DFT method. The contribution of different states in $\text{ZnS}_x\text{Se}_{1-x}$ was studied carefully. The band gap of the $\text{ZnS}_x\text{Se}_{1-x}$ films was tweaked from a value of 2.59 eV to 3.38 eV by altering the composition of the film and thereby, concluding a successful band gap engineering of the thermally evaporated $\text{ZnS}_x\text{Se}_{1-x}$ thin films.

CHAPTER 10

SUMMARY, CONCLUSION, AND FUTURE SCOPE OF THE WORK

Overview:

In this chapter, a succinct summary of the thesis is presented, along with an exploration of potential future directions for the work.

10.1 Summary of the work:

The thesis comprises nine comprehensive chapters covering a vast array of topics concerning thin films, compound semiconductors, and solar cells. Chapter 1 introduces these topics, including an in-depth literature survey, significant materials used in PV cells, and the extensive scope and objectives of the current work. Chapter 2 details the experimental techniques employed to deposit thin films and various methods for analyzing their properties. Chapter 3 presents a thorough discussion on the preparation and properties of CdTe thin films at different substrate temperatures, while Chapter 4 elucidates on ZnTe thin films. Furthermore, Chapter 5 thoroughly examines the preparation and properties of the p-ZnTe/n-CdTe heterostructure, while Chapter 6 focuses on potential BSF materials for CdTe solar cells. Chapter 7 delves deep into Cu-doped CdTe thin films and their properties, whereas Chapter 8 explores Cd-free absorber layers and Mxenes (2D materials). Finally, Chapter 9 conclusively describes the preparation and properties of a Cd-free window layer, ZnS_xSe_(1-x).

10.2 Conclusion:

- CdTe thin films prepared under ambient conditions showed increased absorption rates as substrate temperature increased. Higher temperatures also caused a switch from p-type to n-type conductivity, which could be helpful for solar cell applications.
- ZnTe thin films under ambient conditions were prepared, and found that the substrate temperature has an impact on the absorbance of the films. It is worth noting that ZnTe thin film has a wide band gap of 2.24 eV and shows consistent p-type conductivity, making it an attractive option for solar cell applications. This exciting discovery could lead to the development of sustainable energy solutions.
- The properties of the ZnTe/CdTe heterojunction were studied, and it was found that the interface is ideal for photovoltaic solar cells. Along with this, the theoretical calculations investigated the interface properties and found that using ZnTe as a back surface field layer in CdTe solar cells can improve efficiency and control recombination.

- The use of CdSe and ZnSe thin films as back surface field layers for CdTe solar cells was studied. Hybrid-DFT calculations showed that ZnSe/CdTe and CdSe/CdTe heterojunctions had improved light absorption behavior and created a local field that separates photo-generated electrons and holes, reducing recombination loss in the solar cells.
- CdTe and Cu-doped CdTe thin films were produced using PVD and analyzed with XRD, SEM, and EDAX methods. The optical properties of CdTe films were controllable, and Cu doping improved optical behavior. From the absorbance point of view, thin films using up to 3% Cu-doped CdTe thin film were recommended for highly efficient p-n junction solar cells.
- A study found $\text{Sb}_2(\text{S}_{0.7}\text{Se}_{0.3})_3$ to be a promising alternative to toxic CdTe for solar cells, with its direct band gap allowing for thinner, lighter PV cells. ScHfNNoH (Mxenes) was also studied for its semiconducting behavior and can serve as a window layer with a wide band gap. Further research can improve solar cell performance by exploring interface parameters and functional groups.
- $\text{ZnS}_x\text{Se}_{1-x}$ films were deposited on glass substrates using thermal evaporation. The films had a polycrystalline cubic structure and were suitable for solar cell window layers. The band gap values ranged from 2.59 eV to 3.38 eV, depending on the film composition. The electronic properties of all the samples were studied by using the DFT. Furthermore, the absorbance properties were studied.

10.3 Scope for future work:

The current highest laboratory cell efficiency record, held by NREL, has plateaued at 22%. The potential to increase current has been nearly exhausted, as challenges related to junction quality, CdTe properties, and contacts have proven more difficult to overcome. By comprehending the deterioration that certain CdTe devices experience at their contacts, the devices can be redesigned to mitigate this occurrence. Introducing the back surface field layer is one of the best ways to fix the problem. Extensive research on the 2D metal chalcogenide nanostructures was done and presented in this thesis. Apart from this, several other materials can also be explored in the context of the BSF layer.

Furthermore, both p-type and n-type CdTe thin films can be prepared by choosing the suitable dopant material. This investigation was carried out for Cu, and the conductivity was found to be p-type. The heterojunction can be fabricated with this doped layer, and the junction properties can be studied.

Finally, an attempt has been made to design the Cd-free solar cell absorber layer; S alloyed Sb_2Se_3 was introduced in this thesis. Nevertheless, there is an enormous scope to study the heterostructure's defect density, junction properties, and charge carrier dynamics. To our knowledge, the detailed study of junction properties of different layered materials associated with Sb_2Se_3 solar cells using first-principles calculations is yet to be done. Additionally, there is potential for exploring other 2D materials, such as Mxenes, for use in solar cell applications, beyond just $\text{Ti}_3\text{C}_2\text{T}_x$.

REFERENCES:

- A. Chikwenze, R. (2015). "Effect of Dip Time on the Structural and Optical Properties of Chemically Deposited CdSe Thin Films." *Int. J. Mater. Sci. Appl.*, 4(2), 101.
- Abd El-Raheem, M. M., Ali, H. M., and El-Husainy, N. M. (2009). "Optical and electrical measurements on electron beam evaporated CdTe thin films." *Optoelectron. Adv. Mater. Rapid Commun.*, 3(6), 533–538.
- Ablekim, T., Duenow, J. N., Zheng, X., Moutinho, H., Moseley, J., Perkins, C. L., Johnston, S. W., O'Keefe, P., Colegrove, E., Albin, D. S., Reese, M. O., and Metzger, W. K. (2020). "Thin-Film Solar Cells with 19% Efficiency by Thermal Evaporation of CdSe and CdTe." *ACS Energy Lett.*, 5(3), 892–896.
- Acharya, K. P., Erlacher, A., and Ullrich, B. (2007). "Optoelectronic properties of ZnTe/Si heterostructures formed by nanosecond laser deposition at different Nd:YAG laser lines." *Thin Solid Films*, 515(7–8), 4066–4069.
- Agawane, G. L., Shin, S. W., Vanalakar, S. A., Moholkar, A. V., Gurav, K. V., Suryawanshi, M. P., Lee, J. Y., Yun, J. H., and Kim, J. H. (2014). "Non-toxic novel route synthesis and characterization of nanocrystalline ZnS_xSe_{1-x} thin films with tunable band gap characteristics." *Mater. Res. Bull.*, 55, 106–113.
- AL-Oqla, F. M., and Fares, O. (2023). "Investigating the effect of green composite back sheet materials on solar panel output voltage harvesting for better sustainable energy performance." *Energy Harvest. Syst.*, 0(0).
- Albin, D. S., Yan, Y., and Al-Jassim, M. M. (2002). "The effect of oxygen on interface microstructure evolution in CdS/CdTe solar cells." *Prog. Photovoltaics Res. Appl.*, 10(5), 309–322.
- Amani-Ghadim, A. R., Mousavi, M., and Bayat, F. (2022). "Dysprosium doping in CdTe@CdS type II core/shell and cosensitizing with CdSe for photocurrent and efficiency enhancement in quantum dot sensitized solar cells." *J. Power Sources*, 539(January), 231624.
- Amin, N., Sopian, K., and Konagai, M. (2007a). "Numerical modeling of CdS/CdTe

and CdS/CdTe/ZnTe solar cells as a function of CdTe thickness.” *Sol. energy Mater. Sol. cells*, 91(13), 1202–1208.

Amin, N., Sopian, K., and Konagai, M. (2007b). “Numerical modeling of CdS/CdTe and CdS/CdTe/ZnTe solar cells as a function of CdTe thickness.” *Sol. Energy Mater. Sol. Cells*, 91(13), 1202–1208.

Amutha, R., Subbarayan, A., and Sathyamoorthy, R. (2006). “Influence of substrate temperature on microcrystalline structure and optical properties of ZnTe thin films.” *Cryst. Res. Technol.*, 41(12), 1174–1179.

Ashraf, M., Akhtar, S. M. J., Mehmood, M., and Qayyum, A. (2009). “Optical and structural properties of ZnS_xSe_{1-x} thin films deposited by thermal evaporation.” *Eur. Phys. J. - Appl. Phys.*, 48(1), 10501.

Azizi, S., Rezagholipour Dizaji, H., and Ehsani, M. H. (2016). “Structural and optical properties of $Cd_{1-x}Zn_xS$ ($x = 0, 0.4, 0.8$ and 1) thin films prepared using the precursor obtained from microwave irradiation processes.” *Optik (Stuttg.)*, 127(18), 7104–7114.

Bacaksiz, E., Aksu, S., Ozer, N., Tomakin, M., and Özçelik, A. (2009). “The influence of substrate temperature on the morphology, optical and electrical properties of thermal-evaporated ZnTe Thin Films.” *Appl. Surf. Sci.*, 256(5), 1566–1572.

Baciewicz, R. (1997). “Polycrystalline thin film solar cells.” *Opto-Electronics Rev.*, 1997(3), 167–173.

Bai, S., Guo, X., Zhang, X., Zhao, X., and Yang, H. (2021). “ Ti_3C_2Tx MXene - AgNW composite flexible transparent conductive films for EMI shielding.” *Compos. Part A Appl. Sci. Manuf.*, 149(July), 106545.

Barman, B., Bangera, K. V., and Shivakumar, G. K. (2019). “Preparation of thermally deposited $Cu_x(ZnS)_{1-x}$ thin films for opto-electronic devices.” *J. Alloys Compd.*, 772, 532–536.

Barman, B., Bangera, K. V., and Shivakumar, G. K. (2020). “ $Zn_xSn_{1-x}S$ thin films: A study on its tunable opto-electrical properties for application towards a high efficient photodetector.” *Sol. Energy*, 206(May), 479–486.

- Bätzner, D. L., Wendt, R., Romeo, A., Zogg, H., and Tiwari, A. N. (2000). “Study of the back contacts on CdTe/CdS solar cells.” *Thin Solid Films*, 361, 463–467.
- Benabbas, S., Rouabah, Z., Bouarissa, N., and Chelali, N. (2016). “The role of back surface field SnS layer in improvement of efficiency of CdTe thin film solar cells.” *Optik (Stuttg.)*, 127(15), 6210–6217.
- Benyahia, K., Benhaya, A., and Aida, M. S. (2015). “ZnS thin films deposition by thermal evaporation for photovoltaic applications.” *J. Semicond.*, 36(10), 2–6.
- Bhattacharya, R. N., Contreras, M. A., and Teeter, G. (2004). “18.5% Copper indium gallium diselenide (CIGS) device using single-layer, chemical-bath-deposited ZnS(O,OH).” *Japanese J. Appl. Physics, Part 2 Lett.*, 43(11 B).
- Bhattacharya, R. N., and Ramanathan, K. (2004). “Cu(In,Ga)Se₂ thin film solar cells with buffer layer alternative to CdS.” *Sol. Energy*, 77(6), 679–683.
- Birkmire, R. W., and McCandless, B. E. (2010). “CdTe thin film technology: Leading thin film PV into the future.” *Curr. Opin. Solid State Mater. Sci.*, 14(6), 139–142.
- Blaha, P., Schwarz, K., Tran, F., Laskowski, R., Madsen, G. K. H., and Marks, L. D. (2020). “WIEN2k: An APW+lo program for calculating the properties of solids.” *J. Chem. Phys.*, 152(7).
- Blöchl, P. E. (1994). “Projector augmented-wave method.” *Phys. Rev. B*, 50(24), 17953–17979.
- Bonnet, D. (2000). “Manufacturing of CSS CdTe solar cells.” *Thin Solid Films*, 361, 547–552.
- Borse, S. V., Chavhan, S. D., and Sharma, R. (2007). “Growth, structural and optical properties of Cd_{1-x}Zn_xS alloy thin films grown by solution growth technique (SGT).” *J. Alloys Compd.*, 436(1–2), 407–414.
- Bouroushian, M., Kosanovic, T., Karoussos, D., and Spyrellis, N. (2009). “Electrodeposition of polycrystalline ZnTe from simple and citrate-complexed acidic aqueous solutions.” *Electrochim. Acta*, 54(9), 2522–2528.
- Bozzini, B., Baker, M. A., Cavallotti, P. L., Cerri, E., and Lenardi, C. (2000). “Electrodeposition of ZnTe for photovoltaic cells.” *Thin Solid Films*, 361, 388–395.

- Britt, J., and Ferekides, C. (1993a). “Thin-film CdS/CdTe solar cell with 15.8% efficiency.” *Appl. Phys. Lett.*, 62(22), 2851–2852.
- Britt, J., and Ferekides, C. (1993b). “Thin-film CdS/CdTe solar cell with 15.8% efficiency.” *Appl. Phys. Lett.*, 62(22), 2851–2852.
- Brus, V. V., Solovan, M. N., Mastruk, E. V., Kozyarskii, I. P., Maryanchuk, P. D., Ulyanytsky, K. S., and Rappich, J. (2014). “Specific features of the optical and electrical properties of polycrystalline CdTe films grown by the thermal evaporation method.” *Phys. Solid State*, 56(10), 1947–1951.
- Cao, Y. L., Liu, Z. T., Chen, L. M., Tang, Y. B., Luo, L. B., Jie, J. S., Zhang, W. J., Lee, S. T., and Lee, C. S. (2011). “Single-crystalline ZnTe nanowires for application as high-performance Green/Ultraviolet photodetector.” *Opt. Express*, 19(7), 6100.
- Caracas, R., and Gonze, X. (2005). “First-principles study of the electronic properties of A₂B₃ minerals, with A=Bi,Sb and B=S,Se.” *Phys. Chem. Miner.*, 32(4), 295–300.
- Carey, J. J., Allen, J. P., Scanlon, D. O., and Watson, G. W. (2014). “The electronic structure of the antimony chalcogenide series: Prospects for optoelectronic applications.” *J. Solid State Chem.*, 213, 116–125.
- Çetinkaya, Ç., Çokduygular, E., Kınacı, B., Güzelçimen, F., Özen, Y., Sönmez, N. A., and Özçelik, S. (2022). “Highly improved light harvesting and photovoltaic performance in CdTe solar cell with functional designed 1D-photonic crystal via light management engineering.” *Sci. Rep.*, 12(1), 1–12.
- Chander, S., and Dhaka, M. S. (2016). “Impact of thermal annealing on physical properties of vacuum evaporated polycrystalline CdTe thin films for solar cell applications.” *Phys. E Low-Dimensional Syst. Nanostructures*, 80, 62–68.
- Chapman, A. J., Lane, D. W., Rogers, K. D., and Özsan, M. E. (2002). “Microstructural changes of CdTe during the annealing process.” *Thin Solid Films*, 403–404, 522–525.
- Chaure, N. B., Samantilleke, A. P., and Dharmadasa, I. M. (2003). “The effects of inclusion of iodine in CdTe thin films on material properties and solar cell performance.” *Sol. Energy Mater. Sol. Cells*, 77(3), 303–317.

- Chen, C., Bobela, D. C., Yang, Y., Lu, S., Zeng, K., Ge, C., Yang, B., Gao, L., Zhao, Y., Beard, M. C., and Tang, J. (2017a). “Characterization of basic physical properties of Sb₂Se₃ and its relevance for photovoltaics.” *Front. Optoelectron.*, 10(1), 18–30.
- Chen, C., Li, W., Zhou, Y., Chen, C., Luo, M., Liu, X., Zeng, K., Yang, B., Zhang, C., Han, J., and Tang, J. (2015). “Optical properties of amorphous and polycrystalline Sb₂Se₃ thin films prepared by thermal evaporation.” *Appl. Phys. Lett.*, 107(4).
- Chen, C., Wang, L., Gao, L., Nam, D., Li, D., Li, K., Zhao, Y., Ge, C., Cheong, H., Liu, H., Song, H., and Tang, J. (2017b). “6.5% Certified Efficiency Sb₂Se₃ Solar Cells Using PbS Colloidal Quantum Dot Film as Hole-Transporting Layer.” *ACS Energy Lett.*, 2(9), 2125–2132.
- Chopra, K. L., and Das, S. R. (1983). “Properties of Thin Films for Solar Cells.” *Thin Film Sol. Cells*, 275–347.
- Chou, R. L., Lin, M. S., and Chou, K. Sen. (1986). “Characteristics of CdTe grown on Si by low pressure metalorganic chemical vapor deposition.” *Appl. Phys. Lett.*, 48(8), 523–525.
- Chu, T. L. (1988). “Thin film cadmium telluride solar cells by two chemical vapor deposition techniques.” *Sol. Cells*, 23(1–2), 31–48.
- Chuo, H. X., Wang, T. Y., and Zhang, W. G. (2014). “Optical properties of Zn_xSe_{1-x} alloy nanostructures and their photodetectors.” *J. Alloys Compd.*, 606, 231–235.
- Compaan, A. D., Gupta, A., Lee, S., Wang, S., and Drayton, J. (2004). “High efficiency, magnetron sputtered CdS/CdTe solar cells.” *Sol. Energy*, 77(6), 815–822.
- Contreras, M. A., Ramanathan, K., Abushama, J., Hasoon, F., Young, D. L., Egaas, B., and Noufi, R. (2005). “Diode characteristics in state-of-the-art ZnO/CdS/ Cu(In_{1-x}Ga_x)Se₂ solar cells.” *Prog. Photovoltaics Res. Appl.*, 13(3), 209–216.
- Corwine, C. R., Pudov, A. O., Gloeckler, M., Demtsu, S. H., and Sites, J. R. (2004). “Copper inclusion and migration from the back contact in CdTe solar cells.” *Sol. Energy Mater. Sol. Cells*, 82(4), 481–489.
- Cusano, D. A. (1963). “CdTe solar cells and photovoltaic heterojunctions in II-VI compounds.” *Solid State Electron.*, 6(3), 217–232.

Desnica, U. V. (1998). "DOPING LIMITS IN II-VI COMPOUNDS - CHALLENGES, PROBLEMS AND SOLUTIONS." 36(4), 291–357.

Dey, D. M., Dey, M., Matin, M. A., and Amin, N. (2017). "High efficient and stable ultra-thin cdte solar cell with a potential copper telluride BSF." *Proc. 9th Int. Conf. Electr. Comput. Eng. ICECE 2016*, 590–593.

Dharmadasa, I. M., Bingham, P. A., Echendu, O. K., Salim, H. I., Druffel, T., Dharmadasa, R., Sumanasekera, G. U., Dharmasena, R. R., Dergacheva, M. B., Mit, K. A., Urazov, K. A., Bowen, L., Walls, M., and Abbas, A. (2014). "Fabrication of CdS/CdTe-based thin film solar cells using an electrochemical technique." *Coatings*, 4(3), 380–415.

Di, T., Xu, Q., Ho, W. K., Tang, H., Xiang, Q., and Yu, J. (2019). "Review on Metal Sulphide-based Z-scheme Photocatalysts." *ChemCatChem*, 11(5), 1394–1411.

Dobson, K. D., Visoly-Fisher, I., Hodes, G., and Cahen, D. (2000). "Stability of CdTe/CdS thin-film solar cells." *Sol. Energy Mater. Sol. Cells*, 62(3), 295–325.

Du, Y. T., Kan, X., Yang, F., Gan, L. Y., and Schwingenschlögl, U. (2018). "MXene/Graphene Heterostructures as High-Performance Electrodes for Li-Ion Batteries." *ACS Appl. Mater. Interfaces*, 10(38), 32867–32873.

Dudarev, S., and Botton, G. (1998). "Electron-energy-loss spectra and the structural stability of nickel oxide: An LSDA+U study." *Phys. Rev. B - Condens. Matter Mater. Phys.*, 57(3), 1505–1509.

Duffy, N. W., Peter, L. M., Wang, R. L., Lane, D. W., and Rogers, K. D. (2000). "Electrodeposition and characterization of CdTe films for solar cell applications." *Electrochim. Acta*, 45(20), 3355–3365.

Dzhafarov, T. D., Yesilkaya, S. S., Canli, N. Y., and Caliskan, M. (2005). "Diffusion and influence of Cu on properties of CdTe thin films and CdTe/ CdS cells." *Sol. Energy Mater. Sol. Cells*, 85(3), 371–383.

Edwards, P. R., Galloway, S. A., and Durose, K. (2000). "EBIC and luminescence mapping of CdTe / CdS solar cells." 362, 364–370.

Ernst, K., Engelhardt, R., Ellmer, K., Kelch, C., Muffler, H. J., Lux-Steiner, M. C.,

- and Könenkamp, R. (2001). "Contacts to a solar cell with extremely thin CdTe absorber." *Thin Solid Films*, 387(1–2), 26–28.
- Farrow, R. F. C., Jones, G. R., Williams, G. M., and Young, I. M. (1981). "Molecular beam epitaxial growth of high structural perfection, heteroepitaxial CdTe films on InSb (001)." *Appl. Phys. Lett.*, 39(12), 954–956.
- Fauzi, F., Diso, D. G., Echendu, O. K., Patel, V., Purandare, Y., Burton, R., and Dharmadasa, I. M. (2013). "Development of ZnTe layers using an electrochemical technique for applications in thin-film solar cells." *Semicond. Sci. Technol.*, 28(4).
- Feng, Z. C., Chou, H. C., Rohatgi, A., Lim, G. K., Wee, A. T. S., and Tan, K. L. (n.d.). "Correlations between CdTe/CdS/SnO₂/glass solar cell performance and the interface/surface properties." *Scopus*.
- Ferekides, C., Britt, J., Ma, Y., and Killian, L. (1993). "High efficiency CdTe solar cells by close spaced sublimation." *Conf. Rec. IEEE Photovolt. Spec. Conf.*, 389–393.
- Ferekides, C. S., Marinskiy, D., Viswanathan, V., Tetali, B., Palekis, V., Selvaraj, P., and Morel, D. L. (2000). "High efficiency CSS CdTe solar cells." *Thin Solid Films*, 361, 520–526.
- Fermi, E. (1927). "A statistical method for determining some properties of the atom. I." *Atti della Accad. Naz. dei Lincei, Cl. di Sci. Fis. Mat. e Nat. Rend.*, 6(December), 602–607.
- Filip, M. R., Patrick, C. E., and Giustino, F. (2013). "GW quasiparticle band structures of stibnite, antimonselite, bismuthinite, and guanajuatite." *Phys. Rev. B - Condens. Matter Mater. Phys.*, 87(20), 1–11.
- Fleming, A. J., Surnev, S., and Netzer, F. P. (2007). "Atomic force microscopy and photoemission electron microscopy study of the low-pressure oxidation of transition metal nitrides." *J. Appl. Phys.*, 102(8).
- Fock, V. (1930). "Näherungsmethode zur Lösung des quantenmechanischen Mehrkörperproblems." *Zeitschrift für Phys.*, 61(1–2), 126–148.
- Ganguly, A., Chaudhuri, S., and Pal, A. K. (2001). "Synthesis of ZnS_xSe_{1-x} (0 < x < 1) nanocrystalline thin films by high-pressure sputtering." *J. Phys. D: Appl. Phys.*,

34(4), 506–513.

Gessert, T. A., Metzger, W. K., Dippo, P., Asher, S. E., Dhere, R. G., and Young, M. R. (2009a). “Dependence of carrier lifetime on Cu-contacting temperature and ZnTe:Cu thickness in CdS/CdTe thin film solar cells.” *Thin Solid Films*, 517(7), 2370–2373.

Gessert, T. A., Metzger, W. K., Dippo, P., Asher, S. E., Dhere, R. G., and Young, M. R. (2009b). “Dependence of carrier lifetime on Cu-contacting temperature and ZnTe:Cu thickness in CdS/CdTe thin film solar cells.” *Thin Solid Films*, 517(7), 2370–2373.

Gessert, T. A., Wei, S. H., Ma, J., Albin, D. S., Dhere, R. G., Duenow, J. N., Kuciauskas, D., Kanevce, A., Barnes, T. M., Burst, J. M., Rance, W. L., Reese, M. O., and Moutinho, H. R. (2013). “Research strategies toward improving thin-film CdTe photovoltaic devices beyond 20% conversion efficiency.” *Sol. Energy Mater. Sol. Cells*, 119, 149–155.

Ghosh, B., Ghosh, D., Hussain, S., Chakraborty, B. R., Dalai, M. K., Sehgal, G., Bhar, R., and Pal, A. K. (2013). “Utilization of residual CdCl₂ in CBD-CdS to realize grain growth in CdTe: A novel route.” *Mater. Res. Bull.*, 48(11), 4711–4717.

Ghosh, C., and Varma, B. P. (1979). “Optical properties of amorphous and crystalline Sb₂S₃ thin films.” *Thin Solid Films*, 60(1), 61–65.

Giannozzi, P., Andreussi, O., Brumme, T., Bunau, O., Nardelli, M. B., Calandra, M., Car, R., Cavazzoni, C., Ceresoli, D., Cococcioni, M., and others. (2017). “Advanced capabilities for materials modelling with Quantum ESPRESSO. (arXiv:1709.10010v1 [cond-mat.mtrl-sci]).” *J. Phys. Condens. Matter*, 29(46), 465901.

Gloeckler, M., Sankin, I., and Zhao, Z. (2013). “CdTe solar cells at the threshold to 20% efficiency.” *IEEE J. Photovoltaics*, 3(4), 1389–1393.

González-Alcudia, M., Zapata-Torres, M., Meléndez-Lira, M., and Calzadilla Amaya, O. (2008). “Microstructural analysis for europium in CdTe films.” *Superlattices Microstruct.*, 43(5–6), 570–574.

Gonze, X., Amadon, B., Antonius, G., Arnardi, F., Baguet, L., Beuken, J. M., Bieder, J., Bottin, F., Bouchet, J., Bousquet, E., Brouwer, N., Bruneval, F., Brunin, G.,

Cavignac, T., Charraud, J. B., Chen, W., Côté, M., Cottenier, S., Denier, J., Geneste, G., Ghosez, P., Giantomassi, M., Gillet, Y., Gingras, O., Hamann, D. R., Hautier, G., He, X., Helbig, N., Holzwarth, N., Jia, Y., Jollet, F., Lafargue-Dit-Hauret, W., Lejaeghere, K., Marques, M. A. L., Martin, A., Martins, C., Miranda, H. P. C., Naccarato, F., Persson, K., Petretto, G., Planes, V., Pouillon, Y., Prokhorenko, S., Ricci, F., Rignanese, G. M., Romero, A. H., Schmitt, M. M., Torrent, M., Setten, M. J. van, Troeye, B. Van, Verstraete, M. J., Zérah, G., and Zwanziger, J. W. (2020). “The ABINITproject: Impact, environment and recent developments.” *Comput. Phys. Commun.*, 248.

Gordillo, G., Florez, J. M., and Hernandez, L. C. (1995a). “Preparation and characterization of CdTe thin films deposited by CSS.” *Sol. Energy Mater. Sol. Cells*, 37(3–4), 273–281.

Gordillo, G., Flórez, J. M., and Hernández, L. C. (1995b). “Preparation and characterization of CdTe thin films deposited by CSS.” *Sol. Energy Mater. Sol. Cells*, 37(3–4), 273–281.

Green, M., Dunlop, E., Hohl-Ebinger, J., Yoshita, M., Kopidakis, N., and Hao, X. (2021a). “Solar cell efficiency tables (version 57).” *Prog. Photovoltaics Res. Appl.*, 29(1), 3–15.

Green, M., Dunlop, E., Hohl-Ebinger, J., Yoshita, M., Kopidakis, N., and Hao, X. (2021b). “Solar cell efficiency tables (version 57).” *Prog. Photovoltaics Res. Appl.*, 29(1), 3–15.

Grimme, S., Antony, J., Ehrlich, S., and Krieg, H. (2010a). “A consistent and accurate ab initio parametrization of density functional dispersion correction (DFT-D) for the 94 elements H-Pu.” *J. Chem. Phys.*, 132(15).

Grimme, S., Antony, J., Ehrlich, S., and Krieg, H. (2010b). “A consistent and accurate ab initio parametrization of density functional dispersion correction (DFT-D) for the 94 elements H-Pu.” *J. Chem. Phys.*, 132(15), 154104.

Gullu, H. H., Isik, M., Gasanly, N. M., and Parlak, M. (2020). “Influence of temperature on optical properties of electron-beam-evaporated ZnSe thin film.” *Phys. Scr.*, 95(7).

- Guo, J., Zhou, Z., Wang, T., Lu, Z., Yang, Z., and Liu, C. (2017). “Electronic structure and optical properties for blue phosphorene/graphene-like GaN van der Waals heterostructures.” *Curr. Appl. Phys.*, 17(12), 1714–1720.
- Guo, Q., Kume, Y., Fukuhara, Y., Tanaka, T., Nishio, M., Ogawa, H., Hiratsuka, M., Tani, M., and Hangyo, M. (2007). “Observation of ultra-broadband terahertz emission from ZnTe films grown by metalorganic vapor epitaxy.” *Solid State Commun.*, 141(4), 188–191.
- Guo, Z., Zhou, J., Zhu, L., and Sun, Z. (2016). “MXene: A promising photocatalyst for water splitting.” *J. Mater. Chem. A*, 4(29), 11446–11452.
- Hall, R. S., Lamb, D., and Irvine, S. J. C. (2021). “Back contacts materials used in thin film CdTe solar cells—A review.” *Energy Sci. Eng.*, 9(5), 606–632.
- Harif, M. N., Rahman, K. S., Rosly, H. N., Chelvanathan, P., Doroody, C., Misran, H., and Amin, N. (2020). “An approach to alternative post-deposition treatment in CdTe thin films for solar cell application.” *Superlattices Microstruct.*, 147(August), 106687.
- Hartley, A., Irvine, S. J. C., Halliday, D. P., and Potter, M. D. G. (2001). “The influence of CdTe growth ambient on MOCVD grown CdS/CdTe photovoltaic cells.” *Thin Solid Films*, 387(1–2), 89–91.
- Hartree, D. R. (1928). “The Wave Mechanics of an Atom with a Non-Coulomb Central Field Part I Theory and Methods.” *Math. Proc. Cambridge Philos. Soc.*, 24(1), 89–110.
- Hasan, M. M., Hossain, M. M., and Chowdhury, H. K. (2021). “Two-dimensional MXene-based flexible nanostructures for functional nanodevices: a review.” *J. Mater. Chem. A*, 9(6), 3231–3269.
- He, S., Lu, H., Li, B., Zhang, J., Zeng, G., Wu, L., Li, W., Wang, W., and Feng, L. (2017). “Study of CdTe/ZnTe composite absorbing layer deposited by pulsed laser deposition for CdS/CdTe solar cell.” *Mater. Sci. Semicond. Process.*, 67(February), 41–45.
- Heyd, J., Scuseria, G. E., and Ernzerhof, M. (2003). “Hybrid functionals based on a screened Coulomb potential.” *J. Chem. Phys.*, 118(18), 8207–8215.

- Holzwarth, U., and Gibson, N. (2011). “The Scherrer equation versus the ‘Debye-Scherrer equation.’” *Nat. Nanotechnol.*, 6(9), 534.
- Homann, T., Hotje, U., Binnewies, M., Börger, A., Becker, K. D., and Bredow, T. (2006). “Composition-dependent band gap in ZnS_xSe_{1-x}: A combined experimental and theoretical study.” *Solid State Sci.*, 8(1), 44–49.
- Hou, X., Chou, K. C., and Zhang, M. (2010). “The Model for Oxidation Kinetics of Titanium Nitride Coatings.” *Int. J. Appl. Ceram. Technol.*, 7(2), 248–255.
- Huang, M., Xu, P., Han, D., Tang, J., and Chen, S. (2019). “Complicated and Unconventional Defect Properties of the Quasi-One-Dimensional Photovoltaic Semiconductor Sb₂Se₃.” *ACS Appl. Mater. Interfaces*, 11(17), 15564–15572.
- Husain, A. A. F., Hasan, W. Z. W., Shafie, S., Hamidon, M. N., and Pandey, S. S. (2018). “A review of transparent solar photovoltaic technologies.” *Renew. Sustain. Energy Rev.*, 94, 779–791.
- Hwang, H. L., Hsu, K. Y. J., and Ueng, H. Y. (1996). “Fundamental studies of p-type doping of CdTe.” *J. Cryst. Growth*, 161(1–4), 73–81.
- Hwang, S., Larina, L., Lee, H., Kim, S., Choi, K. S., Jeon, C., Ahn, B. T., and Shin, B. (2018). “Wet Pretreatment-Induced Modification of Cu(In,Ga)Se₂/Cd-Free ZnTiO Buffer Interface.” *ACS Appl. Mater. Interfaces*, 10(24), 20920–20928.
- Ibrahim, A. A., El-Sayed, N. Z., Kaid, M. A., and Ashour, A. (2004). “Structural and electrical properties of evaporated ZnTe thin films.” *Vacuum*, 75(3), 189–194.
- Isik, M., Gullu, H. H., Parlak, M., and Gasanly, N. M. (2020). “Synthesis and temperature-tuned band gap characteristics of magnetron sputtered ZnTe thin films.” *Phys. B Condens. Matter*, 582(November 2019).
- Islam, M. A., Rahman, K. S., Sobayel, K., Enam, T., Ali, A. M., Zaman, M., Akhtaruzzaman, M., and Amin, N. (2017). “Fabrication of high efficiency sputtered CdS:O/CdTe thin film solar cells from window/absorber layer growth optimization in magnetron sputtering.” *Sol. Energy Mater. Sol. Cells*, 172(August), 384–393.
- Ismail, B. B., and Gould, R. D. (1989). “Structural and electronic properties of evaporated thin films of cadmium telluride.” *Phys. status solidi*, 115(1), 237–245.

- Jana, S., Maity, R., Das, S., Mitra, M. K., and Chattopadhyay, K. K. (2007). “Synthesis, structural and optical characterization of nanocrystalline ternary Cd_{1-x}Zn_xS thin films by chemical process.” *Phys. E Low-Dimensional Syst. Nanostructures*, 39(1), 109–114.
- Jiang, Q. W., Li, G. R., and Gao, X. P. (2009). “Highly ordered TiN nanotube arrays as counter electrodes for dye-sensitized solar cells.” *Chem. Commun.*, (44), 6720–6722.
- Jiao, S., Shen, Q., Mora-Sero, I., Wang, J., Pan, Z., Zhao, K., Kuga, Y., Zhong, X., and Bisquert, J. (2015). “Band Engineering in Core / Shell ZnTe / CdSe for Photovoltage and Efficiency Enhancement in Exciplex.” *ACS Nano*, 9(1), 908–915.
- Jin, X., Li, H., Huang, S., Gu, X., Shen, H., Li, D., Zhang, X., Zhang, Q., Li, F., and Li, Q. (2018). “Bright alloy type-II quantum dots and their application to light-emitting diodes.” *J. Colloid Interface Sci.*, 510, 376–383.
- Jung, J. Y., Park, J. H., Jeong, Y. J., Yang, K. H., Choi, N. K., Kim, S. H., and Kim, W. J. (2006). “Involvement of Bcl-2 family and caspases cascade in sodium fluoride-induced apoptosis of human gingival fibroblasts.” *Korean J. Physiol. Pharmacol.*, 10(5), 289–295.
- Kagan, C. R., Lifshitz, E., Sargent, E. H., and Talapin, D. V. (2016). “Building devices from colloidal quantum dots.” *Science* (80-.), 353(6302).
- Kaito, C., Fujita, T., Kimura, T., Hanamoto, K., Suzuki, N., Kimura, S., and Saito, Y. (1998). “Structure and crystallization of Sb-Se films prepared by vacuum evaporation method.” *Thin Solid Films*, 312(1–2), 93–98.
- Kale, R. B., and Lokhande, C. D. (2004). “Room temperature deposition of ZnSe thin films by successive ionic layer adsorption and reaction (SILAR) method.” *Mater. Res. Bull.*, 39(12), 1829–1839.
- Kale, S. S., and Lokhande, C. D. (2000). “Thickness-dependent properties of chemically deposited CdSe thin films.” *Mater. Chem. Phys.*, 62(2), 103–108.
- Kanevce, A., and Gessert, T. A. (2011). “Optimizing CdTe solar cell performance: Impact of variations in minority-carrier lifetime and carrier density profile.” *IEEE J. Photovoltaics*, 1(1), 99–103.

- Kannappan, P., Asokan, K., Krishna, J. B. M., and Dhanasekaran, R. (2013). "Effect of SHI irradiation on structural, surface morphological and optical studies of CVT grown ZnSSe single crystals." *J. Alloys Compd.*, 580, 284–289.
- Kazmi, S. A. A., Khan, A. D., Khan, A. D., Rauf, A., Farooq, W., Noman, M., and Ali, H. (2020). "Efficient materials for thin-film CdTe solar cell based on back surface field and distributed Bragg reflector." *Appl. Phys. A Mater. Sci. Process.*, 126(1).
- Khairnar, U. P., Bhavsar, D. S., Vaidya, R. U., and Bhavsar, G. P. (2003). "Optical properties of thermally evaporated cadmium telluride thin films." *Mater. Chem. Phys.*, 80(2), 421–427.
- Khan, A. H., Bertrand, G. H. V., Teitelboim, A., Sekhar M, C., Polovitsyn, A., Brescia, R., Planelles, J., Climente, J. I., Oron, D., and Moreels, I. (2020). "CdSe/CdS/CdTe Core/Barrier/Crown Nanoplatelets: Synthesis, Optoelectronic Properties, and Multiphoton Fluorescence Upconversion." *ACS Nano*, 14(4), 4206–4215.
- Khazaei, M., Arai, M., Sasaki, T., Chung, C. Y., Venkataramanan, N. S., Estili, M., Sakka, Y., and Kawazoe, Y. (2013). "Novel Electronic and Magnetic Properties of Two-Dimensional Transition Metal Carbides and Nitrides." *Adv. Funct. Mater.*, 23(17), 2185–2192.
- Khurram, A. A., Imran, M., Khan, N. A., and Mehmood, M. N. (2017). "ZnSe/ITO thin films: Candidate for CdTe solar cell window layer." *J. Semicond.*, 38(9).
- Kim, D., Kim, J., Yang, G., Chun, S., and Jung, Y. (2014). "Post-growth CdCl₂ treatment on CdTe thin films grown on graphene layers using a close-spaced sublimation method." *Opt. Express*, Vol. 22, Issue S3, pp. A986-A991, 22(103), A986–A991.
- Kim, S. J., Naguib, M., Zhao, M., Zhang, C., Jung, H. T., Barsoum, M. W., and Gogotsi, Y. (2015). "High mass loading, binder-free MXene anodes for high areal capacity Li-ion batteries." *Electrochim. Acta*, 163, 246–251.
- Koma, A. (1999). "Van der Waals epitaxy for highly lattice-mismatched systems." *J. Cryst. Growth*, 201, 236–241.

- Kresse, G., and Furthmüller, J. (1996a). “Efficient iterative schemes for ab initio total-energy calculations using a plane-wave basis set.” *Phys. Rev. B*, 54(16), 11169.
- Kresse, G., and Furthmüller, J. (1996b). “Efficiency of ab-initio total energy calculations for metals and semiconductors using a plane-wave basis set.” *Comput. Mater. Sci.*, 6(1), 15–50.
- Kuang, P., Low, J., Cheng, B., Yu, J., and Fan, J. (2020). “MXene-based photocatalysts.” *J. Mater. Sci. Technol.*, 56, 18–44.
- Kulkarni, R., Rondiya, S., Pawbake, A., Waykar, R., Jadhavar, A., Jadkar, V., Bhorde, A., Date, A., Pathan, H., and Jadkar, S. (2017). “Structural and Optical Properties of CdTe Thin Films Deposited Using RF Magnetron Sputtering.” *Energy Procedia*, 110(December 2016), 188–195.
- Kumar, S., Kang, D., Nguyen, V. H., Nasir, N., Hong, H., Kim, M., Nguyen, D. C., Lee, Y. J., Lee, N., and Seo, Y. (2021a). “Application of Titanium-Carbide MXene-Based Transparent Conducting Electrodes in Flexible Smart Windows.” *ACS Appl. Mater. Interfaces*, 13(34), 40976–40985.
- Kumar, S., Khan, Z. H., Khan, M. A. M., and Husain, M. (2005). “Studies on thin films of lead chalcogenides.” *Curr. Appl. Phys.*, 5(6), 561–566.
- Kumar, S., Parly, Riya, Saravanan, M. P., Deshpande, U., and Venkatesh, R. (2021b). “Structural, morphological and optoelectronic properties of screen-printed film deposited using Sb₂Se₃nanowires.” *AIP Conf. Proc.*, 2369(1).
- Kumar, V., Singh, V., Sharma, S. K., and Sharma, T. P. (1998). “Structural and optical properties of sintered Cd_{1-x}Zn_xS films.” *Opt. Mater. (Amst.)*, 11(1), 29–34.
- L. H. Thomas. (n.d.). “On the Capture of Electrons by Swiftly Moving Electrified Particles.”
- Lai, Y., Han, C., Lv, X., Yang, J., Liu, F., Li, J., and Liu, Y. (2012). “Electrodeposition of antimony selenide thin films from aqueous acid solutions.” *J. Electroanal. Chem.*, 671, 73–79.
- Lee, K. H., Lee, J. H., Kang, H. D., Park, B., Kwon, Y., Ko, H., Lee, C., Lee, J., and Yang, H. (2014). “Over 40 cd/A efficient green quantum dot electroluminescent

device comprising uniquely large-sized quantum dots.” *ACS Nano*, 8(5), 4893–4901.

Li, C., Wang, F., Chen, Y., Wu, L., Zhang, J., Li, W., He, X., Li, B., and Feng, L. (2018). “Characterization of sputtered CdSe thin films as the window layer for CdTe solar cells.” *Mater. Sci. Semicond. Process.*, 83(January), 89–95.

Li, Y. M., Chen, W. G., Guo, Y. L., and Jiao, Z. Y. (2019). “Theoretical investigations of TiNbC MXenes as anode materials for Li-ion batteries.” *J. Alloys Compd.*, 778, 53–60.

Li, Y., Zhou, Y., Luo, J., Chen, W., Yang, B., Wen, X., Lu, S., Chen, C., Zeng, K., Song, H., and Tang, J. (2016a). “The effect of sodium on antimony selenide thin film solar cells.” *RSC Adv.*, 6(90), 87288–87293.

Li, Y., Zhou, Y., Zhu, Y., Chen, C., Luo, J., Ma, J., Yang, B., Wang, X., Xia, Z., and Tang, J. (2016b). “Characterization of Mg and Fe doped Sb₂Se₃ thin films for photovoltaic application.” *Appl. Phys. Lett.*, 109(23).

Li, Z., Chen, X., Zhu, H., Chen, J., Guo, Y., Zhang, C., Zhang, W., Niu, X., and Mai, Y. (2017). “Sb₂Se₃ thin film solar cells in substrate configuration and the back contact selenization.” *Sol. Energy Mater. Sol. Cells*, 161(October 2016), 190–196.

Lingwal, V., and Panwar, N. S. (2005). “Scanning magnetron-sputtered TiN coating as diffusion barrier for silicon devices.” *J. Appl. Phys.*, 97(10).

Liu, C., Hao, S., Chen, X., Zong, B., and Mao, S. (2020). “High Anti-Interference Ti₃C₂T_xMXene Field-Effect-Transistor-Based Alkali Indicator.” *ACS Appl. Mater. Interfaces*, 12(29), 32970–32978.

Liu, J. (2015). “Origin of high photocatalytic efficiency in monolayer g-C₃N₄/CdS heterostructure: a hybrid DFT study.” *J. Phys. Chem. C*, 119(51), 28417–28423.

Liu, X., Chen, J., Luo, M., Leng, M., Xia, Z., Zhou, Y., Qin, S., Xue, D., Lv, L., Huang, H., Niu, D., and Tang, J. (2014). “Thermal Evaporation and Characterization of Sb₂Se₃ Thin Film for Substrate Sb₂Se₃ / CdS Solar Cells.”

Liu, X., Xiao, X., Yang, Y., Xue, D. J., Li, D. B., Chen, C., Lu, S., Gao, L., He, Y., Beard, M. C., Wang, G., Chen, S., and Tang, J. (2017). “Enhanced Sb₂Se₃ solar cell performance through theory-guided defect control.” *Prog. Photovoltaics Res. Appl.*,

25(10), 861–870.

Lohar, G. M., Shinde, S. K., and Fulari, V. J. (2014). “Structural, morphological, optical and photoluminescent properties of spray-deposited ZnSe thin film.” *J. Semicond.*, 35(11).

Lokhande, C. D., Patil, P. S., Ennaoui, A., and Tributsch, H. (1998). “Chemical bath ZnSe thin films: Deposition and characterisation.” *Appl. Surf. Sci.*, 123–124, 294–297.

Lokhande, C. D., Sankapal, B. R., Mane, R. S., Pathan, H. M., Muller, M., Giersig, M., Tributsch, H., and Ganeshan, V. (2002). “Structural characterization of chemically deposited Bi₂S₃ and Bi₂Se₃ thin films.” *Appl. Surf. Sci.*, 187(1–2), 108–115.

Lu, W., Song, B., Li, H., Zhou, J., Dong, W., Zhao, G., and Han, G. (2020). “Strategy for performance enhancement of Cd_{1-x}Zn_xTe/CdS core/shell quantum dot sensitized solar cells through band adjustment.” *J. Alloys Compd.*, 826, 154050.

Ma, L., Xu, L., Xu, X., Zhou, X., Luo, J., and Zhang, L. (2016). “Cobalt-doped edge-rich MoS₂/nitrogenated graphene composite as an electrocatalyst for hydrogen evolution reaction.” *Mater. Sci. Eng. B Solid-State Mater. Adv. Technol.*, 212, 30–38.

Maghraoui-Meherzi, H., Nasr, T. Ben, and Dachraoui, M. (2013). “Synthesis, structure and optical properties of Sb₂Se₃.” *Mater. Sci. Semicond. Process.*, 16(1), 179–184.

Mahmood, Q., Murtaza, G., Ali, G., Hassan, M., Algrafy, E., Shahid, M. S., Kattan, N. A., and Laref, A. (2020). “Probing the electronic structure and magnetism in Ni doped ZnTe: a DFT modeling and experiment.” *J. Alloys Compd.*, 834, 155176.

Maissel, L. I., Glang, R., and Budenstein, P. P. (1971). “Handbook of Thin Film Technology.” *J. Electrochem. Soc.*, 118(4), 114C.

Maki, S. A., and Hassun, H. K. (2016). “The Structural and Optical Properties of Zinc Telluride Thin Films by Vacuum Thermal Evaporation Technique.” *Ibn Al-Haitham J. Pure Appl. Sci.*, 29(2), 70–80.

Martin, R. M. (2004). “Electronic Structure: Basic Theory and Practical Methods.”

- Mathuri, S., Ramamurthi, K., and Ramesh Babu, R. (2016). "Effect of substrate temperature on the structural and optical properties of CdSe thin film deposited by electron beam evaporation technique." *J. Mater. Sci. Mater. Electron.*, 27(7), 7582–7588.
- Matin, M. A., Mannir Aliyu, M., Quadery, A. H., and Amin, N. (2010). "Prospects of novel front and back contacts for high efficiency cadmium telluride thin film solar cells from numerical analysis." *Sol. Energy Mater. Sol. Cells*, 94(9), 1496–1500.
- Matin, M. A., Tomal, M. U., and Robin, A. M. (2013). "Copper telluride as a novel BSF material for high performance ultra thin CdTe PV cell." *2013 Int. Conf. Informatics, Electron. Vision, ICIEV 2013*.
- Matsumoto, H., Kuribayashi, K., Uda, H., Komatsu, Y., Nakano, A., and Ikegami, S. (1984). "Screen-printed CdS/CdTe solar cell of 12.8% efficiency for an active area of 0.78 cm²." *Sol. Cells*, 11(4), 367–373.
- McCandless, B., Buchanan, W., Sriramagiri, G., Thompson, C., Duenow, J., Albin, D., Jensen, S. A., Moseley, J., Al-Jassim, M., and Metzger, W. K. (2019). "Enhanced p-Type Doping in Polycrystalline CdTe Films: Deposition and Activation." *IEEE J. Photovoltaics*, 9(3), 912–917.
- Messina, S., Nair, M. T. S., and Nair, P. K. (2009). "Antimony Selenide Absorber Thin Films in All-Chemically Deposited Solar Cells." *J. Electrochem. Soc.*, 156(5), H327.
- Michael, J., Qifeng, Z., and Danling, W. (2019). "Titanium carbide MXene: Synthesis, electrical and optical properties and their applications in sensors and energy storage devices." *Nanomater. Nanotechnol.*, 9, 1–9.
- Mitchell, K. W., Eberspacher, C., Cohen, F., Avery, J., Duran, G., and Bottenberg, W. (1988). "Progress towards high efficiency thin film CdTe solar cells." *Sol. Cells*, 23(1–2), 49–57.
- Mohammed, K. A., AL-Kabbi, A. S., and Zidan, K. M. (2019). "Synthesis and characterization of CdSe nanoparticles." *AIP Conf. Proc.*, 2144(1), 30009.
- Mohanta, M. K., Rawat, A., Dimple, Jena, N., Ahammed, R., and Sarkar, A. De. (2019). "Superhigh out-of-plane piezoelectricity, low thermal conductivity and

photocatalytic abilities in ultrathin 2D van der Waals heterostructures of boron monophosphide and gallium nitride.” *Nanoscale*, 11(45), 21880–21890.

Mohanta, M. K., Rawat, A., Jena, N., Dimple, Ahammed, R., and Sarkar, A. De. (2020). “Interfacing Boron Monophosphide with Molybdenum Disulfide for an Ultrahigh Performance in Thermoelectrics, Two-Dimensional Excitonic Solar Cells, and Nanopiezotronics.” *ACS Appl. Mater. Interfaces*, 12(2), 3114–3126.

Monika, S., Mahalakshmi, M., and Pandian, M. S. (2023). “TiO₂/CdS/CdSe quantum dots co-sensitized solar cell with the staggered-gap (type-II) heterojunctions for the enhanced photovoltaic performance.” *Ceram. Int.*, 49(6), 8820–8826.

Morkoç, H., Strite, S., Gao, G. B., Lin, M. E., Sverdlov, B., and Burns, M. (1994). “Large-band-gap SiC, III-V nitride, and II-VI ZnSe-based semiconductor device technologies.” *J. Appl. Phys.*, 76(3), 1363–1398.

Moutinho, H. R., Al-Jassim, M. M., Abulfotuh, F. A., Levi, D. H., Dippo, P. C., Dhere, R. G., and Kazmerski, L. L. (1997). “Studies of recrystallization of CdTe thin films after CdCl₂ treatment.” *Conf. Rec. IEEE Photovolt. Spec. Conf.*, 431–434.

Moutinho, H. R., Hasoon, F. S., Abulfotuh, F., and Kazmerski, L. L. (1995). “Investigation of polycrystalline CdTe thin films deposited by physical vapor deposition, close-spaced sublimation, and sputtering.” *J. Vac. Sci. Technol. A*, 13(6), 2877–2883.

Mrinalini, M., Islavath, N., Prasanthkumar, S., and Giribabu, L. (2019). “Stipulating Low Production Cost Solar Cells All Set to Retail...!” *Chem. Rec.*, 19(2–3), 661–674.

Nakano, A., Ikegami, S., Matsumoto, H., Uda, H., and Komatsu, Y. (1986). “Long-term reliability of screen printed CdS/CdTe solar-cell modules.” *Sol. Cells*, 17(2–3), 233–240.

Nasir, J. A., Rehman, Z. U., Shah, S. N. A., Khan, A., Butler, I. S., and Catlow, C. R. A. (2020). “Recent developments and perspectives in CdS-based photocatalysts for water splitting.” *J. Mater. Chem. A*, 8(40), 20752–20780.

Nikale, V. M., Shinde, S. S., Bhosale, C. H., and Rajpure, K. Y. (2011). “Physical properties of spray deposited CdTe thin films: PEC performance.” *J. Semicond.*, 32(3), 033001.

- Oklobia, O., Kartopu, G., and Irvine, S. J. C. (2019). "Properties of Arsenic-Doped ZnTe Thin Films as a Back Contact for CdTe Solar Cells." *Mater.* 2019, Vol. 12, Page 3706, 12(22), 3706.
- P. HOHENBERG, W. K. (1964). "Inhomogeneous Electron Gas." *Phys. Rev.*, 136.
- Pandey, S. K., Tiwari, U., Raman, R., Prakash, C., Krishna, V., Dutta, V., and Zimik, K. (2005). "growth of cubic and hexagonal CdTe thin film by pulsed laser deposition." *thin solid films*.
- Park, K. C., Cha, E. S., and Ahn, B. T. (2011). "Sodium-doping of ZnTe film by close-spaced sublimation for back contact of CdTe solar cell." *Curr. Appl. Phys.*, 11(1 SUPPL.), S109–S112.
- Patil, N. M., Nilange, S. G., and Yadav, A. A. (2018). "Growth and characterization of ZnS_xSe_{1-x} thin films deposited by spray pyrolysis." *Thin Solid Films*, 664(October 2017), 19–26.
- Patra, S., and Pradhan, S. K. (2012). "Microstructural, optical and quantum confinement effect study of mechanically synthesized ZnTe quantum dots." *Acta Mater.*, 60(1), 131–138.
- Patrick, C. E., and Giustino, F. (2011a). "Structural and Electronic Properties of Semiconductor-Sensitized Solar-Cell Interfaces." *Adv. Funct. Mater.*, 21(24), 4663–4667.
- Patrick, C. E., and Giustino, F. (2011b). "Structural and Electronic Properties of Semiconductor-Sensitized Solar-Cell Interfaces." *Adv. Funct. Mater.*, 21(24), 4663–4667.
- Peng, X., Tang, F., and Coppale, A. (2012). "Engineering the work function of armchair graphene nanoribbons using strain and functional species: A first principles study." *J. Phys. Condens. Matter*, 24(7).
- Perdew, J. P., Burke, K., and Ernzerhof, M. (1996). "Generalized gradient approximation made simple." *Phys. Rev. Lett.*, 77(18), 3865–3868.
- Perdew, J. P., and Wang, Y. (2018). "Erratum: Accurate and simple analytic representation of the electron-gas correlation energy (Physical Review B (1992) 45

- (13244) DOI: 10.1103/PhysRevB.45.13244).” *Phys. Rev. B*, 98(7), 244–249.
- Perera, F. P. (2017). “Multiple threats to child health from fossil fuel combustion: Impacts of air pollution and climate change.” *Environ. Health Perspect.*, 125(2), 141–148.
- Pochareddy, S. A., Nicholson, A. P., Thiagarajan, A., Shah, A., and Sampath, W. S. (2021). “Structural and Electronic Calculations of CdTe Using DFT: Exchange–Correlation Functionals and DFT-1/2 Corrections.” *J. Electron. Mater.*, 50(4), 2216–2222.
- Poplawsky, J. D., Guo, W., Paudel, N., Ng, A., More, K., Leonard, D., and Yan, Y. (2016). “Structural and compositional dependence of the CdTe x Se 1-x alloy layer photoactivity in CdTe-based solar cells.” *Nat. Commun.*, 7, 1–10.
- Potter, B. G., and Simmons, J. H. (1990). “Quantum-confinement effects in CdTe-glass composite thin films produced using rf magnetron sputtering.” *J. Appl. Phys.*, 68(3), 1218–1224.
- Radaf, I. M. El. (2019). “Structural, optical, optoelectrical and photovoltaic properties of the thermally evaporated Sb₂Se₃ thin films.” *Appl. Phys. A Mater. Sci. Process.*, 125(12), 1–11.
- Rajavel, D., and Summers, C. J. (1992). “Gas source iodine n-type doping of molecular beam epitaxially grown CdTe.” *Appl. Phys. Lett.*, 60(18), 2231–2233.
- Rao, G. K., Bangera, K. V, and Shivakumar, G. K. (2009). “The effect of substrate temperature on the structural, optical and electrical properties of vacuum deposited ZnTe thin films.” *Vacuum*, 83(12), 1485–1488.
- Ren, S., Li, H., Lei, C., Li, C., Yin, X., Wu, L., Li, W., Zhang, J., Wang, W., and Feng, L. (2019). “Interface modification to enhance electron extraction by deposition of a ZnMgO buffer on SnO₂-coated FTO in CdTe solar cells.” *Sol. Energy*, 177(November 2018), 545–552.
- Ringel, S. A., Smith, A. W., MacDougal, M. H., and Rohatgi, A. (1991a). “The effects of CdCl₂ on the electronic properties of molecular-beam epitaxially grown CdTe/CdS heterojunction solar cells.” *J. Appl. Phys.*, 70(2), 881–889.

- Ringel, S. A., Smith, A. W., MacDougal, M. H., and Rohatgi, A. (1991b). “The effects of CdCl₂ on the electronic properties of molecular-beam epitaxially grown CdTe/CdS heterojunction solar cells.” *J. Appl. Phys.*, 70(2), 881–889.
- Rogach, A. L. (2000). “Nanocrystalline CdTe and CdTe(S) particles: Wet chemical preparation, size-dependent optical properties and perspectives of optoelectronic applications.” *Mater. Sci. Eng. B Solid-State Mater. Adv. Technol.*, 69, 435–440.
- Rosa, S. (1984). “for Photovoltaic Applications.” 27(4), 329–337.
- Savory, C. N., and Scanlon, D. O. (2019). “The complex defect chemistry of antimony selenide.” *J. Mater. Chem. A*, 7(17), 10739–10744.
- Schwab, H., Dörnfeld, C., Göbel, E. O., Hvam, J. M., Klingshirn, C., Kuhl, J., Lyssenko, V. G., Majumder, F. A., Noll, G., Nunnenkamp, J., Pantke, K. H., Renner, R., Reznitsky, A., Siegner, U., Swoboda, H. E., and Weber, C. (1992). “Dynamics of Excitons in CdS, CdSe, and CdS_{1-x}Se_x.” *Phys. status solidi*, 172(2), 479–519.
- Segall, M. D., Lindan, P. J. D., Probert, M. J., Pickard, C. J., Hasnip, P. J., Clark, S. J., and Payne, M. C. (2002). “First-principles simulation: Ideas, illustrations and the CASTEP code.” *J. Phys. Condens. Matter*, 14(11), 2717–2744.
- Seyam, M. A. M. (2012). “Effect of substrate temperature on photoconductivity, structural, and optical properties of vacuum evaporated Zinc Telluride films.” *J. Alloys Compd.*, 541, 448–453.
- Shaaban, E. R., Afify, N., and El-Taher, A. (2009). “Effect of film thickness on microstructure parameters and optical constants of CdTe thin films.” *J. Alloys Compd.*, 482(1–2), 400–404.
- Shao, L. X., Chang, K. H., and Hwang, H. L. (2003). “Zinc sulfide thin films deposited by RF reactive sputtering for photovoltaic applications.” *Appl. Surf. Sci.*, 212–213(SPEC.), 305–310.
- Sharma, R., Himanshu, Patel, S. L., Chander, S., Kannan, M. D., and Dhaka, M. S. (2020). “Physical properties of ZnSe thin films: Air and vacuum annealing evolution to buffer layer applications.” *Phys. Lett. Sect. A Gen. At. Solid State Phys.*, 384(4), 126097.

Sharma, R., Sharma, A., Himanshu, Thakur, A., Kannan, M. D., and Dhaka, M. S. (2023). “Combinatorial study to the physical properties of Cd_{1-x}Zn_xTe thin films as budding absorber for solar cell applications.” *Mater. Res. Bull.*, 163(September 2022), 112214.

Shen, D., Au, S. Y., Han, G., Que, D., Wang, N., and Sou, I. K. (2003). “MBE growth and structural characterization of ZnS_{1-x}Se_x thin films on ITO/glass substrates.” *J. Mater. Sci. Lett.*, 22(6), 483–487.

Shenoy, S., and Tarafder, K. (2020). “Enhanced photocatalytic efficiency of layered CdS/CdSe heterostructures: Insights from first principles electronic structure calculations.” *J. Phys. Condens. Matter*, 32(27).

Shi, X., Zhang, X., Tian, Y., Shen, C., Wang, C., and Gao, H. J. (2012). “Electrodeposition of Sb₂Se₃ on indium-doped tin oxides substrate: Nucleation and growth.” *Appl. Surf. Sci.*, 258(6), 2169–2173.

Shockley, W., and Queisser, H. J. (1961). “Detailed Balance Limit of Efficiency of p-n Junction Solar Cells.” *J. Appl. Phys.*, 32(3), 510–519.

Shreekanthan, K. N., Bangera, K. V., Shivakumar, G. K., and Mahesha, M. G. (2006a). “Structure and properties of vacuum deposited cadmium telluride thin films.” *Indian J. Pure Appl. Phys.*, 44(9), 705–708.

Shreekanthan, K. N., Bangera, K. V., Shivakumar, G. K., and Mahesha, M. G. (2006b). “Structure and properties of vacuum deposited cadmium telluride thin films.” *Indian J. Pure Appl. Phys.*, 44, 705–708.

Shtrikman, H., Raizman, A., Oron, M., and Eger, D. (1988). “ZnTe layers grown on GaAs substrates by low pressure MOCVD.” *J. Cryst. Growth*, 88(4), 522–526.

Sites, J., and Pan, J. (2007). “Strategies to increase CdTe solar-cell voltage.” *Thin Solid Films*, 515(15 SPEC. ISS.), 6099–6102.

Smidstrup, S., Markussen, T., Vancraeyveld, P., Wellendorff, J., Schneider, J., Gunst, T., Verstichel, B., Stradi, D., Khomyakov, P. A., Vej-Hansen, U. G., Lee, M. E., Chill, S. T., Rasmussen, F., Penazzi, G., Corsetti, F., Ojanperä, A., Jensen, K., Palsgaard, M. L. N., Martinez, U., Blom, A., Brandbyge, M., and Stokbro, K. (2020). “QuantumATK: An integrated platform of electronic and atomic-scale modelling

- tools.” *J. Phys. Condens. Matter*, 32(1).
- Soler, M., Artacho, E., Gale, J. D., Garc, A., Junquera, J., Ordej, P., and Daniel, S. (2002). “Soler2002.”
- Song, J. H., Sim, E. D., Baek, K. S., and Chang, S. K. (2000). “Optical properties of ZnS_xSe_{1-x} ($x < 0.18$) random and ordered alloys grown by metalorganic atomic layer epitaxy.” *J. Cryst. Growth*, 214, 460–464.
- Souri, S., and Marandi, M. (2023). “Numerical modelling of the effect of the Ag: ZnSe BSF layer on the high performance of ZnSe/CdTe thin film solar cells by SCAPS-1D software.” *Opt. Quantum Electron.*, 55(5), 1–14.
- Späth, B., Fritsche, J., Klein, A., and Jaegermann, W. (2007). “Nitrogen doping of ZnTe and its influence on CdTe/ZnTe interfaces.” *Appl. Phys. Lett.*, 90(6).
- Suthar, D., Himanshu, Patel, S. L., Chander, S., Kannan, M. D., and Dhaka, M. S. (2021a). “Thickness and annealing evolution to physical properties of e-beam evaporated ZnTe thin films as a rear contact for CdTe solar cells.” *J. Mater. Sci. Mater. Electron.*, 32(14), 19070–19082.
- Suthar, D., Himanshu, Patel, S. L., Chander, S., Kannan, M. D., and Dhaka, M. S. (2021b). “Thickness and annealing evolution to physical properties of e-beam evaporated ZnTe thin films as a rear contact for CdTe solar cells.” *J. Mater. Sci. Mater. Electron.*, 32(14), 19070–19082.
- Sutrave, D. S., Shahane, G. S., Patil, V. B., and Deshmukh, L. P. (2000). “Micro-crystallographic and optical studies on $Cd_{1-x}Zn_xSe$ thin films.” *Mater. Chem. Phys.*, 65(3), 298–305.
- Tanaka, T., Kume, Y., Nishio, M., Guo, Q., Ogawa, H., and Yoshida, A. (2003). “Fabrication of ZnTe light-emitting diodes using Bridgman-grown substrates.” *Japanese J. Appl. Physics, Part 2 Lett.*, 42(4 A).
- Tang, H., Feng, H., Wang, H., Wan, X., Liang, J., and Chen, Y. (2019). “Highly Conducting MXene-Silver Nanowire Transparent Electrodes for Flexible Organic Solar Cells.” *ACS Appl. Mater. Interfaces*, 11(28), 25330–25337.
- Tauc, J. (1972). “STATES IN THE GAP.” 10, 569–585.

- Tauc, J., and Menth, A. (1972). “States in the gap.” *J. Non. Cryst. Solids*, 8–10(C), 569–585.
- Teller, E. (1962). “On the stability of molecules in the Thomas-Fermi theory.” *Rev. Mod. Phys.*, 34(4), 627–631.
- Tumelero, M. A., Faccio, R., and Pasa, A. A. (2016). “Unraveling the native conduction of trichalcogenides and its ideal band alignment for new photovoltaic interfaces.” *J. Phys. Chem. C*, 120(3), 1390–1399.
- Urbankowski, P., Anasori, B., Makaryan, T., Er, D., Kota, S., Walsh, P. L., Zhao, M., Shenoy, V. B., Barsoum, M. W., and Gogotsi, Y. (2016). “Synthesis of two-dimensional titanium nitride Ti₄N₃ (MXene).” *Nanoscale*, 8(22), 11385–11391.
- Vasilyev, S., Moskalev, I., Mirov, M., Mirov, S., and Gapontsev, V. (2016). “Multi-Watt mid-IR femtosecond polycrystalline Cr²⁺:ZnS and Cr²⁺:ZnSe laser amplifiers with the spectrum spanning 20–26 μm.” *Opt. Express*, 24(2), 1616.
- Venkatachalam, S., Mangalaraj, D., and Narayandass, S. K. (2007). “Characterization of vacuum-evaporated ZnSe thin films.” *Phys. B Condens. Matter*, 393(1–2), 47–55.
- Virt, I. S., Rudyj, I. O., Kurilo, I. V., Lopatynskiy, I. Y., Linnik, L. F., Tetyorkin, V. V., Potera, P., and Luka, G. (2013). “Properties of Sb₂S₃ and Sb₂Se₃ thin films obtained by pulsed laser ablation.” *Semiconductors*, 47(7), 1003–1007.
- Visoly-Fisher, I., Dobson, K. D., Nair, J., Bezalel, E., Hodes, G., and Cahen, D. (2003). “Factors Affecting the Stability of CdTe/CdS Solar Cells Deduced from Stress Tests at Elevated Temperature.” *Adv. Funct. Mater.*, 13(4), 289–299.
- Vos, A. De. (1980). “Detailed balance limit of the efficiency of tandem solar cells.” *J. Phys. D. Appl. Phys.*, 13(5), 839–846.
- W. KOHN AND L. J. SHAM. (1965). “Self-Consistent Equations Including Exchange and Correlation Effects.” *Phys. Rev.*, 140.
- Wang, B. B., Zhu, M. K., Wang, H., and Dong, G. B. (2011). “Study on growth and photoluminescence of zinc telluride crystals synthesized by hydrothermal method.” *Opt. Mater. (Amst.)*, 34(1), 42–47.
- Wang, L., Li, D. B., Li, K., Chen, C., Deng, H. X., Gao, L., Zhao, Y., Jiang, F., Li, L.,

- Huang, F., He, Y., Song, H., Niu, G., and Tang, J. (2017). “Stable 6%-efficient Sb₂Se₃ solar cells with a ZnO buffer layer.” *Nat. Energy*, 2(4), 1–9.
- Wang, W., Bowen, W., Spanninga, S., Lin, S., and Phillips, J. (2009). “Optical characteristics of ZnTeO thin films synthesized by pulsed laser deposition and molecular beam epitaxy.” *J. Electron. Mater.*, 38(1), 119–125.
- Wang, X., Quhe, R., Cui, W., Zhi, Y., Huang, Y., An, Y., Dai, X., Tang, Y., Chen, W., Wu, Z., and Tang, W. (2018). “Electric field effects on the electronic and optical properties in C₂N/Sb van der Waals heterostructure.” *Carbon N. Y.*, 129, 738–744.
- Wen, X., Chen, C., Lu, S., Li, K., Kondrotas, R., Zhao, Y., Chen, W., Gao, L., Wang, C., Zhang, J., Niu, G., and Tang, J. (2018). “Vapor transport deposition of antimony selenide thin film solar cells with 7.6% efficiency.” *Nat. Commun.*, 9(1).
- Wolden, C. A., Abbas, A., Li, J., Diercks, D. R., Meysing, D. M., Ohno, T. R., Beach, J. D., Barnes, T. M., and Walls, J. M. (2016). “The roles of ZnTe buffer layers on CdTe solar cell performance.” *Sol. Energy Mater. Sol. Cells*, 147, 203–210.
- Wu, X. (2004). “High-efficiency polycrystalline CdTe thin-film solar cells.” *Sol. energy*, 77(6), 803–814.
- Xin, P., Larsen, J. K., Deng, F., and Shafarman, W. N. (2016). “Development of Cu(In,Ga)Se₂ superstrate devices with alternative buffer layers.” *Sol. Energy Mater. Sol. Cells*, 157, 85–92.
- Xu, B., Zhu, M., Zhang, W., Zhen, X., Pei, Z., Xue, Q., Zhi, C., and Shi, P. (2016). “Ultrathin MXene-Micropattern-Based Field-Effect Transistor for Probing Neural Activity.” *Adv. Mater.*, 28(17), 3333–3339.
- Xu, Q., Zhang, L., Yu, J., Wageh, S., Al-ghamdi, A. A., and Jaroniec, M. (2018). “Direct Z-scheme photocatalysts : Principles , synthesis , and applications.” *Mater. Today*, 21(10), 1042–1063.
- Xu, Q., Zong, B., Li, Q., Fang, X., Mao, S., and Ostrikov, K. (Ken). (2022). “H₂S sensing under various humidity conditions with Ag nanoparticle functionalized Ti₃C₂T_x MXene field-effect transistors.” *J. Hazard. Mater.*, 424(PB), 127492.
- Yang, J. H., Yin, W. J., Park, J. S., Burst, J., Metzger, W. K., Gessert, T., Barnes, T.,

- and Wei, S. H. (2015). “Enhanced p-type dopability of P and As in CdTe using non-equilibrium thermal processing.” *J. Appl. Phys.*, 118(2), 25102.
- Yang, Y., Kang, X., Huang, L., and Pan, D. (2016). “Tuning the Band Gap of Cu₂ZnSn(S,Se)₄ Thin Films via Lithium Alloying.” *ACS Appl. Mater. Interfaces*, 8(8), 5308–5313.
- Yoshikawa, K., Kawasaki, H., Yoshida, W., Irie, T., Konishi, K., Nakano, K., Uto, T., Adachi, D., Kanematsu, M., Uzu, H., and Yamamoto, K. (2017). “Silicon heterojunction solar cell with interdigitated back contacts for a photoconversion efficiency over 26%.” *Nat. Energy*, 2(5).
- Yuan, C., Jin, X., Jiang, G., Liu, W., and Zhu, C. (2016). “Sb₂Se₃ solar cells prepared with selenized dc-sputtered metallic precursors.” *J. Mater. Sci. Mater. Electron.*, 27(9), 8906–8910.
- Yuan, Q., Wang, T., Yu, P., Zhang, H., Zhang, H., and Ji, W. (2021). “A review on the electroluminescence properties of quantum-dot light-emitting diodes.” *Org. Electron.*, 90(November 2020), 106086.
- Yudar, H. H., Pat, S., Korkmaz, Ş., Özen, S., and Şenay, V. (2017). “Zn/ZnSe thin films deposition by RF magnetron sputtering.” *J. Mater. Sci. Mater. Electron.*, 28(3), 2833–2837.
- Zachariasen, W. H. (1967). “A general theory of X-ray diffraction in crystals.” *Acta Crystallogr.*, 23(4), 558–564.
- Zedan, I. T., Azab, A. A., and El-Menyawy, E. M. (2016). “Structural, morphological and optical properties of ZnSe quantum dot thin films.” *Spectrochim. Acta - Part A Mol. Biomol. Spectrosc.*, 154, 171–176.
- Zeng, K., Xue, D. J., and Tang, J. (2016). “Antimony selenide thin-film solar cells.” *Semicond. Sci. Technol.*, 31(6), 1–13.
- Zeng, X., Pramana, S. S., Batabyal, S. K., Mhaisalkar, S. G., Chen, X., and Jinesh, K. B. (2013). “Low temperature synthesis of wurtzite zinc sulfide (ZnS) thin films by chemical spray pyrolysis.” *Phys. Chem. Chem. Phys.*, 15(18), 6763–6768.
- Zhao, H., Farah, A., Morel, D., and Ferekides, C. S. (2009). “The effect of impurities

on the doping and VOC of CdTe/CdS thin film solar cells.” *Thin Solid Films*, 517(7), 2365–2369.

Zhao, X. H., Liu, S., Zhao, Y., Campbell, C. M., Lassise, M. B., Kuo, Y. S., and Zhang, Y. H. (2016). “Electrical and Optical Properties of n-Type Indium-Doped CdTe/Mg_{0.46}Cd_{0.54}Te Double Heterostructures.” *IEEE J. Photovoltaics*, 6(2), 552–556.

Zheng, Z., Zu, X., Zhang, Y., and Zhou, W. (2020). “Rational design of type-II nano-heterojunctions for nanoscale optoelectronics.” *Mater. Today Phys.*, 15, 100262.

Zhou, Y., Leng, M., Xia, Z., Zhong, J., Song, H., Liu, X., Yang, B., Zhang, J., Chen, J., Zhou, K., Han, J., Cheng, Y., and Tang, J. (2014). “Solution-Processed Antimony Selenide Heterojunction Solar Cells.” *Adv. Energy Mater.*, 4(8), 1301846.

Zhou, Y., Wang, L., Chen, S., Qin, S., Liu, X., Chen, J., Xue, D. J., Luo, M., Cao, Y., Cheng, Y., Sargent, E. H., and Tang, J. (2015). “Thin-film Sb₂Se₃ photovoltaics with oriented one-dimensional ribbons and benign grain boundaries.” *Nat. Photonics*, 9(6), 409–415.

Ziesche, P., Eschrig, H. (Helmut), Technische Universität Dresden. Institut für Theoretische Physik., European Physical Society., International Symposium on Electronic Structure of Solids (21st : 1991 : Gaussig, G., and Dresdener Seminar für Theoretische Physik. (1991). “Electronic structure of solids ’91 : proceedings of the 75. WE-Heraeus-Seminar and 21st Annual International Symposium on Electronic Structure of Solids held in Gaussig (Germany), March 11-15, 1991.” 249.

Zubair, M., Ul Hassan, M. M., Mehran, M. T., Baig, M. M., Hussain, S., and Shahzad, F. (2022). “2D MXenes and their heterostructures for HER, OER and overall water splitting: A review.” *Int. J. Hydrogen Energy*, 47(5), 2794–2818.

LIST OF PUBLICATIONS:

1. **Subhasmita Ray**, Biswajit Barman, C Darshan, Kartick Tarafder, Kasturi V. Bangera (2022) “ZnS_xSe_{1-x} thin films: A study into its tunable energy band gap property using an experimental and theoretical approach”, *Solar energy* 240 (140-146), Elsevier.
2. **Subhasmita Ray**, Kartick Tarafder (2023) “Investigation of CdSe and ZnSe as potential back surface field layers for CdTebased solar cells: A study from first principle calculations,” *Advanced theory and simulations* 6, Issue 3 (2200718), Wiley.
3. **Subhasmita Ray**, Kasturi V. Bangera, Kartick Tarafder (2021) “Synthesis and characterization of Cu doped CdTe thin films for a solar cell application,” *Materials Today Proceedings* 39, Part 5,(2000-2004), Elsevier
4. **Subhasmita Ray**, Kartick Tarafder (2023) “Validation of ZnTe as back surface field layer for CdTe solar cells: A combined experimental and theoretical study,” *Materials science and engineering B* 295, (116548) Elsevier.
5. **Subhasmita Ray**, Kartick Tarafder, “Investigation of S alloyed Sb₂Se₃, a new 2D mxenes (S₂HfNNOH) and their heterostructure for solar cell applications”, *Applied surface science* (Manuscript submitted).
6. Soumitra Payra, **Subhasmita Ray**, Ruchi Sharma, Kartick Tarafder, Paritosh Mohanty, Sounak Roy (2022) “Photo- and Electrocatalytic Reduction of CO₂ over Metal-Organic Frameworks and Their Derived Oxides: A Correlation of the Reaction Mechanism with the Electronic Structure”, *Inorganic Chemistry* 61, (2476–2489), ACS.
7. Vishnu G Nath, **Subhasmita Ray**, Subir Roy, Bharath S P, Kartick Tarafder, S Angapanne, “Mixed Spinel structure of ZnFe₂O₄ with tunable cation distribution: an exciting material for ultrasensitive and selective NO_x detection at room temperature”, *Journal of materials chemistry A*. (Under review)
8. Umasish Bhoi, **Subhasmita Ray**, Sujit Bhand, Pranay Ninawe, Debashree Roy, Shammi Rana, Kartick Tarafder, Nirmalya Ballav, “3d7-3d8 synergistic interactions beyond proximity in Bimetal-Organic framework for Catalytic Water Oxidation”, *ACS Energy Letters*. (Under review).

SUBHASMITA RAY

Address-HN-L21/33,

Panchasakhanagar, Khandagiri,

Bhubaneswar, Odisha, India, 751019

Phone-+91-7625037090

Email-subhasmitaray01@gmail.com

A dedicated and capable research fellow with 4.5 years of experience. Working on a challenging job profile provides an opportunity to enhance my technical skills and knowledge and could provide me insight into new aspects that would be helpful for my career. Talented researcher with a progressive background in Compound semiconductor thin films for solar cell applications and Density Functional Theory (DFT). Focused on expanding knowledge and results through continuous expansion of research efforts and iterative designs.

RESEARCH EXPERIENCE:

- Design, assembly, and maintenance of experimental setups(Thermal evaporation unit)
- Characterize and analyze the structural, morphological, electrical, and optical properties of chalcogenide thin films.
- Study and analyze different properties of pristine semiconductors and their interface by using the Density Functional Theory.
- Scientific dissemination through publications in peer-reviewed journals.

Intern fellow at Institute of Physics, Bhubaneswar

- Soft Matter Physics (Brownian motion and Viscoelasticity)
-

ACADEMIC PROFILE :

- Ph.D., Physics Department, National Institute of Technology, Karnataka (Thesis Submitted,2023)
Dissertation Title: *Investigation of 2D metal chalcogenide nanostructures for solar cell applications.*
- M.Sc., Physics Department, Berhampur University, Odisha
Project Title: Optical Properties of Si Nanowires

PUBLICATIONS :

1. **Subhasmita Ray**, Biswajit Barman, C Darshan, Kartick Tarafder, Kasturi V. Bangera (2022) “ZnS_xSe_{1-x} thin films: A study into its tunable energy band gap property using an experimental and theoretical approach”, *Solar energy* 240 (140-146), Elsevier.
2. **Subhasmita Ray**, Kartick Tarafder (2023) “Investigation of CdSe and ZnSe as potential back surface field layers for CdTe based solar cells: A study from first principle calculations,” *Advanced theory and simulations* 6, Issue 3 (2200718), Wiley.
3. **Subhasmita Ray**, Kasturi V. Bangera, Kartick Tarafder (2021) “Synthesis and characterization of Cu doped CdTe thin films for a solar cell application,” *Materials Today Proceedings* 39, Part 5,(2000-2004), Elsevier
4. **Subhasmita Ray**, Kartick Tarafder (2023) “Validation of ZnTe as back surface field layer for CdTe solar cells: A combined experimental and theoretical study,” *Materials science and engineering B* 295, (116548) Elsevier.
5. Soumitra Payra, **Subhasmita Ray**, Ruchi Sharma, Kartick Tarafder, Paritosh Mohanty, Sounak Roy (2022) “Photo- and Electrocatalytic Reduction of CO₂ over Metal-Organic Frameworks and Their Derived Oxides: A Correlation of the Reaction Mechanism with the Electronic Structure”, *Inorganic Chemistry* 61, (2476–2489), ACS.
6. Vishnu G Nath, **Subhasmita Ray**, Subir Roy, Bharath S P, Kartick Tarafder, S Angapanne, “Mixed Spinel structure of ZnFe₂O₄ with tunable cation distribution: an exciting material for ultrasensitive and selective NO_x detection at room temperature”, *Journal of materials chemistry A*. (Under review)
7. Umasish Bhoi, **Subhasmita Ray**, Sujit Bhand, Pranay Ninawe, Debashree Roy, Shammi Rana, Kartick Tarafder, Nirmalya Ballav, “3d7-3d8 synergistic interactions beyond proximity in Bimetal-Organic framework for Catalytic Water Oxidation”, ACS Energy Letters.(Under review)

CONFERENCES :

1. Presented a poster entitled “Optical properties of undoped and Cu doped CdTe thin films for solar cell applications” at ‘Bring The Nanoworld Together (BTNT-2019).’
2. Oral presentation entitled “Optimized growth conditions, Structural, morphological and electrical properties of undoped and Cu doped CdTe thin films” at ‘3rd international conference on solar energy photovoltaics (ICSEP 2019)’

ACADEMIC ACTIVITIES/ ACHIEVEMENTS :

1. **SWAMI SIVANANDA MEMORIAL SCHOLARSHIP**, for securing the highest mark in my B.Sc. (honors as well as aggregate) first class first honors with distinction.
 2. Attended a short-term course on DFT and molecular dynamics simulation organized by MNIT, Jaipur.
 3. Attended 2023 virtual school on Many-body calculations using EPW and BerkeleyGW.
-

FAMILIARITY WITH SCIENTIFIC EQUIPMENT:

XRD, UV-VIS spectrometer, Thermal evaporation unit, spray pyrolysis unit, Spin Coater unit, Source meter, High resistance LCR meter, and Rheometer.

FAMILIARITY WITH SCIENTIFIC SOFTWARE:

VASP, Quantum Espresso, Avogadro, Vesta, SIESTA, DLPOLY, & QuantumATK.

RESEARCH INTEREST:

Thin film photovoltaics, OER, HER, Thin film gas sensors

REFERENCES:

1. Dr. Kartick Tarafder.
karticktarafder@gmail.com
2. Dr. Kasturi V. Bangera
kasturivb@gmail.com